SPECTROSCOPIC STUDIES OF GAS-PHASE MOLECULAR CLUSTERS

Thesis by

Chi-Kin Wong

In Partial Fulfillment of the Requirements
for the Degree of
Doctor of Philosophy

California Institute of Technology
Pasadena, California
2001
(Submitted June 26, 2000)

TABLE OF CONTENTS

ACKNOWLEDGEMENTS

This thesis would not have been possible without the assistance of many others. First of all I would like to thank my advisor, Professor Mitchio Okumura, for his teaching, inspiration, encouragement and support. He taught me how to be a physical chemist, inspired me with his dedication and knowledge, encouraged me during my difficult times, and supported me when I was struggling with the experiments. I am also grateful to his financial support throughout my career in Caltech.

I am indebted to all the scientists in Okumura group. James Spott was my mentor in the lab. I thank him for showing me the knowledge and teaching me the techniques for performing experiments. He was patient in his training and forgiving to my foolishness with the machine. Matt Johnson showed me the way around the lab when I first joined the group. Yi-Bin Cao taught me about the OPO. Jong-Ho Choi introduced me to the TOFU experiment. Keith Kuwata helped me started in anion spectroscopy.

Julio Lobo is a good friend and partner. We shared lots of good times and bad times in and outside of the lab, and all the credits of the CN^- experiment. Our story of working sequentially in 12-hour shifts for that experiment is well remembered. And the ammonia experiments would not have been possible without his help. I thank him for his friendship, support and his lure to my "espresso" addiction.

I am thankful to the professional staffs of the support services. Mike Roy, Guy Duremberg, Ray Garcia and Tom Dunne were always able to help and give attention to our problems. Other members of the Okumura group – Chun Chung Tsao, Teresa Moore, Lance Christensen, Eva Garland, Daniel Paik, Andrei Deev, Rachel Niemer – were also

helpful to me and made my experience an enjoyable one. Same goes to my fellow Hong Kong students – Hung Kay Lee, Vincent Tai and John Yip.

I am very grateful to Professor Sunney Chan. He supported me through my years in Caltech, and helped me as a foreign student in USA. I am also very thankful to my undergraduate mentor, Professor Wai-Kee Li, who taught me about scientific research and gave me advice all these years.

Most of all, I would like to thank my family for their understanding and encouragement. And Abbie, for her inspiration.

I would like to dedicate this thesis to

Abbie

For her inspiration and enrichment of my life.

ABSTRACT

Spectroscopic investigations of hydrogen-bonding and van der Waals' interactions in molecular clusters were studied by the techniques of infrared predissociation and resonance-enhanced multiphoton ionization spectroscopies (REMPI). *Ab initio* calculations were applied in conjunction for data interpretation.

The infrared predissociation spectroscopy of $CN^-\cdot(H_2O)_n$ (n = 2 - 6) clusters was reported in the region of 2950 - 3850 cm^{-1}. The hydrogen bondings for the C-site and N-site binding, and among the water molecules were identified for n = 2 to 4. A spectral transition was observed for n = 5 and 6, implying that the anion was surface-bound onto the water aggregates in larger clusters.

The infrared predissociation spectroscopy of $Br^-\cdot(NH_3)$ and $I^-\cdot(NH_3)_n$ (n = 1-3) clusters was reported in the region of 3050-3450 cm^{-1}. For the $Br^-\cdot(NH_3)$ complex, a dominating ionic NH stretch appeared at 3175 cm^{-1}, and the weaker free NH stretch appeared at 3348 cm^{-1}. The observed spectrum was consistent to the structure in which there was one nearly linear hydrogen bond between Br^- and the NH_3 moiety. For the $I^-\cdot(NH_3)$ complex, five distinct IR absorption bands were observed in the spectrum. The spectrum was not consistent with basic frequency patterns of three geometries considered in the *ab initio* calculations – complex with one, two and three hydrogen bondings between I^- and the NH_3 moiety. Substantial inhomogenous broadening were displayed in the spectra for $I^-\cdot(NH_3)_n$ (n =2-3), suggesting the presence of multiple isomers.

The REMPI spectroscopy of the bound $4p\ ^2\Pi_{1/2}$ and $^2\Pi_{3/2}$ states, and the dissociative $3d\ ^2\Sigma^+_{1/2}$ state in the Al·Ar complex was reported. The dissociative spectrum

at Al^+ channel suggested the coupling of the $4p\ ^2\Pi_{1/2,3/2}$ states to the repulsive $3d\ ^2\Sigma^+_{1/2}$ state. The spin-electronic coupling was further manifested in the dissociative Al^+ spectrum of the $3d\ ^2\Sigma^+_{1/2}$ state. Using the potential energy curves obtained from *ab initio* calculations, a bound $\rightarrow$ continuum Franck-Condon-intensity simulation was performed and compared with the one-photon $3d\ ^2\Sigma^+_{1/2}$ profile. The agreement provided evidence for the perturbation above the Al(3d)Ar dissociation limit, and the repulsive character of the $3d\ ^2\Sigma^+_{1/2}$ state.

CHAPTER 1

Introduction

1.1 INTRODUCTION

Clusters represent a unique regime between gas-phase molecules and condensed media. One the one hand, they are important systems for the study of intermolecular forces such as hydrogen bonding and van der Waals' interaction. Their finite complexity provides an opportunity for in-depth investigations of these bonding interactions with appreciable details. On the other hand, they are useful models for bridging the gap between gas phase and condensed phase. With the size-variance from a few molecules to the nano-particle region, they can provide informative insights into the evolution from an individual molecule to the bulk environment. They may also allow a microscopic study of such processes as nucleation, solvation and condensation. For these reasons, the study of molecular clusters has been an active field of research for many years.[1-5] Numerous experimental techniques and theoretical methods have been employed to enrich our understanding about their physical and chemical properties. Some of the examples include high-pressure mass spectrometry, FT-ICR, photoelectron, microwave, infrared, optical and UV spectroscopies, molecular dynamic, classical, semiempirical and *ab initio* calculations.

This thesis work is dedicated to the spectroscopic investigations of molecular clusters. Specifically we are interested in studying two types of intermolecular forces in weakly-bound complexes: hydrogen-bonding and van der Waals' interactions. We have applied the techniques of infrared predissociation and resonance-enhanced multiphoton ionization spectroscopies for our investigations. In conjunction, we have also employed *ab initio* calculations for data interpretation.

1.2 THESIS OUTLINE

The main body of this thesis is divided into four chapters. Chapter 2 presents a discussion on the infrared predissociation spectrometer employed for the anionic clusters. An overview of the machine operation will be provided. Details on several specific modifications will also be reviewed.

In Chapter 3 the vibrational spectroscopy of the $CN^-(H_2O)_n$ clusters, n = 2-6, will be presented. This study focuses on the hydrogen bonding of water molecules around the molecular anion. The possibility of an intramolecular proton-transfer reaction in the larger clusters will also be discussed.

Chapter 4 presents the infrared spectroscopic results on $Br^-(NH_3)$ and $I^-(H_2O)n$ (n =1-3). The complexation with ammonia leads to the possibility of multiple hydrogen bonding between the ionic center and solvating ligands. Variation of the halide ion offers the opportunity of trend observation. *Ab initio* calculations are also performed to aid the interpretation of the spectra.

In Chapter 5, the electronic spectroscopy of the $3d\ ^2\Sigma^+_{1/2} \leftarrow 3p\ ^2\Pi_{1/2}$ transition in AlAr complex will be presented. This study focuses on the perturbation between the Al 3d/4p electronic manifolds induced by the Ar complexation. Continuum $\leftarrow$ bound simulations based on *ab initio* potential energy curves are also performed for comparison with the experimental data.

1.2 REFERENCES

1. J. P. Maier (Ed.), *Ion and Cluster Ion Spectroscopy and Structure*, Elsevier, Amsterdam, 1989.

2. H. Haberland (Ed.), *Clusters of Atoms and Molecules I: Theory, Experiment, and Clusters of Atoms*, Springer-Verlag, Berlin, Germany, 1994.

3. H. Haberland (Ed.), Clusters of Atoms and Molecules II: *Solvation and Chemistry of Free Clusters, and Embedded Clusters, Supported and Compressed Clusters*, Springer-Verlag, Berlin, 1994.

4. E. R. Berstein (Ed.), *Chemical Reactions in Clusters*, Oxford University Press, New York, 1996.

5. A. W. Castleman, Jr. and S. Wei, *Annu. Rev. Phys. Chem.*, **45**, 658 (1994).

CHAPTER 2

Infrared Predissociation Techniques for Gas-Phase Molecular Clusters

2.1 INTRODUCTION

As mentioned in Chapter 1, the work in this thesis focuses on the study of weakly-bound interactions in molecular clusters through the application of gas-phase spectroscopic techniques. Specifically two experimental schemes were employed to investigate the vibrational and electronic transitions in various complexes of interest: infrared vibrational predissociation spectroscopy (IR-VPS) and resonance enhanced multiphoton ionization (REMPI) spectroscopy. In this chapter, particular details for the IR-VPS experiment will be described. As the IR-VPS experimental set-up gas been reviewed in the previous studies of our group[1-4], the discussions will emphasize on three specific modifications implemented for improvement.

For details on design, construction and experimental set-up of the REMPI apparatus, readers are referred to the extensive discussion reviewed by Spotts[5]. Only a basic overview will be given in Chapter 5.

2.2 INFRARED PREDISSOCIATION SPECTROMETER

2.2.1 Overview

The cluster ion apparatus was a tandem TOF mass spectrometer equipped with a pulsed ion-generation source, and coupled to an infrared laser for vibrational excitation. Figure 1 shows the overall arrangement of the experiment. The apparatus was consisted of three regions. The first region was a 20"x20"x30" chamber in which ionic clusters were generated by ionization of a pulsed gas jet. With supersonic gas expansion, the ions were transported downstream (4-5 cm) and collimated by a skimmer, and then passed into the second region. The second chamber was a Wiley-McLaren-type[6] TOF mass

spectrometer where ions were pulsed-accelerated to high kinetic energy (1.0 to 2.5 kV). After travelling through the mass spectrometer, the ions were separated into packets and selectively passed into the third region according to their masses. The third chamber was the detector region equipped with optical windows for laser input. The mass-selected ions were crossed with the infrared laser output from an optical parametric oscillator (OPO) for vibrational excitation. Both the parent ions and predissociation products were mass analyzed by a reflectron and detected by a micro-channel-plate (MCP) detector.

2.2.2 Cluster Generation

A schematic diagram for cluster generation is shown in Figure 2. Molecular clusters were generated in gas phase by means of supersonic expansion[7], during which a gas mixture at high stagnation pressure (900-1200 Torr) was introduced into the vacuum chamber (10^{-6} Torr) through a pulsed valve driven by piezo-disk (Physik Instrument P-283.23) motion. The expansion converted random motion of the gas molecule into a highly directional flow, and thus led to significant translational and rotational cooling through numerous three-body collisions. Vibrational cooling was also induced but to a lesser degree. The overall result was the formation of molecular aggregates with reduced internal energy.

Ionization of clusters was achieved by dissociative attachment of electrons to an "active" species in the molecular beam. The electron source was generated from a home-made electron gun with repelling voltage of 700-1000 eV. With the presence of solvent-type molecules (S) in the gas mixture, aggregation of solvents around the ionic center

took place and resulted in the formation of $X\cdot(S)_n$ clusters, where X could be either a cation or anion.

Eeffective cooling of the molecular clusters was critical for a successful vibrational predissociation experiment. The reduced internal energy allowed: (1) the possible formation of weakly-bound complexes; (2) and a significant suppression of spectral congestion/broadening, and led to the observation of distinct spectral features. Therefore it was particularly important to optimize experimental conditions for the production of "cold" clusters. One could monitor the cluster temperature by measuring the amount of metastable ions formed during the flight time, or through the observation of hot spectra which would display significant spectral broadening. For further reference, some of the key parameters for cluster optimization are reviewed as follows:

A. Carrier Gas.

Previous experience in our group showed that CH_4 was a suitable carrier gas for vibrational cooling of ionic clusters. The operative mechanism was believed to be the coupling of expansion cooling with the vibration modes in CH_4. However, the ion intensity could be enhanced by mixing CH_4 with other carrier gases using the mass flow controllers (MKS 1159B). For the $CN^-(H_2O)_n$ clusters, ion intensity was significantly increased by introducing H_2 into the gas mixture. Generally speaking, higher H_2 content would lead to stronger intensity for the ions, but also a higher cluster temperature. Typical mixing ratio of H_2:CH_4 ranged from 1:3 to 1:1. For the $X^-(NH_3)_n$ (X = Br and I), it was necessary to use NH_3 as part of the carrier gas. Similar to the case of H_2, a higher content of NH_3 lead to higher cluster temperature. Optimized NH_3:CH_4 ratio was about 1:5 to 1:7.

B. "Source Chemical" for Anions.

Anion generation was achieved by the dissociative attachment of an electron to the appropriate molecule entrained in the molecular beam. The high-energy electron beam created a plasma environment at the early stage of expansion, which in turn led to the formation of secondary electrons with lower kinetic energy. A molecule could then capture a secondary electron and result in a dissociative attachment reaction:

$$e^- + A\text{–}B \rightarrow A\text{–}B^{-*} \rightarrow A^- + B$$

$$\text{or} \qquad\qquad \rightarrow A + B^-$$

It was, therefore, necessary to choose a suitable reagent that had an appreciable yield for this reaction. For example, early attempts for $CN^-(H_2O)_n$ employed substituted acetonitriles, $(CH3)_n(H)_{3-n}C\text{–}CN$, as the source of CN^-, but failed to generate sufficient amount of anion for the infrared experiment. BrCN, which effectively captured low-energy electrons[8], was found to be an appropriate reactant instead. Another observation was that it was generally preferable to employ the least possible amount of reactant, as long as it sustained sufficient partial pressure in the carrier gas for ion generation. (Temperature was a convenient parameter to control the partial pressure.) A high content of the reactant could lead to extensive reactions in the expansion and result in increased cluster temperature.

C. Expansion Conditions

Supersonic expansion was achieved by introducing the gas mixture at high stagnation pressure (900-1200 Torr) into the vacuum chamber (10^{-6} Torr) through a pulsed valve driven by piezo-disk motion. Three modifications were found to be effective in improving the cluster formation. The first change was to replace the vacuum seal of the

pulsed valve opening from an o-ring to a hard plastic (Vespel-SP1) tip (Figure 2). Previously it was found that the rising edge of the gas pulse could have a significant influence on the degree of clustering[5,9]. The plastic surface allowed a much faster opening of the pulsed valve, and reduced the time delay between the poppet retraction and actual gas flow. Due to the elastic nature, this delay was intrinsically long for the o-ring seal. This led to a reduced pulse length and higher collision frequency for the expansion. In other words, a reduced gas load could result in same degree of supersonic cooling.

Secondly, a straight channel (diameter = 2.0 mm) was employed in place of the original cone-shape channel after the pulsed valve. Presumably the straight channel led to a restricted expansion, and thus induced a pre-mixing of "source molecule" and the clustering ligands (solvent molecules). This channel was preferable for the generation of larger clusters.

The third change was the lengthening of skimmer-chamber wall distance (Figure 2). The underlying rationale was that the supersonic expansion would be disrupted by the gas bounced back from the chamber. A lengthening of the skimmer-to-wall distance could delay the arrival time of the rebound gas (preferably longer than the extraction time for ions), and reduce the collision along the expansion direction. To this end, a 3"-long mounting extension was placed between the skimmer and the chamber (Figure 3).

With all these modifications installed in place, a significant improvement in ion intensity and cluster temperature was observed. As an illustration, the infrared spectra of $I^-(H2O)_2$ taken under old and new conditions are shown in Figure 4. One could clearly

note that the previously unresolved features were made evident because of the improved cluster temperature.

2.2.3 Pulsed Electron Source

Previous experiments on anion clusters employed a continuous electron beam for ionization. The electrons were generated from a home-made electron gun positioned closed to the pulsed-valve housing (Figure 2). As the electron cloud would create a plasma environment, the clusters were inevitably heated during the ionization. One way to partly compensate for this problem was to aim the collimated electron beam as close to the beginning point of the expansion as possible. In this way one could maximize the cooling effect from supersonic expansion.

In view of this reason, Bieske and workers suggested an arrangement for electron injection that would allow a close proximity of the electron to the gas jet[10,11]. They mounted a heated tungsten filament at the beginning of the expansion around the molecular beam, and injected the electrons into the gas from within a few mm. With this set-up, they were able to generate weakly-bound cationic clusters with rare gases (He, Ne) as the solvating ligands.

Guided by their filament design, we constructed a new assembly for the electron injection into the gas. A thoriated iridium filament (Duniway) was placed close to the expansion nozzle as shown in Figure 5. The filament was heated up by a current of 5-6 A to generate thermal electrons. A pulsed voltage of -150 to -500 V, with a typical pulse width of 30 μs, was applied to the filament to eject the electrons out. An early attempt employed a DC voltage instead, but the ion intensity was significantly weaker and more

unstable. A repelling plate at about -700 V (DC) was located behind the filament to focus the electrons onto the gas. The entire assembly was enclosed inside stainless meshes to shield the ions from high voltages. It should be note that the repelling plate and the ground shield facing the gas were both curved inwards to create concave surfaces for an appropriate electric field (Figure 5b). The concave arrangement was necessary for focusing the electrons onto the molecular beam. An electric field generated by parallel-plate arrangement failed to produce enough sufficient ions for the experiment.

The assembly was mounted independently from the nozzle. The distance from the filament to the beam axis was about 1 cm. By sliding the nozzle backwards and forwards, the distance between the nozzle orifice and the ionization region could be adjusted. Typical distances were from 2 to 10 mm along the beam direction. Generally speaking, a shorter ionization-nozzle distance would lead to the production of colder cluster ions, but a decrease in ion intensity. Presumably it was due to the difficulty for electron penetration in a high gas-density region.

The main advantage of the new filament arrangement was the improvement in cluster temperature, so that weakly-bound complexes with solvating ligands such as CH_4 could also be observed. Figure 6 shows a TOF mass spectrum for the previously unobserved $CN^-(CH4)_n$, n = 3-12, clusters. Further indications of lower temperature included reduction in metastable ions and improvement in vibrational resolution (reduced spectral broadening/congestion).

2.2.4 Double-Pass Pumping for Optical Parametric Oscillator

The pulsed tunable infrared laser used in our experiments was generated from an home-made angle-tuned $LiNbO_3$ optical parametric oscillator (OPO). Details for design and construction have been given elsewhere[2,3]. In this section, we will discuss an alternative pumping arrangement for infrared generation.

The parametric oscillation is based on the second-order nonlinear dielectric properties of a crystal ($LiNbO_3$ in our case) in which the induced polarization has components proportional to the square of the electric field[12]. The generation of an infrared photon from OPO involves the transfer of energy from a pump photon (ω_p) to two new photons signal (ω_s) and idler (ω_i). Due to energy conservation, the three frequencies are related by:

$$\omega_p = \omega_s + \omega_i \ .$$

The most efficient OPO generation is obtained with collinear phase matching where all three beams are parallel to each other. In this case, the phase-matching condition (momentum conservation) is given by:

$$n_p\omega_p = n_s\omega_s + n_i\omega_i \ ,$$

where n's are refractive indexes.

Our OPO cavity was based on the design of Brosnan and Byer[2,3,13]. The cavity was 20 cm long and singly resonant with the signal photon. It was pumped by a 30-Hz Nd:YAG laser (Continuum YG660-S) which could generated 400 mJ/pulse at 1.06 μm. Due to the low damage threshold of $LiNbO_3$ (~600 $MWcm^{-2}$), the pump beam was multi-passed for ~10 m to ensure a nominally Gaussian TEM_{00} intensity profile and to remove "hot spots". Typical diameter for the Gaussian beam was 2.5 to 3.0 mm, with a pulsed width of 15-18 ns. The OPO output was continuously tunable from 2600 to 6800 cm^{-1}.

In previous experiments, the IR output was generated by a single-pass pumping of the Nd:YAG beam. A 15ns pulse would, therefore, allow an energy build-up of ~10 round-trip for the lasing photons (signal). In order to maximize the temporal overlap of the signal and the pump beam for each single pulse, a double-pass arrangement was employed. After passing through the OPO cavity, the pump beam was reflected by a 0° YAG mirror and traveled back the original beam-path in the backward direction (Figure 7). The time lag between the forward and backward beams was about 1 ns. In this double-pass arrangement, an effective 30 ns pumping could be achieved and the pump energy required for OPO generation could be reduced. This was particularly favorable as the $LiNbO_3$ crystal (Deltronic, damage threshold = 600 $MWcm^{-2}$) was susceptible to pump-beam damage. However, one should caution not to send the reflected beam all the way back to the pump laser. Such an action would cause serious damages to the laser optics. Therefore, the returning beam was aligned off the cavity axis by a small angle so that it became separated from the forward beam-path by a few centimeters 8 to 9 m upstream.

To separate the IP outputs from the pump beam, one could employ the condition of non-linear phase matching. In this scheme, each of the three beams propagated in a different direction[3]. However, the efficiency of power conversion would be reduced. Alternatively, one could maintain the collinear phase matching and use a beam separator to differentiate the beams (Figure 7). A suitable optics for the OPO output was the CaF_2 window with coating for 45° YAG reflection. Typical parameters for the double-pass pumping are also given in Table 1.

2.3 SUMMARY

This chapter has provided an overview for the infrared predissociation spectrometer employed for the experiments of discussion. Implementations for several modifications have also been reviewed. It is of interest to note the TOF mass spectrometer can readily be coupled to different laser systems for other applications. One successful attempt was the photodetachment (depletion) experiment on solvated I_2^- by ultraviolet radiation.

2.4 REFERENCES

1. Y. Cao, J.-H. Choi, B.-M. Haas, and M. Okumura, *J. Phys. Chem.*, **98,** 12176 (1994).
2. Y. Cao, *Ph.D. Thesis*, California Institute of Technology, 1994.
3. J.-H. Choi, *Ph. D. Thesis*, California Institute of Technology, 1995.
4. M. S. Johnson, *Ph. D. Thesis*, California Institute of Technology, 1995.
5. J. M. Spotts, *Ph.D. Thesis*, California Institute of Technology, 1998.
6. W. C. Wiley and I. H. McLaren, *Rev. Sci. Instru.*, **26,** 1150 (1955).
7. *Atomic and Molecular Beam Methods Vol. I*, Vol. , edited by G. Scoles (Oxford University Press, New York, 1988).
8. F. Bruning, I. Hahndorf, A. Stamatovic, and E. Illenberger, *J. Phys. Chem.*, **100,** 19740 (1996).
9. T. Schindler, .
10. E. J. Bieske, A. M. Soliva, and J. P. Maier, *J. Chem. Phys.*, **94,** 4749 (1991).
11. E. J. Bieske, *J. Chem. Soc. Faraday Trans.*, **91,** 1 (1995).
12. A. Yariv, *Optical Electronics*, 4th ed. (Saunders College Publishing, U. S. A., 1991).
13. S. J. Bronsnan and R. L. Byer, *IEEE J. Quantum ELectronics,* **15,** 45 (1979).

Table 1 Typical parameters of the Nd:YAG pump beam used for OPO double-pass pumping.

Pulse Width (ns)	15 - 18
Total Energy (mJ/pulse)	120 - 140
Peak Fluence (J/cm^2)	1.05 - 1.25
Gaussian-beam Diameter (mm)	2.5 - 3.0
Output Power (mJ/pulse)	~ 12 (Signal at 5798 cm^{-1}) ~ 3 (Idler at 3600 cm^{-1})
Resolution (cm^{-1})	1.5

2.5 FIGURE CAPTIONS

Figure 1 Schematic diagram of the infrared predissociation spectrometer.[3]

Figure 2 Schematic diagram of the source arrangement for ionic clusters.

Figure 3 Schematic diagram of the skimmer extension.

Figure 4 Comparison of the infrared spectra of $I^-(H_2O)_2$ taken under old (upper trace) and new (lower trace) source arrangement.

Figure 5 Schematic diagram of the pulsed electron source: (a) side view, (b) front view.

Figure 6 TOF mass spectrum for the $CN^-(CH_4)_n$ clusters.

Figure 7 Schematic diagram of the double-pass pumping of the OPO.

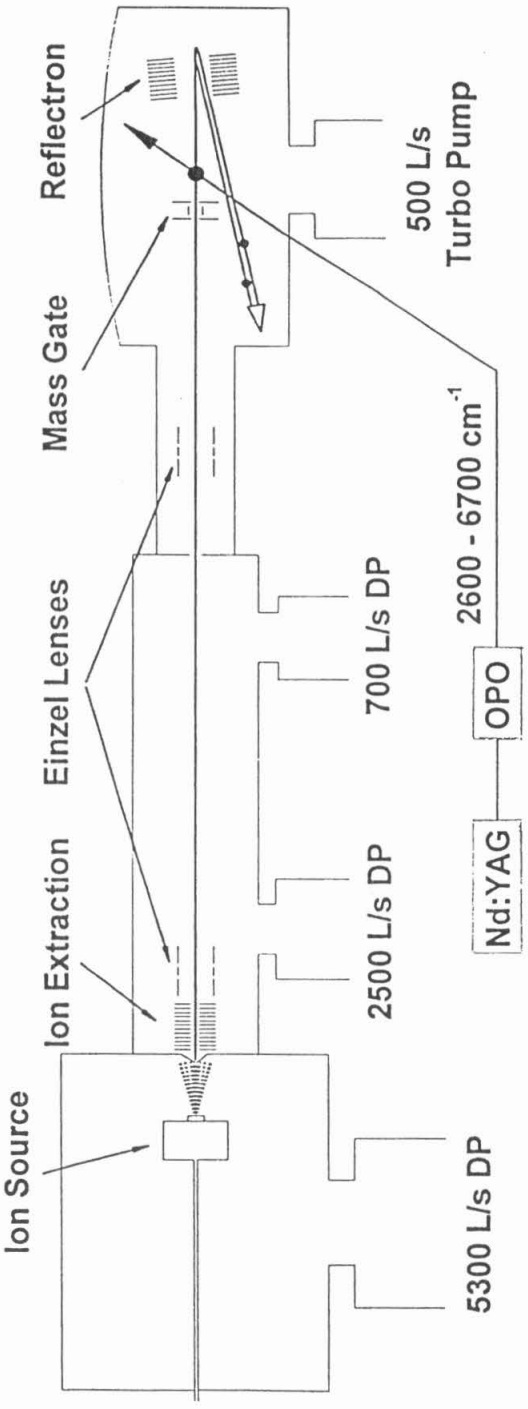
Reflectron
Mass Gate
Einzel Lenses
Ion Extraction
Ion Source
500 L/s
Turbo Pump
700 L/s DP
2500 L/s DP
5300 L/s DP
2600 - 6700 cm-1
OPO
Nd:YAG

Figure 1

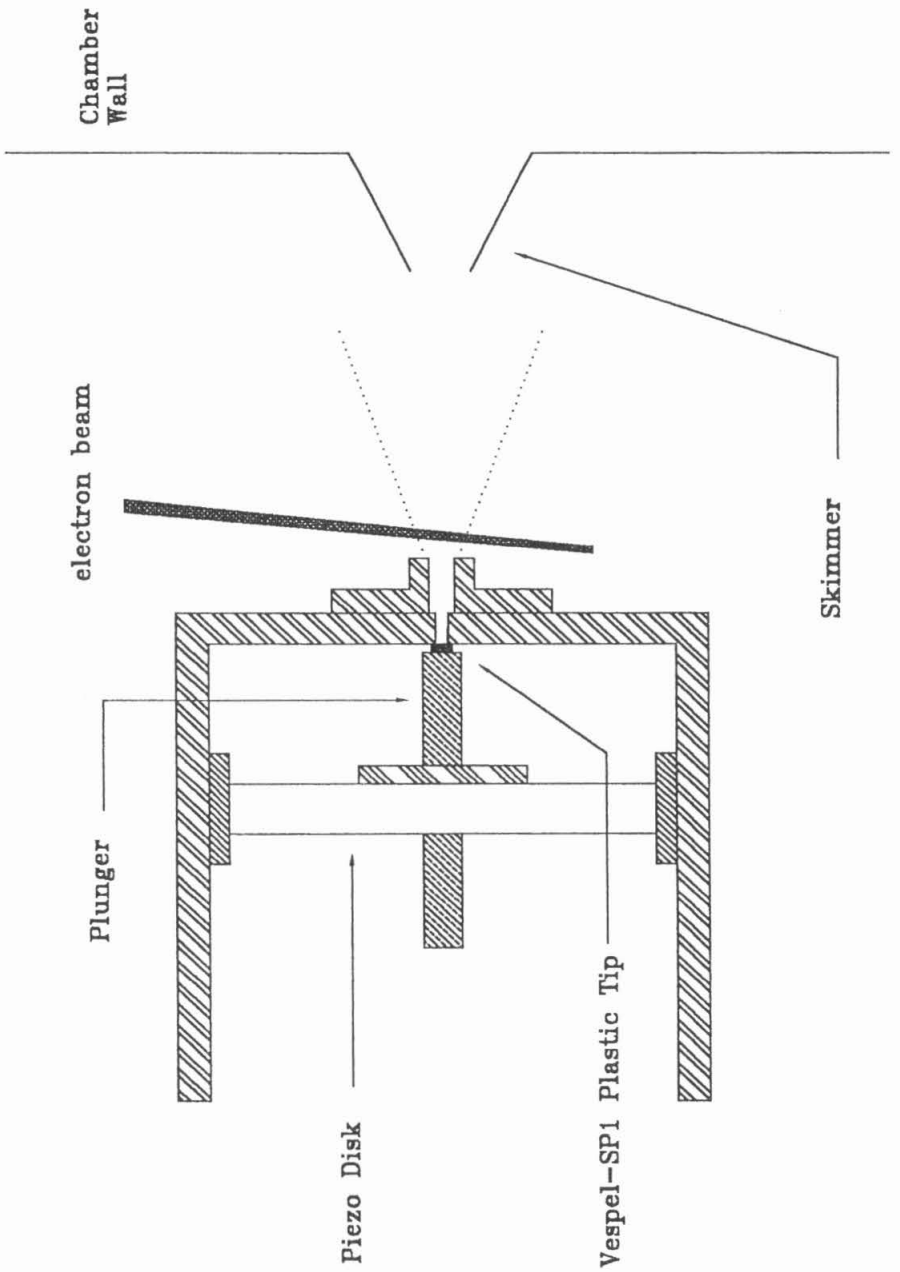
Chamber Wall
electron beam
Skimmer
Plunger
Piezo Disk
Vespel-SP1 Plastic Tip

Figure 2

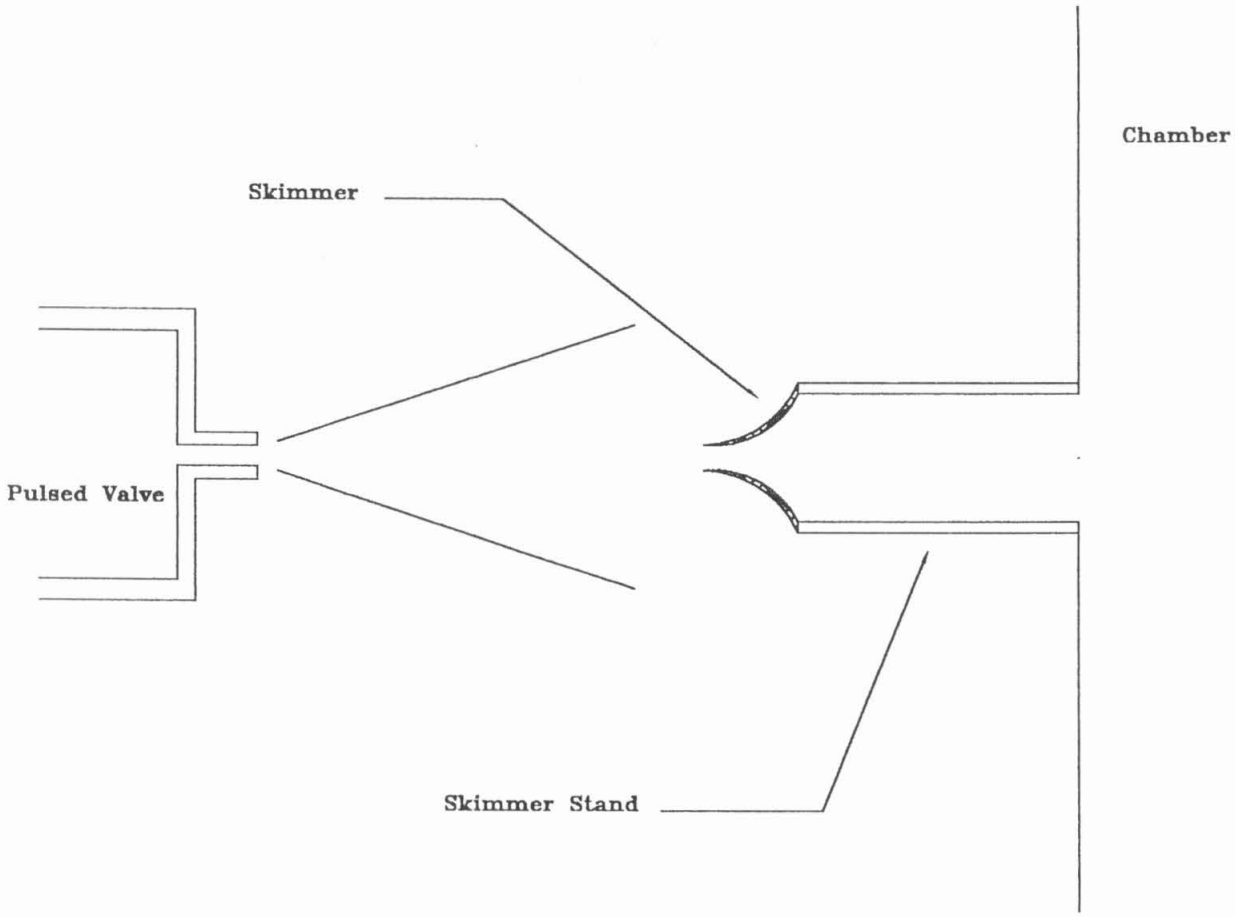

Figure 3

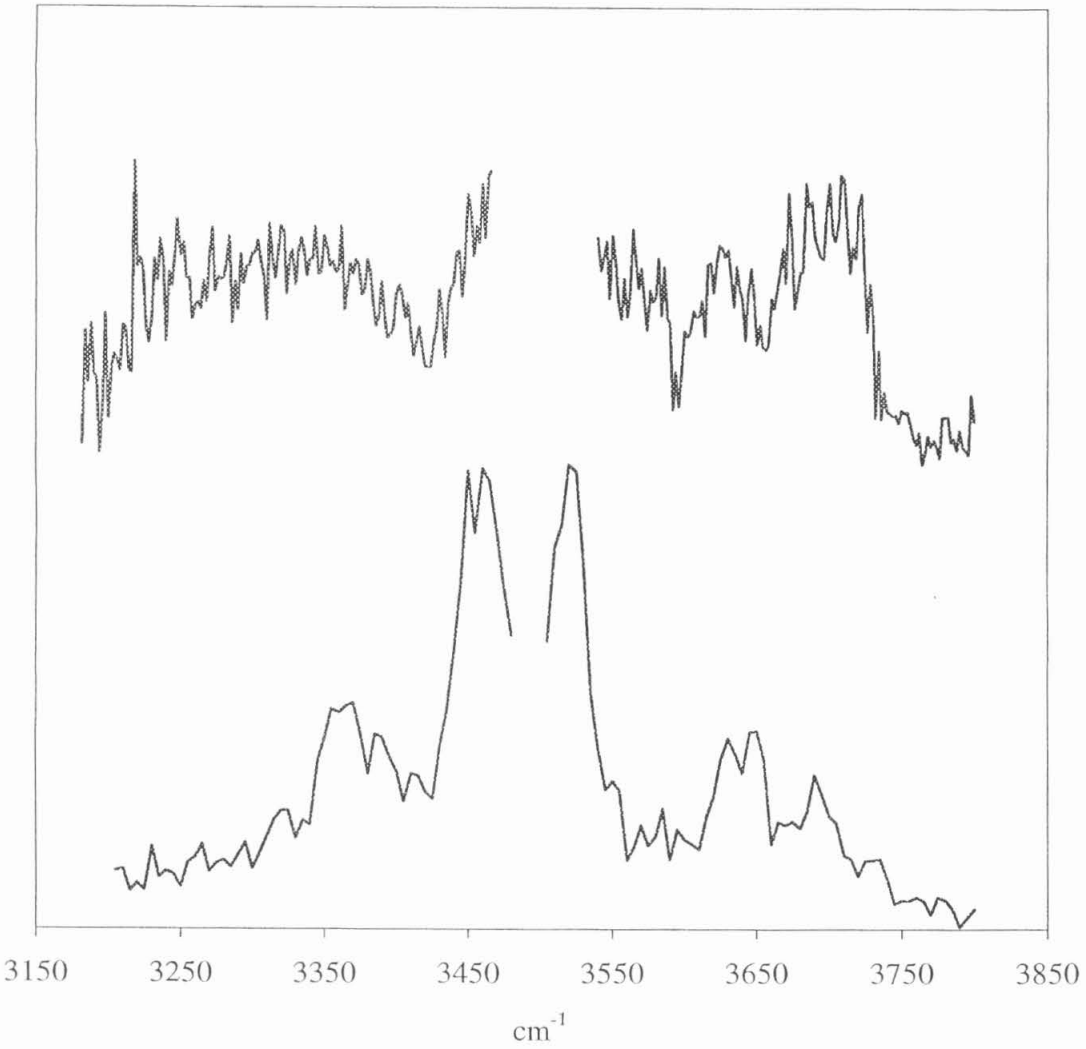

Figure 4

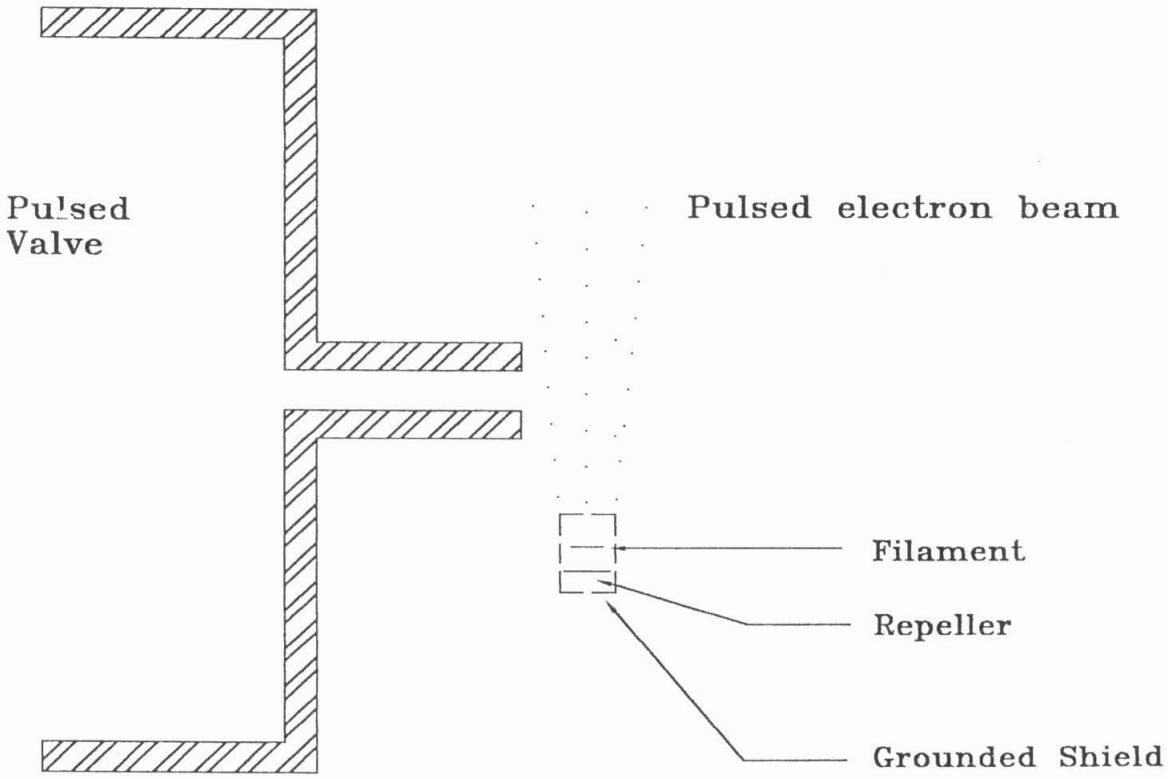

Side View

Figure 5a

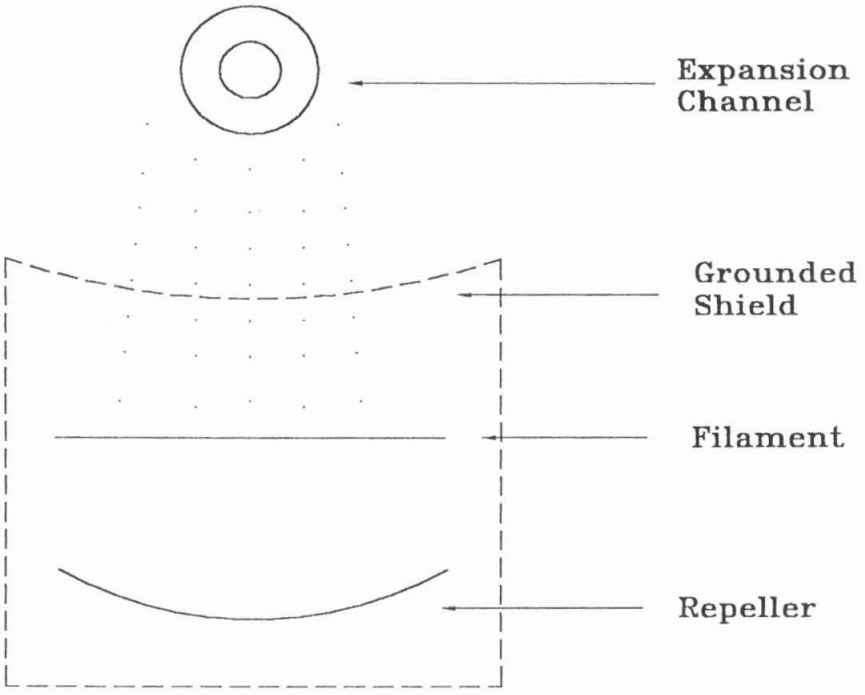

Front View

Figure 5b

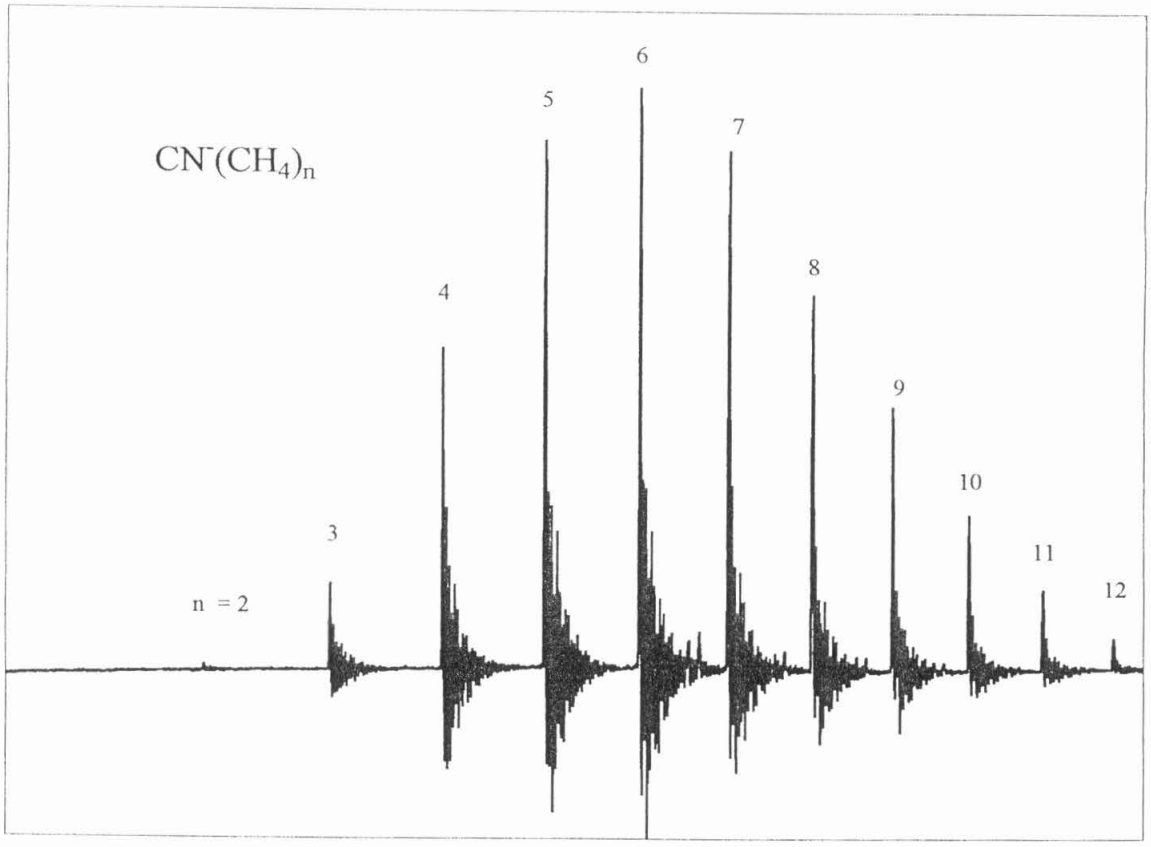

Figure 6

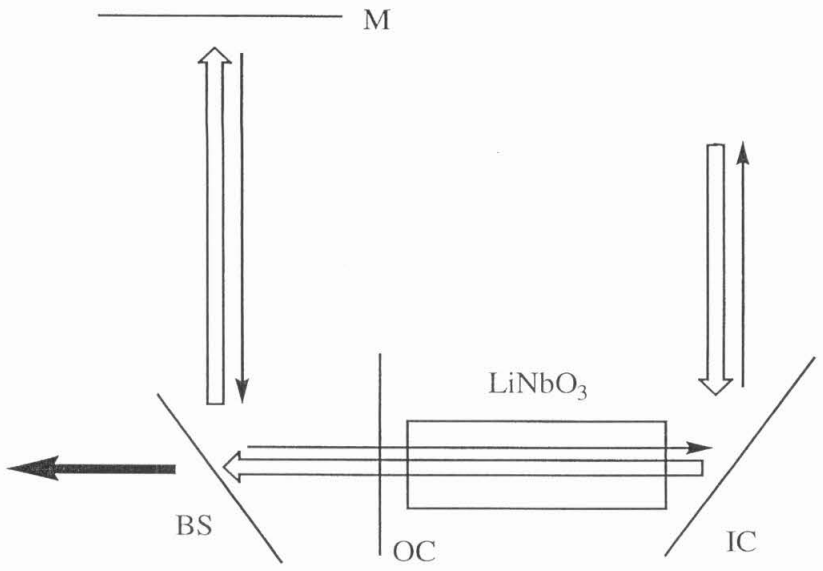

Forward Beam
Backward Beam
IR Output

IC: Input Coupler
OC: Output Coupler
BS: Beam Separator
M: YAG Mirror

Figure 7

CHAPTER 3

Stepwise Hydration of Cyanide Anion: The Vibrational Spectroscopy of $CN^-(H_2O)_n$, n = 2-6

3.1 INTRODUCTION

The study of ion-solvent interactions is of fundamental significance to the understanding of solution phase chemistry. As a solvating medium, water is particularly important because of its ubiquitous presence in chemical and biological systems, and the ability to form extensive hydrogen bonding networks. In the system of hydrated ions, the local environment around the ionic species is determined by the subtle balance of electrostatic and hydrogen bonding interactions between the ions and the solvent water, and the hydrogen bonding among water molecules. An in-depth picture of the local environment can, therefore, provide useful information about the interplay of these interactions and lead to a better understanding of the hydration process.

Gas-phase ionic clusters are useful models for the study of solvation interactions[1]. The controlled number of molecules and the tractable complexity in these clusters allow a microscopic understanding of the solvation process. In particular, the structural details of these clusters can provide direct information about the interactions such as the nature of bonding networks and the shell-closing behaviors around the ions. Among the various spectroscopic approaches, infrared predissociation spectroscopy of mass-selected ions has been proven to be a useful technique for determining the structures of gas-phase ionic clusters[2-7]. In these experiments, the vibrational frequencies of the solvent molecules are used as a sensitive probe for the bonding arrangement around the ionic center. As the simplicity of these systems usually allows the application of high-level *ab initio* calculations, a combined effort of experiment and theory may therefore provide a detailed picture of the structure and bonding of the ionic clusters.

Given the structural information available from vibrational studies, there have been extensive applications of the infrared predissociation spectroscopy to anionic systems in recent years[3-7]. In particular, the hydrated clusters of halide anions have received much of the attention. The structural simplicity and the chemical importance of these monatomic anions motivate the extensive research to understand the hydration behavior around these ions. The major complexity of the halide hydration arises from the property that small anions bind strongly to only one of the two protons in a water molecule, allowing the other free to form hydrogen-bonding networks with other water molecules in the hydration shell. Polarization of anions by hydrogen-bonding water molecules[8-11]. For polyatomic anions, additional properties such as multiple binding sites and permanent multipole moments will also be involved in determining the hydration structure around the ionic center. However, similar vibrational studies on molecular anions are only limited[7]. In view of the importance of polyatomic anions in solution phase chemistry, it will be of significance to extend the study of hydrated clusters to the polyatomic regime.

Cyanide ion is a suitable candidate as a prototypical system for hydration of molecular anions. On the one hand, it is an important anion in aqueous chemistry, with chemical properties similar to those of the spherical halide ions[12,15,17-19]. On the other hand, the ellipsoid-like diatomic ion allows an anisotropic environment for the primary hydration shell. The ambivalent nature[13] of the molecule provides two distinct binding sites for the competition of hydrogen bonding. The polarizability and permanent dipole moment[26] may also influence the hydration structure. Therefore it will be of interest to

perform a vibrational study on hydrated cyanide clusters, $CN^-\cdot(H_2O)_n$ to obtain the bonding and structural information.

Early experiments on these clusters focused on the measurement of thermodynamic quantities for the reaction:

$$CN^-\cdot(H_2O)_{n-1} + H_2O \leftrightarrow CN^-\cdot(H_2O)_n \qquad \Delta H_{rxn} = \Delta H_{n,n-1}\,. \qquad (1)$$

Using high-pressure mass spectrometry (HPMS), Kerbarle and coworkers[14] provided the first measurement of $-\Delta H_{1,0}$ with the value of 13.8 kcal/mol. Later on McMahon and coworkers[16] revisited the reaction with the same technique and obtained 12.7 ± 0.8 kcal/mol. In a similar study of binding the cyanide ion to various Brønsted acids[15], they also performed *ab initio* calculations on $CN^-\cdot(H_2O)_2$ at the SCF/4-31G level and concluded that the structure with one water binding to each end of CN^- is more stable than both water binding to the N side by 18.5 kcal/mol! However, the reliability of this calculation is doubtful because of the minimal level of theory and the obvious disagreement with experimental results (the binding energy of a single water molecule is only about 13 kcal/mol). Based on a survey of the binding energies to a series of Lewis-acid and Brønsted-acid types ligands, these authors suggested that in cases where the bonding appears to be principally electrostatic (e.g. SO_2, PF_3 and H_2O), the CN^- ion will behave similarly to the isotropic chloride ion. For the larger clusters, Meot-Ner (Mautner) and coworkers[18,19] employed HPMS to measure the hydration energies of $CN^-\cdot(H_2O)_n$, n = 1- 4 (Table1). From the absence of discontinuity in the solvation energies versus n (shell-closing effect), these authors also suggested that CN^- behaves as a spherical ion similar to Cl^- and Br^- towards the clustering of H_2O and HCN.

Theoretical evidence also points to isotropic hydration of CN^-. Jorgensen and

coworkers[17] performed an *ab initio* study on the $CN^-\cdot(H_2O)$ complex. They carried out optimization at the HF/6-31+G* level and obtained two minimum structures with the water binding by of linear hydrogen bonding to the N and C ends, with hydrogen-bond length of 1.919Å and 2.038Å at the N and C ends, respectively. Upon the inclusion of the electron correlation by single point calculation at MP2/6-31+G* level, the binding energy is calculated to be 16.3 kcal/mol for N hydration and 15.8 kcal/mol for C hydration. The energy difference is only 0.5 kcal/mol. In a similar *ab initio* study of the $CN^-\cdot(HCN)$ complex, Meot-Ner (Mautner)[18] suggested that CN^- is nearly isotropic towards the HCN binding. The bonding energy to the N site is preferred over the C site by 1.3 kcal/mol, with the T-shaped arrangement only 0.6 kcal/mol less stable than the C-site complex. In a more recent theoretical study, Ikeda et al.[20] performed a Monte Carlo simulation on $CN^-\cdot(H_2O)_n$ (n = 1 to 8) clusters at 300K. Using a semi-classical intermolecular potential (fitted to *ab initio* HF energy calculations), they calculated the isoenergy contour for monohydration around the CN^- core. They found that there are two stable and nearly isoenergetic regions around the N and C ends, with a binding energy of about 13 kcal/mol. Their simulations on larger clusters suggested that for n = 1 and 2, the water molecules bind primarily to the N site. For n = 3-6, there is a competition between binding to the C site and the formation of hydrogen bonding network among the water molecules. The binding energies of all the isomers are within a few kcal/mol.

Xantheas and coworkers[28] recently performed an *ab initio* study on $CN^-\cdot(H_2O)_n$ clusters (n = 1-3). They employed MP2/aug-cc-p-VDZ level of theory to calculate the minimum structures and binding energies. Their results will be reviewed in the following sections.

In this chapter, we report the vibrational predissociation spectroscopy of the hydrated cyanide clusters, $CN^-\cdot(H_2O)_n$ (n = 2 to 6), in the region of 3000 - 3850 cm^{-1}. A comparison with *ab initio* calculations for n = 1 to 3 will also be discussed. The computational results are generously provided by Prof. S. S. Xantheas at Pacific Northwest National Laboratory.

3.2 EXPERIMENTAL

The details of the experimental arrangement have been discussed in Chapter 2 and other references,[10,27] and only a brief account will be given here to provide the relevant details for this experiment. The cyanide ion clusters were generated by seeding a mixture of H_2O and BrCN (97%, Aldrich) vapor into a buffer gas at a total stagnation pressure of ~1000 Torr. The two samples were placed into separated bubblers along the carrier-gas line to prevent the reaction of BrCN with aqueous water. The deionized water was kept at room temperature (partial pressure = 18 Torr); and the BrCN was cooled down to -45 °C (partial pressure ≈ 1 Torr). The buffer gas employed was a mixture of CH_4/H_2 (99.99%, Matheson) with the mixing ratio varying from 5:1 to 1:5. The gas mixture was expanded into a vacuum chamber (10^{-6} Torr with no gas load) through a piezoelectric pulsed valve (nozzle dia. = 1.0 mm) at a repetition rate of 30 Hz (pulse width = ~200 μs). The piezoelectric disk was coated with fluorinated grease to prevent chemical damage to the crystal element. The gas mixture was ionized by intersecting with a continuous electron beam (500-750 eV) at the beginning of the supersonic expansion. Typical emission currents were about 2 mA, of which ~100-150 μA reached the Faraday cup at the far side of the nozzle.

The resulting ionized gas jet was skimmed and entered a time-of-flight (TOF) chamber where ions were extracted by a pulsed electric field (10 μs wide), and accelerated to -2.5 kV. The 2-m TOF mass spectrometer separated the clusters into spatially discrete mass packets, and a mass gate selected the ions of interest for pulsed infrared irradiation (1-4 mJ/pulse). The radiation was generated from a Nd:YAG-pumped lithium niobate ($LiNbO_3$) optical parametric oscillator (OPO), with a tunable frequency range from 2600 to 6800 cm^{-1} and a resolution of 1.5 cm^{-1}. Precise electronic triggering allowed the intersection of the ion packets with the laser beam. If the laser frequency was resonant with the molecular vibrational transition, the clusters would absorb the infrared photons and undergo vibrational predissociation to fragment ions. Fragment ions were separated from the parent ions by a reflectron energy analyzer, and detected by a microchannel plate detector. Action spectra were recorded by measuring the predissociation signal as a function of OPO wavelength. Depending on the photofragment intensity, scans of 1000-8000 shots per point were performed for signal averaging. Background ion signal, primarily caused by unimolecular dissociation of metastable parents in the TOF chamber, was subtracted to obtain the actual photodissociation signal. Spectra were normalized to the laser fluence to correct for relative intensity. The OPO output was calibrated by a monochromator and a photoacoustic cell (see Chapter 2).

3.3 RESULTS

A typical TOF mass spectrum of hydrated cyanide clusters, $CN^-\cdot(H_2O)_n$, is shown in Figure 1. The cluster distribution could be altered by adjusting expansion conditions (stagnation pressure, pulse width and gas mixture), electron beam energy and alignment,

and the nozzle-skimmer distance for ion extraction. Consistent clustering conditions were maintained and monitored by measuring the metastable fragmentation (Table2). The infrared spectra of mass-selected $CN^-\cdot(H_2O)_n$ for n = 2-6 were recorded in the 3000-3850 cm^{-1} region. Only one photodissociation channel, the loss of a water molecule, was observed in our experiments. A summary of the observed vibrational frequencies is given in Table 3.

3.3.1 Vibrational Predissociation Spectra of $CN^-\cdot(H_2O)_n$, n =2-6

The vibrational predissociation spectra of $CN^-\cdot(H_2O)_n$, n =2-6, were shown in Figures 2 to 6. All the clusters exhibited a weak absorption around 3720 cm^{-1}, which was assigned to a free OH stretch of water ligands in the hydrated ion clusters.

Figure 2 shows the infrared predissociation spectrum of $CN^-\cdot(H_2O)_2$. In addition to the 3717 cm^{-1} band (free OH stretch), the observed spectrum exhibited a strong absorption at 3200 cm^{-1} and a shoulder-like feature at 3335 cm^{-1}. The spectrum also displayed a broad band absorption spanning from 3050 to 3550 cm^{-1}. The bands at 3200 and 3345 cm^{-1} were both significantly red-shifted relative to the free OH stretch, indicating donor-type hydrogen bonding to the ion core.

The infrared spectrum of the cluster $CN^-\cdot(H_2O)_3$ exhibited five distinct bands in the region 3000-3850 cm^{-1} (Figure 3). The strong bands at 3155 and 3230 cm^{-1} suggested the formation of two ionic hydrogen bonds. They were close to the 3200 cm^{-1} peak in n = 2. A broader absorption appeared at 3345 cm^{-1}, and probably corresponded to the shoulder feature observed in the same region in n = 2. Another peak was located at 3550 cm^{-1}. The free OH stretch appeared at 3725 cm^{-1}.

For the $CN^-\cdot(H_2O)_4$ (Figure 4) clusters, the low frequency doublet band were washed out and became an intense absorption at 3210 cm^{-1} superimposed on a broad feature. Two other peaks appeared at 3365 cm^{-1} and 3600 cm^{-1}, in addition to the free OH stretch at 3720cm^{-1}.

For n = 5 and 6 (Figures 5 and 6), the infrared spectra displayed qualitative changes from those of smaller clusters. The peaks in 3000-3450 cm^{-1} region were washed out and became a broad unresolved band. More prominently the major absorption intensity now appeared at around 3500 cm^{-1}.

3.3.2 Vibrational Predissociation Spectra of n =4 under Hot and Cold Conditions

In the case of $CN^-\cdot(H_2O)_4$, two sets of infrared predissociation spectrum were taken under different clustering conditions. They corresponded to a significant difference in cluster temperature, as was reflected from the percentage of parent ions undergoing metastable dissociation (Table 2) in the TOF mass spectrometer. A comparison of two infrared spectra corresponding to 0.1% (cold clusters) and 1.5% (hot clusters) metastable dissociation is shown in Figure 7. Under the high-temperature condition, the absorption was red-shifted to below 3000 cm^{-1}. Two sharp bands remained in the region available in our experiments. Such a significant change in the infrared spectrum suggested a different entity for the ionic core. We tentatively assigned the "hot" spectrum to $OH^-(HCN)\cdot(H_2O)_3$ cluster, with the peaks at 3225 and 3725 cm^{-1} corresponding to the hydrogen-bonding CH stretch of HCN ligand and the free OH stretch of water ligand, respectively.

3.4 DISCUSSION

3.4.1 Review of Ab Initio Calculations on $CN^-(H_2O)_{1-3}$ by S. S. Xantheas

Xantheas and coworkers[28] recently performed an *ab initio* study on $CN^-(H_2O)_n$ clusters. They calculated the energies and structures for n = 1 to 3 at MP2/aug-cc-p-VDZ level, and predicted the IR absorption spectra for n =1 and 2.

The calculations showed that the potential energy surface (PES) for binding water molecules around CN^- core is extremely flat. For n = 1, they obtained two minimum-energy structures with the water molecule forming a linear hydrogen bond to the N and C ends, respectively. Their energy difference was less than 1 kcal/mol, with the stability order reversed upon the inclusion of zero-point vibrational energy (ZPVE). The barrier for interconversion between the two isomers was only 2.3 kcal/mol. Despite the similarities in their energies, the two isomers were predicted to have qualitative different infrared absorption spectra. The ionic hydrogen-bonded OH stretch of the N-binding structure was calculated to be about 3050 cm^{-1}. The same OH stretch was 118 cm^{-1} further to the red in the C-binding structure. The intensity of free OH stretch at 3890 cm^{-1} was about 40 times weaker than that of the ionic bonds.

In the case of $CN^-(H_2O)_2$, three minina of nearly identical energy (within 2 kcal/mol) were located in the PES. They corresponded to: (1) one water molecule hydrogen-bonding to both N and C ends separately; (2) two water molecules hydrogen-bonding to the N end and with each other; and (3) two water molecules hydrogen-bonding to the C end and with each other. In structure **1**, the two ionic OH stretches were calculated to be in 3200-3300 cm^{-1} region. The C-end absorption band was ~107 cm-1 red-shifted relative to the N-end band. The free OH stretch was about 12 times weaker

than the N-end ionic OH stretch. For both structures **2** and **3**, only one ionic OH stretch in 3000-3300 cm^{-1} region was predicted. The frequency of the C-binding isomer was located 192 cm^{-1} to the red of the N-binding isomer. The peak intensity of free OH stretch was enhanced to about one fifth of the ionic OH stretches.

For n =3, at least 3 minimum-energy structures were predicted. The first two structures indicated that all three water molecules were bound only to one end of the CN^- core, and formed a cyclic network among themselves. The third isomer consisted of 2 water ligands on the N-site, and one water ligand bridging the water network to the C-site. All the structures were within 3 kcal/mol. No predicted IR spectra were reported.

One should caution that the predicted energies of the different isomers in n = 1-3 were only within a few kcal/mol. As there was no basis-set superposition-error corrections, the relative orders of the energy could not be guaranteed.

3.4.2 Peak Assignment for n = 2 to 6

A. $CN^-\cdot(H_2O)_2$

Various theoretical calculations[17,20,28] suggest that the PES around the CN^- core is extremely flat for hydration. Multiple isomers, with energy difference less than a few kcal/mol, are possible in clusters predicted in calculations, can account for the broad absorption features in n = 2. The bands from 3000 to 3500 cm^{-1} indicate substantial inhomogenous broadening (the presence of multiple isomers) for the ionic OH stretches. The existence of multiple isomers is also apparent at the free OH stretch, where three or more bands may be present within a bandwidth of 50 cm^{-1} FWHM. Another contribution to peak broadening is the high temperature of clusters. As the efficiency of evaporative

cooling[30] is limited by the binding energy of evaporating ligands, one may expect a higher temperature for smaller hydrated clusters. The internal energy available will allow the clusters to sample more configurations and thus lead to spectral broadening.

Two shaper bands superimpose onto the broad feature. The peaks at 3200 cm^{-1} and the shoulder at 3335 cm^{-1} suggest the presence of two distinct binding sites for ionic hydrogen bonding. One possible assignment is the hydrogen bonding of water molecules at the N and C sites. Due to the difference in electronegativity, the negative charge in CN^- will be preferentially shifted to the N end.[26] The interaction of N end with the water molecule will be significantly electrostatic in nature. As the C end is almost isoenergetic for the binding of water molecules, the hydrogen-bonding interaction on the C end will have more covalent character. This is also consistent to the fact that a proton transfer from water to the C site will lead to the formation of a stable HCN molecule, while a proton transfer to the N site will only to lead the unstable CNH. One may therefore expect a more significant lengthening of the OH bond when the water is bounded to the C end. That in turns will lead to a larger red-shifting in the OH stretching frequency. This frequency order agrees with the *ab initio* calculations by Xantheas and coworkers[28]. Their calculations predict a splitting of 118 cm^{-1} for these binding sites in $n = 1$, and 107 cm^{-1} for a structure in which the water molecules bind separately to C and N ends at $n = 2$ (Structure **1**). However, a frequency difference of 192 cm^{-1} is expected between the isomers of both water molecules binding to the same site (Structures **2** for C binding and **3** for N binding). Our experimental vale of 135 cm^{-1} is in better agreement with the structure **1**. Alternatively one of the bands may correspond to the bending overtone of one of the water molecules. However, that would require a comparable intensity of the

bending overtone to the bonded OH stretch. This situation is possible if there is strong Fermi resonance resulting from accidental near degeneracy.[4g] Further experimental or computational evidence is needed to support this argument. Currently we tentatively assign the 3200 and 3335 cm^{-1} peaks to OH stretches of one water molecule binding to C and N ends of the CN^- core, respectively.

B. $CN^-\cdot(H_2O)_3$

In $CN^-\cdot(H_2O)_3$, the peak at 3200 cm^{-1} becomes a strong doublet with maxima at 3155 and 3230 cm^{-1}. This band is the evidence for at least two strong ionic hydrogen bonds. The splitting of 75 cm^{-1} is smaller than the predicted frequency difference between the C-binding and N-binding OH stretches, either in $n = 1$ (118 cm^{-1}) or $n = 2$ (107 cm^{-1}, Structure **1**). Such a splitting is not predicted in structures where two water ligands are bound to the same bind site (Structures **2** and **3** of $n = 2$). However, a similar splitting (72 cm^{-1}) is observed in the ionic OH stretches of $Cl^-\cdot(H_2O)_2$, in which two water ligands are bound to the same ionic center[3a]. The Fermi resonance of an ionic OH stretch with the bending overtone of the water molecules is also possible, but again one may expect a much weaker feature than the ionic OH stretch. As the doublet is located very close to the C-binding OH stretch in $n = 2$, we tentatively assign these bands to the hydrogen bonding of two water molecules binding to the C-end.

The N-binding OH stretch at 3345 cm^{-1} remains in $n = 3$, and the shoulder-like feature becomes a more prominent band. It indicates the hydrogen bonding of a water molecule at the N-end. The appearance of the 3550 cm^{-1} peak also suggests the presence of hydrogen bonding among the water molecules. Interesting the free OH stretch observed at 3125 cm^{-1} is considerably sharper than that in $n = 2$. In fact, the spectral

features of n = 3 are in general sharper and better resolved than those of n = 2. One may conjure the following reasons for these observations: (a) Due to higher efficiency of evaporative cooling, the cluster temperature is lower in n = 3 than n =2; (b) the interlocking of three water molecules around the ellipsoid core may result in more rigid structure. In summary, our experimental data is in reasonable agreement with the structure in which two water molecules are hydrogen-bonded to the C-end and each other, and the third water bound both to the N-end and the neighboring water molecules. One should note that multiple isomers are definitely possible in the clusters, and the internal energy will probably lead to the sampling of various configurations. And also, both of the ionic OH stretches are slightly red-shifted relative n = 2, indicating a possible enhancement of hydrogen-bonding due to the additional water molecule. A possible mechanism may involves a cooperative effect in which the binding of water to the polarizable CN^- ion induces a dipole that favors and is enhanced by the binding of a second water to the same side of the ion[3a,31].

C. $CN^-\cdot(H_2O)_4$

The infrared spectrum of $CN^-\cdot(H_2O)_4$ resembles that of n =2 more than n = 3. The broad band features most probably suggest the co-existence of multiple isomers. As the size of hydrated clusters increases, the number of isomeric structures will increase considerably[3a,4b,20,28]. Given that the evaporative cooling is limited by the binding energy of water ligands, the internal energy available will allow the clusters to access various low-lying isomers. This situation agrees with the observation of broad absorption for ionic H-bonds from 3000 to 3500 cm^{-1}, and the water-water H-bonds from 3550 to 3675 cm^{-1}. The characteristic absorptions for C-site binding at 3210cm^{-1} and N-site binding at

3365 cm^{-1} are still observed in the spectrum. They are slightly blue-shifted relatively the corresponding peaks in n = 3, indicating a possible weakening of the ionic H-bond as more solvent molecules are bound to the ion core[3a,4b]. The free OH stretch at 3720 cm^{-1} also implies that not all OH bonds are involved hydrogen-bonding networks.

D. $CN^-\cdot(H_2O)_{5\text{-}6}$

Upon transiting to n = 5 and 6, there is a qualitative difference in the general appearance of the spectra. The infrared spectra for both clusters are dominated by absorption spanning frequencies from 3450 to 3650 cm^{-1}. While the free OH stretch remains evident in both spectra, the C-binding peak at 3225 cm^{-1} is only barely discernible and the N-binding peak at ~3350 cm^{-1} becomes unidentifiable. The intensity maxima of OH stretches are now shifted to the double-donor region, indicating extensive hydrogen bonding among the water ligands. The reduction of relative intensity for the ionic OH stretches (which are usually the strongest) may also suggest the breakage of ionic hydrogen bonds. A possible structure to account for these observations is that a ring-like network is formed between the water molecules, and the anion is "surface-bound" onto the water aggregate. Such a behavior has also been observed in the related of systems $X^-\cdot(H_2O)_n$ (X = Cl [3a], Br and I [4b]; $1 \leq n \leq 6$). The surface solvation for these systems is also supported by calculations[32,33]. However, one should caution that these large clusters probably contain significant amount of internal energy, and the broad profile may result from a fluctuating ensemble.

3.4.3 Intramolecular Proton Transfer at n = 4?

In $CN^-\cdot(H_2O)_4$, we observed a dramatic change in the infrared predissociation spectrum when the ions were produced under different source conditions (Figure 7). While the "cold" clusters display hydrogen-bonded OH stretches in the 3100-3600 cm^{-1} region, the intensity maximum in absorption spectrum of "hot" clusters is red-shifted to below 2900 cm^{-1}. Only two sharp bands remain in the region of 2900-3850 cm^{-1}. The first peak at 3725 cm^{-1} corresponds to the free OH stretch. The second peak is located at 3225 cm^{-1}, close to the C-binding peak at 3210 cm^{-1} of the cold clusters.

Such a significant change in the infrared spectrum is quite puzzling. As internal energy of the cluster increases, one may expect an increase in the inhomogenous broadening caused by ensemble fluctuation. Nevertheless, the spectral features corresponding to CN^- core would remain. The red-shifting of the absorption maximum to below 3000 cm^{-1} suggests the presence of a different ion center with stronger ionic hydrogen bonds. We tentatively propose that the "hot" spectrum belongs to $OH^-(HCN)\cdot(H_2O)_3$ clusters instead of $CN^-\cdot(H_2O)_4$. With OH^- as the hydration core, the spectral pattern would agree with *ab initio* calculations[34], which predict that the ionic OH stretches would be located between 2000 to 3000 cm^{-1}. The band at 3225 cm^{-1} is then tentatively assigned to the CH (ν_2) stretch in a hydrogen-bonded HCN moiety. The peak is close to the hydrogen-bonded ν_2 in HCN dimer at 3242 cm^{-1} [38]. The absence of an absorption band in 3500-3650 cm^{-1} regions would indicate that the water-water hydrogen bondings are broken by the high internal energy. Alternatively, there could be a co-existence of isomeric forms with both OH^- and CN^- as ion cores. The 3225 cm^{-1} would then correspond to the C-binding OH stretch (3210 cm^{-1}) in hydrated CN^- clusters. However, the peak in hot spectrum is considerably sharper than in the cold spectrum, and

there is no indication of other spectral signatures for ionic hydrogen bonding in 3100-3500 cm^{-1} region. Thus the assignment of 3225 cm^{-1} peak to C-binding OH stretch is less probable.

For the unsolvated anions, the proton transfer is thermodynamically unfavorable. The heat of reaction for:

$$CN^- + H_2O \rightarrow OH^- + HCN \qquad (2)$$

is 42.4 kcal/mol.[36] However, this energy penalty can be partially offset by the preferential hydration of OH^- over CN^-. Table 1 shows the hydration energies ($-\Delta H_{n,n-1}$) for these anions. The stabilization energy is defined as the energy gained from hydration of OH^- over CN^-. At $n = 4$, the stabilization energy of 25.8 kcal/mol would reduce the heat of reaction (2) to 16.6 kcal/mol. Furthermore, HCN binds more strongly to anions than H_2O, further stabilizing the solvated OH^- product. Together with the high internal energy, the stabilization of $OH^-(H_2O)_m(HCN)$ could allow the proton transfer to occur in hot clusters. We caution that we did not detect the predissociation signal of the loss of HCN molecule from $OH^-(HCN)\cdot(H_2O)_3$ clusters in our experiments. The higher binding energy of HCN to the anion core relative to H_2O should lead to a preferential loss of H_2O upon IR excitation. (See Table 4 for a comparison of their binding energies to typical anions.)

In summary, we have observed a significant transformation in the IR spectrum for $n = 4$ under different clustering conditions. We propose an intramolecular proton transfer to account for the spectral behavior. However, further evidence is needed to establish definitively that such a reaction has occurred. Relevant experiments include observations of the ionic H-bonds corresponding to OH^- core, and the detection of HCN moiety in the clusters.

3.5 SUMMARY

We have reported the infrared predissociation spectroscopy of $CN^-\cdot(H_2O)_n$ (n = 2 - 6) clusters in the region of 2950 - 3850 cm^{-1}. With the aid of *ab initio* calculations, the characteristic hydrogen bondings for the C-site and N-site binding, and among the water molecules are identified for n = 2 to 4. Significant inhomogenous broadening are generally displayed in the vibrational spectra, indicating the presence of multiple isomers of similar energies. A qualitative difference in the IR spectrum, however, is observed for n = 5 and 6. The spectral transition implies that the anion is surface-bound onto the water aggregates in larger clusters. For n = 4, a dramatic transformation in the spectrum is observed when the clusters are generated under the conditions of high internal temperature. The spectral features suggests the possibility of intramolecular proton transfer and the presence of $OH^-(HCN)\cdot(H_2O)_3$.

3.6 REFERENCES

1. H. Haberland (Ed.), *Clusters of Atoms and Molecules II*, Springer-Verlag, Berlin, Germany, 1994.

2. For cationic clusters, see for example: (a) J.-H. Choi, K. T. Kuwata, Y. B. Cao , B.-M. Haas, and M. Okumura, *J Phys. Chem. A*, **101**, 6753 (1997); (b) Y. B. Cao, J.-H. Choi, B.-M. Haas, and M. Okumura, *J. Phys. Chem.*, **98**, 12176 (1994); (c) Y. B. Cao, J.-H. Choi, B.-M. Haas, M. S. Johnson, and M. Okumura, *J. Chem. Phys.*, **99**, 9307 (1993); (d) Y. B. Cao, J.-H. Choi, B.-M. Haas, M. S. Johnson, and M. Okumura, *J. Phys. Chem.*, **97**, 5215 (1993).

3. (a) J.-H. Choi, K. T. Kuwata, Y.-B. Cao, and M. Okumura, *J. Phys. Chem. A*, **102**, 503 (1998); (b) . S. Johnson, K. T. Kuwata, C.-K. Wong, and M. Okumura, *Chem. Phys. Lett.*, **260**, 551 (1996).

4. (a) P. Ayotte, C. G. Bailey, J. Kim, and M. A. Johnson, *J. Chem. Phys.*, **108**, 444 (1998); (b) P. Ayotte, C. G. Bailey, G. H. Weddle, and M. A. Johnson, *J. Phys. Chem. A*, **102**, 3067 (1998); (c) P. Ayotte, J. A. Kelley, S. B. Nielsen, and M. A. Johnson, *Chem. Phys. Lett.*, **316**, 455 (2000); (d) P. Ayotte, S. B. Nielsen, G. H. Weddle, and M. A. Johnson, *J. Phys. Chem. A*, **103**, 10665 (1999); (e) P. Ayotte, G. H. Weddle, and M. A. Johnson, *J. Chem. Phys.*, **110**, 7129 (1999); (f) P. Ayotte, G. H. Weddle, J. Kim, and M. A. Johnson, *Chem. Phys.*, **239**, 485 (1998); (g) P. Ayotte, G. H. Weddle, J. Kim, and M. A. Johnson, *J. Am. Chem. Soc.,* **120**, 12361 (1998); (h) P. Ayotte, G. H. Weddle, J. Kim, J. Kelley, and M. A. Johnson, *J. Phys. Chem.*, **103**, 443 (1999); (i) C. G. Bailey, J. Kim, C. E. H. Dessent and M. A. Johnson, *Chem. Phys. Lett.*, **269**, 122 (1997); (j) S. B. Nelson, P. Ayotte, J. A. Kelley, and M. A. Johnson, *J. Chem. Phys.*, **111**, 9593 (1999); (k) S. B. Nelson, P. Ayotte, J. A. Kelley, G. H. Weddle, and M. A. Johnson, *J. Chem. Phys.*, **111**, 10464 (1999); (l) J. M. Weber, J. A. Kelley, S. B. Nelson, P. Ayotte, and M. A. Johnson, *J. Chem. Phys.*, **111**, 9443 (1999).

5. (a) O. M. Cabarocs, C. J. Weinheimer, J. M. Lisy, and S. S. Xantheas, *J. Chem. Phys.*, **110**, 5 (1999); (b) O. M. Cabarocs, C. J. Weinheimer, T. J. Martinez, and J. M. Lisy, *J. Chem. Phys.*, **110**, 9516 (1999).

6. (a) P. S. Weiser, D. A. Wild, and E. J. Bieske, J. Chem. Phys., **110**, 9443 (1999); (b) P. S. Weiser, D. A. Wild, and E. J. Bieske, *Chem. Phys. Lett.*, **299**, 303 (1999); (c) P. S. Weiser, D. A. Wild, P. P. Wolynec, and E. J. Bieske, *J. Phys. Chem.*, **104**, 2562 (2000).

7. J. M. Weber, J. A. Kelley, S. B. Nielsen, P. Ayotte, and M. A. Johnson, *Science*, **287**, 2461 (2000).

8. T. N. Truong and E. V. Stefanovich, *Chem. Phys.*, **218**, 31 (1997).

9. C. W. Bauschlicher Jr., M. Sodupe, and H. Partridge, *J. Chem. Phys.*, **96**, 4453 (1992).

10. J.-H. Choi, *Ph.D. Thesis*, California Institute of Technology (1995).

11. K. T. Kuwata, *Ph.D. Thesis*, California Institute of Technology (1998).

12. See, for example, J. E. Huheey, *Inorganic Chemistry: Principles of Structure and Reactivity*, 3rd Ed., Harper & Row, New York, U.S.A., 1983.

13. See, for example, (a) D. S. Marynick, L. Throckmorton, and R. Bacquet, *J. Am. Chem. Soc.*, **104**, 1 (1982); (b) K. Imi , N. Yanagihara, and K. Utimoto, *J. Org. Chem.*, **52**, 1013 (1987); and the references therein.

14. J. D. Payzant, R. Yamdagni, and P. Kebarle, *Can. J. Chem.*, **49**, 3308 (1971).

15. J. W. Larson and T. B. McMahon, *J. Am. Chem. Soc.*, **109**, 6230 (1987)

16. J. W. Larson, J. E. Szuleiko, and T. B. McMahon, *J. Am. Chem. Soc.*, **110**, 7604 (1988).

17. J. Gao, D. S. Garner, and W. L. Jorgensen, *J. Am. Chem. Soc.*, **108**, 4784 (1986).

18. M. Meot-Ner (Mautner), S. M. Cybulski, S. Scheiner, and J. F. Liebman., *J. Phys. Chem.*, **92**, 2738 (1988).

19. M. Meot-Ner (Mautner) and C. V. Speller, (a) *J. Phys. Chem.*, **93**, 3663 (1989); (b) *J. Phys. Chem.*, **93**, 6580 (1989).

20. T. Ikeda, K. Nishimoto, and T. Asada, *Chem. Phys. Lett.*, **248**, 329 (1995).

21. G. Eaton, A. S. Pena-Nunez, M. C. R. Symons, M. Ferrario, and I. R. McDonald, *Faraday Discuss. Chem. Soc.*, **85**, 237 (1985).

22. M. Ferrario, I. R. McDonald, and M. C. R. Symons, *Mol. Phys.*, **77**, 617 (1992).

23. R. Rey and H. T. Hynes, *J. Chem. Phys.*, **108**, 142 (1998)

24. M. Shiga and S. Okazaki, *J. Chem. Phys.*, **111**, 5390 (1999).

25. M. Shiga and S. Okazaki, *Chem. Phys. Lett.*, **292**, 431 (1998).

26. S. T. Howard, *Mol. Phys.*, 85, 395 (1995).

27. M. S. Johnson, *Ph.D. Thesis*, California Institute of Technology (1995).

28. S. S. Xantheas, Private Communication.

29. (a) K. Kim, K. D. Jordan and T. S. Zwier, *J. Am. Chem. Soc.*, **116**, 11568 (1994); (b) R. N. Pribble and T. S. Zwier, *Science*, **265**, 75 (1994).

30. C. E. Klots (a) *J. Chem. Phys.*, **83**, 5854 (1985); (b) *J. Phys. Chem.*, **92**, 5864 (1988); (c) *Z. Phys. D.*, **5**, 83 (1987).

31. C. W. Bauschlicher Jr., M. Sodupe, *J. Chem. Phys.*, **96**, 4553 (1992).

32. (a) S. S. Xantheas, *J. Phys. Chem.*, **100**, 9703 (1996); (b) S. S. Xantheas and T. H. Dunning, *J. Phys. Chem.*, **98**, 13489 (1994); (c) S. S. Xantheas and L. X. Dang, *J. Phys. Chem.*, **100**, 3898 (1996).

33. (a) L. Perera and M. L. Berkowitz, *J. Chem. Phys.*, **95**, 1954 (1991); (b) L. Perera and M. L. Berkowitz, *J. Chem. Phys.*, **96**, 8228 (1992); (c) L. Perera and M. L. Berkowitz, *Z. Phys. D.*, **26**, 166 (1993); (d) L. Perera and M. L. Berkowitz , *J. Chem. Phys.*, **99**, 4222 (1993); (e) L. Perera and M. L. Berkowitz, *J. Chem. Phys.*, **99**, 4236 (1993); (f) L. Perera and M. L. Berkowitz, *J. Chem. Phys.*, **100**, 3085 (1994); (g) L. S. Stremaniak L. Perera and M. L. Berkowitz; *Chem. Phys. Lett.*, **218**, 377 (1994); (h) I.-C. Yeh L. Perera and M. L. Berkowitz, *Chem. Phys. Lett.*, **264**, 31 (1994).

34. S. S. Xantheas, *J. Am. Chem. Soc.*, **117**, 10373 (1995).

35. (a) M. Meot-Ner (Mautner) and C. V. Speller, *J. Phys. Chem.*, **90**, 6616 (1986); (b) M. Meot-Ner (Mautner) and L. W. Sieck, *J, Am. Chem. Soc.*, **108**, 7525 (1986); (c) M. Meot-Ner (Mautner), *J, Am. Chem. Soc.*, **110**, 3854 (1988).

36. S. G. Lias, J. E. Bartmess, J. F. Liebman, J. L. Holmes, R. D. Levin, and W. G. Mallard, *J. Phys. Chem. Ref. Data*, **17**, Suppl. 1 (1988).

37. R. G. Keesee and A. W. Castleman, Jr., *J. Phys. Chem. Ref. Data*, **15**, 1011 (1986).

38. (a) K. W. Jucks and R. E. Miller, *J. Chem. Phys.*, **88**, 6059 (1988); (b) K. Nauta and R. E. Miller, *J. Chem. Phys.*, **111**, 3426 (1999).

Table 1 Hydration energies, $-\Delta H_{n,n-1}$ (in kcal/mol), for CN^- and OH^-. The stabilization energy is defined as ΔH (CN) - ΔH (OH).

n	CN^- [19]	OH^- [35]	Stabilization
1	14.6	26.8	12.2
2	11.7	17.6	18.1
3	10.7	16.2	23.6
4	9.8	12.0	25.8
5	-	12	-

Table 2 Typical percentage of parent $CN^-\cdot(H2O)_n$ clusters undergoing metastable dissociation in the field free flight path of the TOF mass spectrometer.

n	%	
2	0.07 %	
3	0.08 %	
4	0.1 %	(cold)
	1.5 %	(hot)
5	0.3 %	
6	0.4 %	

Table 4 Summary of the observed peak positions in the infrared vibrational spectra of the $CN^-(H_2O)_n$ clusters.

n	Frequency (cm^{-1})
2	3200, 3345, 3718
3	3155, 3230, 3345, 3545, 3725
4	3210, 3350, 3600, 3720 (cold)
	3225, 3725 (hot)
5	3225, 3460, 3725
6	3290, 3600, 3730

Table 3 A comparison of binding energies (in kcal/mol) of HCN and H_2O to some typical anions.

	HCN [35]	H_2O [37]
F^-	39.5	23.3
Cl^-	21.9	14.7
CN^-	20.7 [19]	14.6
Br^-	19.4	11.7
I^-	16.8	10.2

3.7 FIGURE CAPTIONS

Figure 1 Typical TOF mass spectrum for $CN^-\cdot(H_2O)_n$ clusters.

Figure 2 Infrared predissociation spectrum of $CN^-\cdot(H_2O)_2$.

Figure 3 Infrared predissociation spectrum of $CN^-\cdot(H_2O)_3$.

Figure 4 Infrared predissociation spectrum of $CN^-\cdot(H_2O)_4$.

Figure 5 Infrared predissociation spectrum of $CN^-\cdot(H_2O)_5$.

Figure 6 Infrared predissociation spectrum of $CN^-\cdot(H_2O)_6$.

Figure 7 Infrared predissociation spectrum of $CN^-\cdot(H_2O)_4$ generated in "hot" conditions.

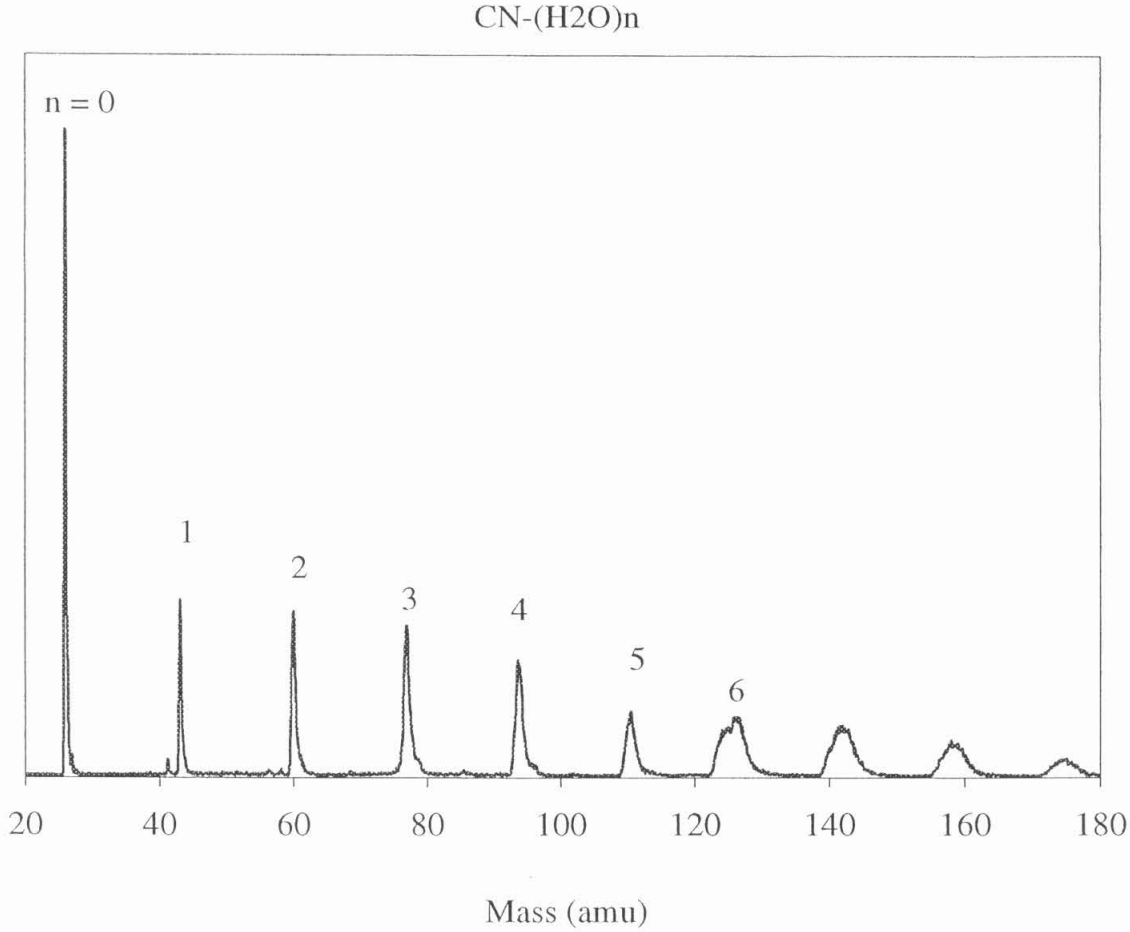

Figure 1

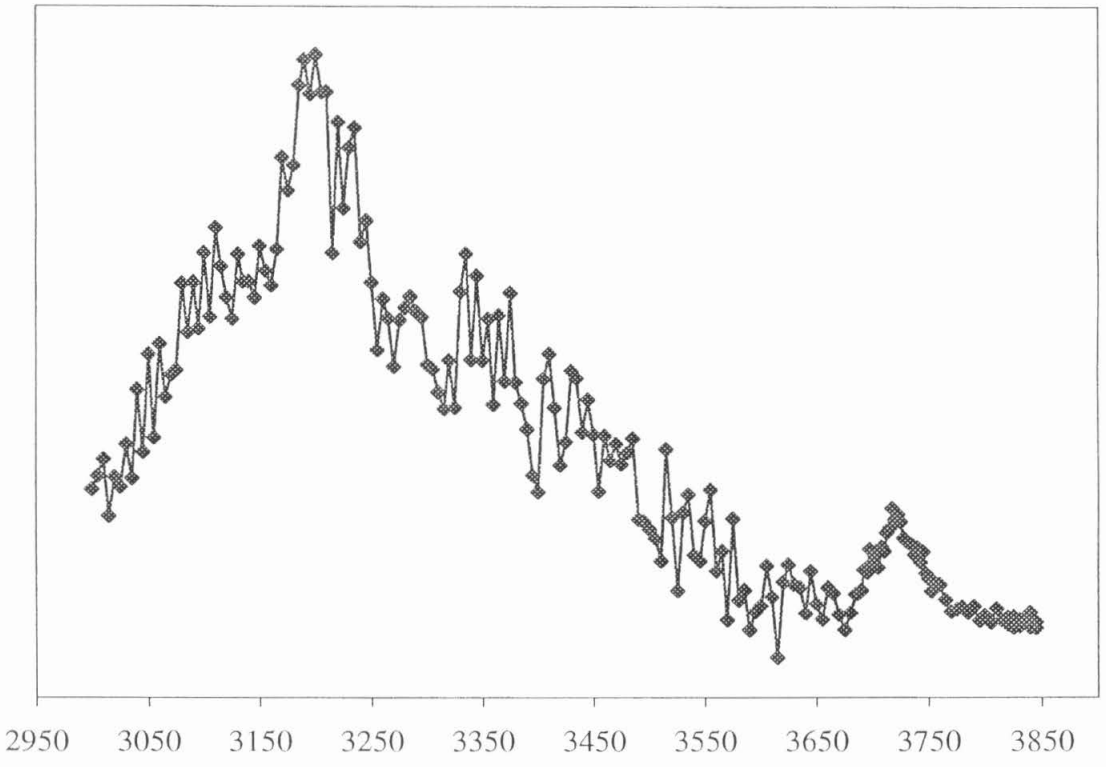

Figure 2

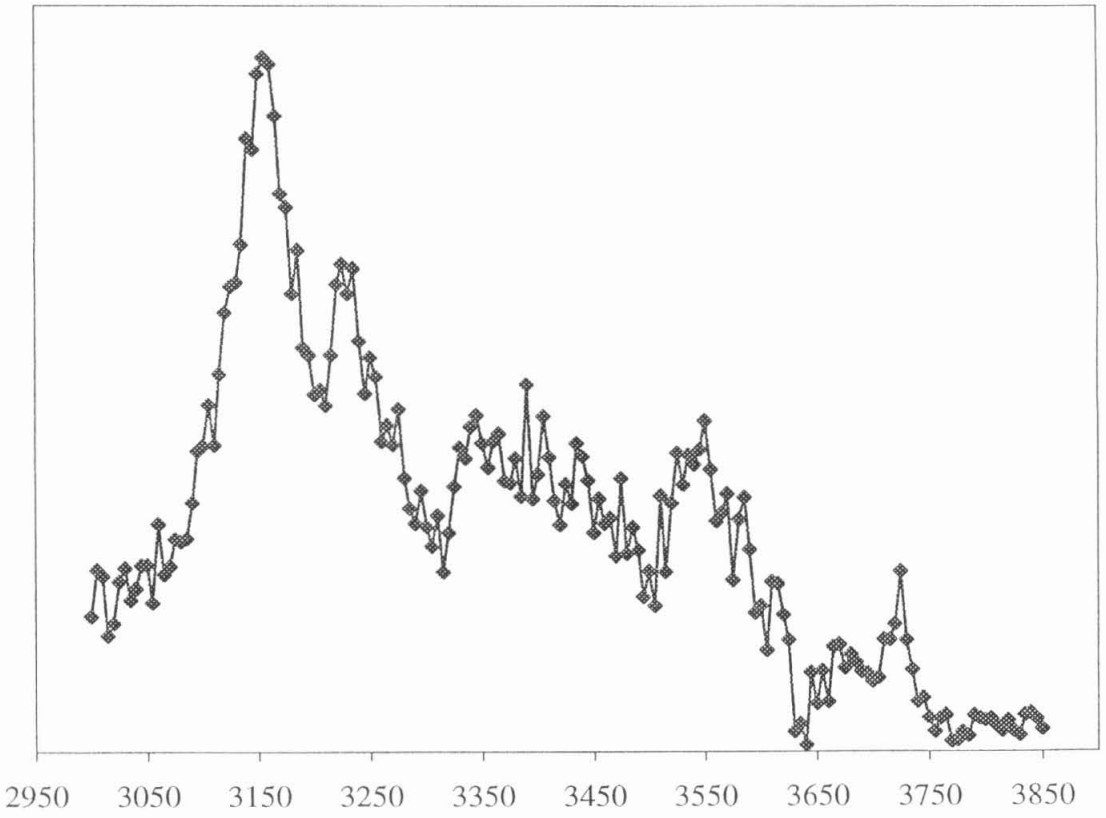

Figure 3

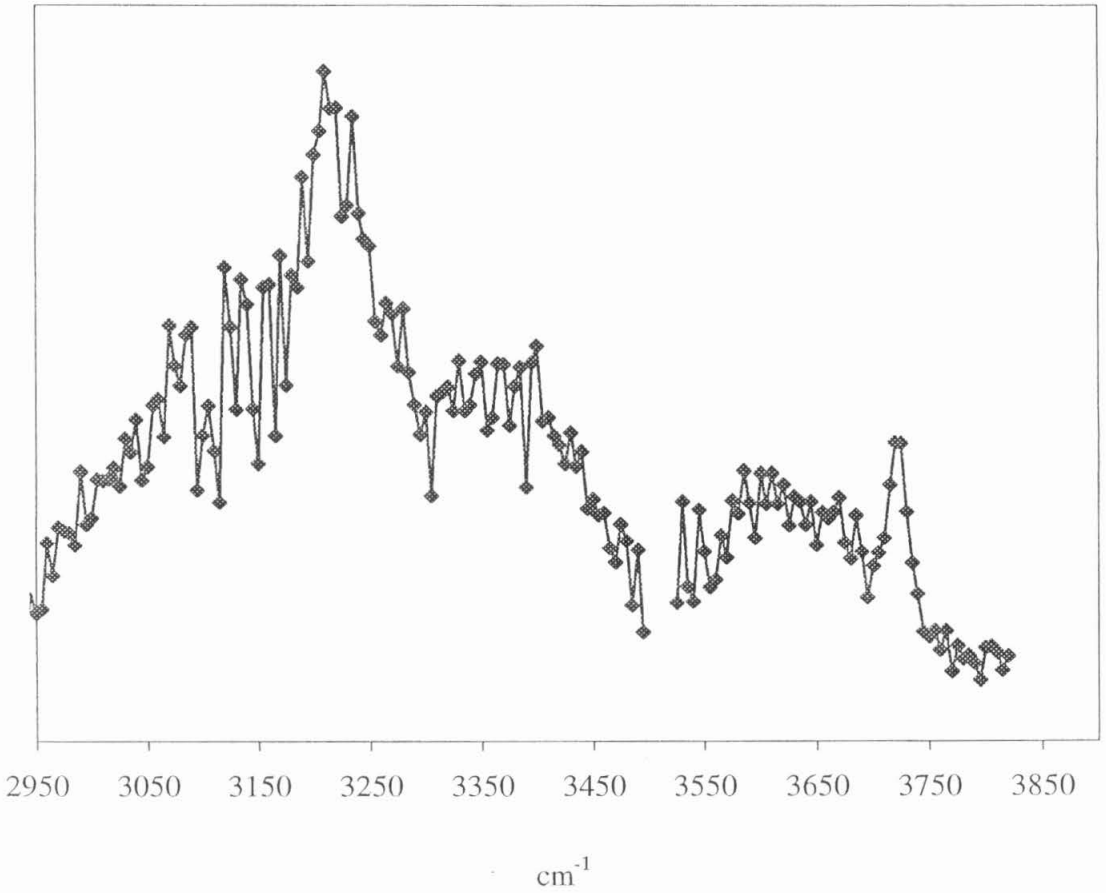

Figure 4

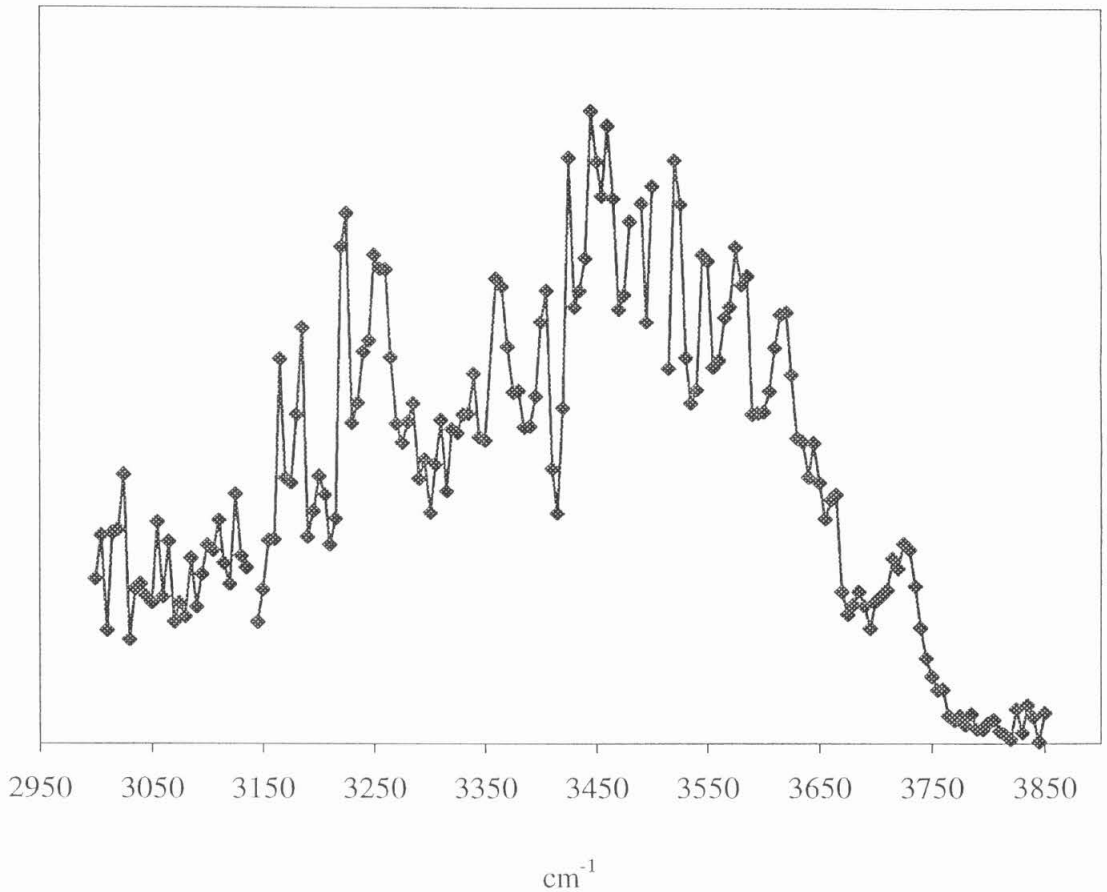

Figure 5

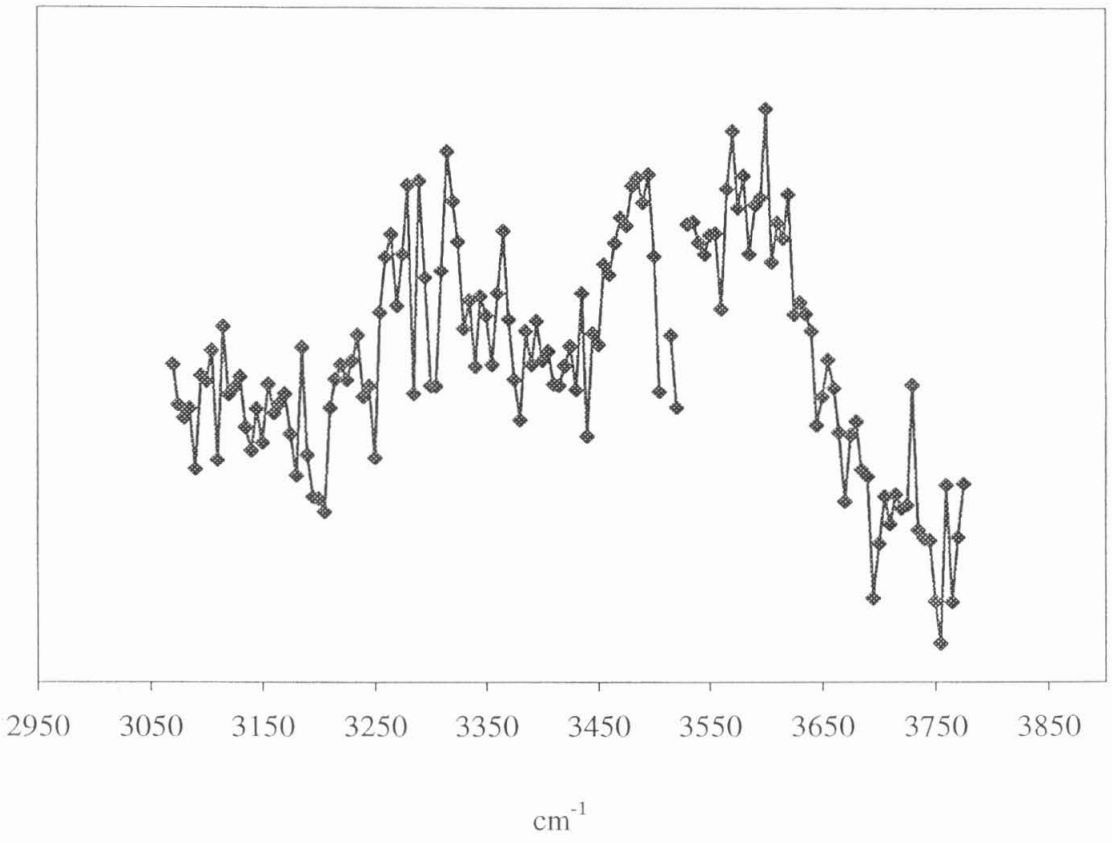

Figure 6

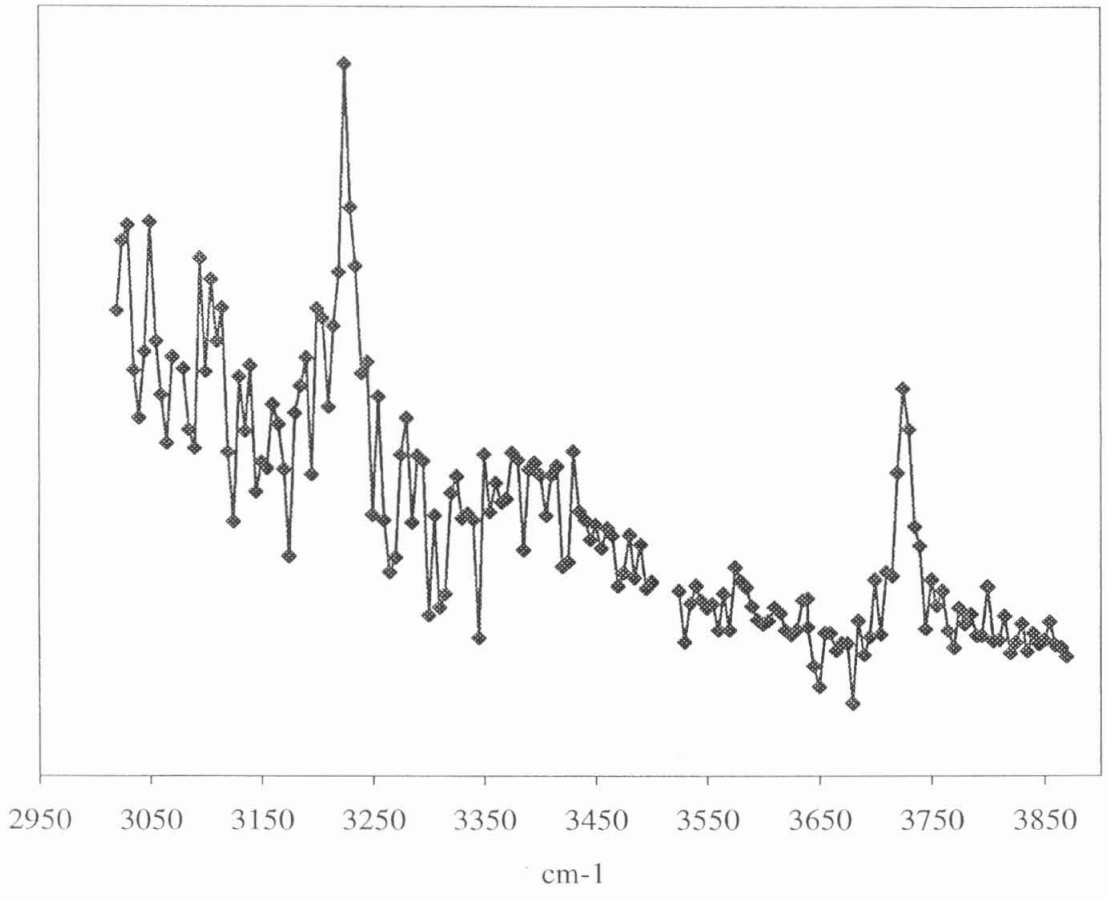

Figure 7

CHAPTER 4

Infrared Vibrational and *Ab Initio* Studies of Halide-Ammonia Complexes: $X^-\cdot(NH_3)$, X = Br and I

4.1 INTRODUCTION

Ion solvation is a fundamental phenomenon in chemical systems. In order to understand the chemical behaviors of ionic species in solution, it is important to examine the nature of ion-solvent interactions. A useful approach to elucidate details of these interactions is through the studies of ion-molecule complexes in the gas phase. The simplicity of ion-molecule complexes allows a detailed investigation into intermolecular forces, and provides information on the interactions without interferences from the bulk environment. The investigation on larger clusters may also provide insights into the elementary processes of solvation.

In recent years there has been extensive interest in characterizing ionic clusters. Experimental techniques such as high-pressure mass spectrometry, ICR, photoelectron and vibrational spectroscopies are applied to solvated clusters to measure their thermodynamic, structural and electronic properties. Complementary studies from *ab initio* calculations provide theoretical input for the interpretation of experimental data. The combined efforts have proved to be useful in obtaining a detailed picture of ion-solvation behavior. One of major foci has been the hydrated halide clusters[1-16]. It has been shown that the structures of hydrated clusters depend on the competition between the hydrogen bondings of water molecules with the ionic center and the hydrogen bonding ligands themselves.

Apart from the ubiquity of water as a solvating medium, these systems represent an important model for the fundamental study of hydrogen-bonding interactions. As hydrogen bonding is operative in numerous chemical and biological systems, it will be of interest to extend the study to other molecules. One of the suitable choices is ammonia.

Ammonia is the simplest molecule in the amine family. It is the representative of amide and amino groups (-NH_2, -NH-) commonly found in molecular systems. Its hydrogen bonding with ionic species is of similar strength to hydration[17]. As in the case of water, the three protons allow the possibility of multiple hydrogen bonding with the ionic center and among the solvating molecules.

Thermodynamic measurements for associations of ammonia with halide ions have been reported for Cl^-, Br^- and I^-. Using ion cyclotron resonance, Larson and McMahon[18] reported a ΔG_{298} of 4.5 ± 0.2 kcal/mol. Combining an ΔS value estimated from A statistical mechanical model, they obtained a ΔH_{298} value of 10.5 ± 0.2 kcal/mol. Later on, Castleman and coworkers[19] employed high-pressure mass spectrometry and obtained ΔH_{298} values of 8.2 ± 0.1, 7.7 ± 0.1 and 7.4 ± 0.3 kcal/mol, and ΔS_{298} values of 15.4 ± 0.2, 19.1 ± 0.4 and 20.9 ± 1.0 cal/K·mol, for Cl^-, Br^- and I^-, respectively. These authors also performed electrostatic calculations to explore the relative energies of three possible isomers for the complexes: (1) a nearly linear hydrogen-bonded structure of C_s symmetry; (2) a C_s structure where the halide bisects the angle between two hydrogen atoms; and (3) an aligned-dipole structure of C_{3v} symmetry. For $F^-\cdot NH_3$, the bisecting structure was of the lowest energy. For other halide anions, the calculated energies for all three structures were within 0.3 kcal/mol. With the application of *ab* initio calculations at HF/4-31G level to F^- and Cl^- complexes, the geometry with one linear hydrogen bond was found to be the minimum structure.

Kaldor[20] re-examined the linear structure for F^- and Cl^- complexes at a more advanced level of theory. The single-and-double coupled clusters calculations (CCSD/ANO) provided similar results on geometries of the complexes as in the work of

Castleman and coworkers[19]. The binding energy was calculated to be 8.3 kcal/mol, which was in excellent agreement with the experimental value of 8.2 kcal/mol. The calculations also predicted the vertical ionization potentials (IP's) for $Cl^-\cdot NH_3$ to neutral $Cl\cdot NH_3$ and $Cl^-\cdot NH_3^+$ complexes. The calculated values were 3.88 and 6.36 eV, respectively. These numbers were also in good agreement with the experimental values of 4.0 and 6.45 eV measured from the photoelectron experiment by Markovich *et al*[21].

More recently, Bieske and coworkers[22] have performed an infrared (IR) vibrational study on $Cl^-\cdot NH_3$. They observed an intense IR absorption at 3140 cm^{-1}, and two weaker absorptions at 3270 and 3340 cm^{-1}. With the aid of high-level *ab initio* calculations (MP2/aug-cc-pVTZ), they assigned the structure to the linear C_s geometry with one ionic hydrogen bond. The 3140 cm^{-1} peak was assigned to the ionic NH stretch, the 3340 cm^{-1} peak to free NH stretch in the NH_3 moiety, and the 3270 cm^{-1} to a combination band of ionic NH stretch with a low frequency intermolecular mode. The calculated binding energy of 7.6 kcal/mol was in good agreement with experiments. The calculations also predicted the bifurcated structure to be a transition state 1.66 kcal/mol higher in energy than the minimum.

Kuwata of our group has also performed similar IR studies on the clusters of $Cl^-\cdot(NH_3)_n$, n =1-5.[23] Our experimental and *ab initio* results of n = 1 were in quantitative agreement with the work of Bieske and coworkers. For the larger clusters, the peak at ~3350 cm^{-1} remained, indicating the presence of free NH stretches in the solvating ligands. The ionic NH stretch gradually shifted to higher frequency as the size increased, suggesting a gradual weakening of the ionic hydrogen bonds. Two weaker features at

~3215 and ~3300 cm^{-1} became increasing intense with increasing clustering. They were assigned to the two components of NH_3 bending overtone ($2\nu_4$).

The success of vibrational studies on $Cl^-\cdot(NH_3)_n$ (n =1-5) has motivated us to extend the investigations to other halide ions. In this chapter, we will report the IR predissociation studies of $Br^-\cdot(NH_3)$ and $I^-\cdot(NH_3)_n$, (n =1-3) in the region of 3000 - 3400 cm^{-1}. *Ab initio* calculations on $Br^-\cdot(NH_3)$ and $I^-\cdot(NH_3)$ will also be reported to aid the interpretation of experimental results.

4.2 EXPERIMENTAL AND COMPUTATIONAL METHODS

The details of experimental arrangement have been discussed in Chapter 2 and other references[24,25], and only a brief account will be given here to provide the details specific to this experiment. The halide-ion clusters were generated by seeding vapor of halogenated compounds, CH_2Br_2 (99%, Aldrich) and CH_3I (99%, Aldrich), into a buffer gas at a stagnation pressure of ~1000 Torr. The chemicals were placed in a glass bubbler equipped along the gas line, and were cooled down to reduce the vapor pressures (CH_2Br_2 at -35 °C, partial pressure ≈ 1 Torr; CH_3I at -45 °C, partial pressure ≈ 10 Torr). The buffer gas employed was a mixture of CH_4/NH_3 (99.99%, Matheson) with the mixing ratio varying from 5:1 to 8:1. In general, higher NH_3 content led to a higher temperature of the clusters. The gas mixture was expanded into a vacuum chamber (10^{-6} Torr with no gas load) through a piezoelectric driven pulsed valve (nozzle dia. = 1.0 mm) at a repetition rate of 30 Hz (pulse width = ~200 μs). The piezoelectric disk was coated with fluorinated grease to prevent chemical damage to the crystal element. The gas

mixture was ionized by intersecting with a pulsed electron beam at the beginning of the supersonic expansion.

The arrangement of the pulsed electron source was guided by the design of Bieske *et al.*[26] The electrons were generated from a thoriated iridium filament (Duniway) positioned close to the molecular beam. The radial distance from the filament to the beam axis was about 1 cm. By sliding the pulsed valve backwards and forwards along the beam axis, the distance between the nozzle orifice and the ionization region could be adjusted. Typical distances were 2 to 10 mm along the beam direction. The filament was heated up by a current of 5-6 A. A pulsed voltage of -150 to -500 V was applied to the filament, with a typical pulse width of 30 μs. A repelling plate at about -700 V was located behind the filament to focus the electrons onto the gas. The entire assembly was shielded with stainless steel meshes. The cluster distribution could be altered by adjusting expansion parameters (stagnation pressure, pulse width and gas mixture), ionization conditions (energy, pulsed width and timing of the pulsed electron beam, and the distance between nozzle orifice and pulsed electron beam), and the nozzle-skimmer distance for ion extraction. Presumably the distribution reflected the temperature of the ionic clusters during the experiments. Consistent clustering conditions were maintained and monitored by measuring the metastable fragmentation. Typical percentage of metastable dissociation was 0.3-0.8% of the parent ions.

The resulting $X^-\cdot(NH_3)_n$ cluster ions were skimmed and entered a time-of-flight (TOF) chamber where the ions were extracted by a pulsed electric field (10 μs wide) and accelerated to -2.5 kV. The TOF mass spectrometer separated the clusters into spatially discrete mass packets, and a mass gate selected the ions of interest for pulsed infrared

irradiation (1-4 mJ/pulse). The radiation was generated from a Nd:YAG-pumped lithium niobate ($LiNbO_3$) optical parametric oscillator (OPO), with a tunable frequency range from 2600 to 6800 cm^{-1} and a resolution of 1.5 cm^{-1}. Precise electronic triggering allowed the intersection of the ion packets with the laser beam. If the laser frequency was resonant with a molecular vibrational transition, a small fraction of the clusters would absorb the infrared photons and undergo vibrational predissociation to form fragment ions. Fragment ions were separated from the parent ions by a reflectron energy analyzer, and detected by a microchannel plate detector. Action spectra were recorded by measuring the predissociation signal as a function of OPO wavelength. Depending on the photofragment intensity, scans of 1000-5000 shots per point were performed for signal averaging. Background ion signal, primarily caused by collision-induced dissociation of metastable parents in the TOF chamber, was subtracted to obtain the actual fragment signal resulted from infrared photodissociation. Spectra were normalized to the laser fluence to correct for relative intensity. The OPO output was calibrated by a monochromator and a photoacoustic cell.

Ab initio calculations were carried out on IBM RS6000/390 and SGI10000 workstations, using the Gaussian 94 package of programs[27]. For the system $Br^-\cdot(NH_3)$, calculations were performed at the second-order Møller-Plesset (MP2) level of theory, with a 6-311++G** level basis sets and correlation of all electrons. For $I^-\cdot(NH_3)$, same level of theory was employed except that the correlation of core electrons was neglected (frozen-core approximation). The computational resources were generously contributed by Professor Wai-Kee Li at The Chinese University of Hong Kong.

4.3 COMPUTATIONAL RESULTS AND DISCUSSION

The three geometries considered for the complexes $Br^-\cdot(NH_3)$ and $I^-\cdot(NH_3)$ are shown in Figures 1 and 2, respectively. They correspond to: 1) a C_s geometry with one near linear hydrogen bond between the anion and ammonia (**Ia**, **IIa**); 2) a C_s geometry with two hydrogen bonds and the halide bisecting the angle between two hydrogen atoms (**Ib**, **IIb**); c) a C_{3v}, aligned-dipole geometry with three hydrogen bonds (**IIIa** and **IIIb**). Comparison of structural parameters with experimental values is only possible for NH_3.[28] Table 1 shows the calculated properties for NH_3 at MP2 level with full and frozen-core correlation. The structural parameters are in good agreement with experimental data. The calculated results are similar in both levels of theory, supporting the reliability of frozen-core approximation for geometry optimization. Vibrational frequencies are consistently higher than experimental values. It is well known that these calculations consistently overestimate vibrational frequencies, partly due to the harmonic treatment of the vibrational motions. A scaling factor of 0.94 has been suggested for the level of theory[29] employed in our studies. However, the data of NH_3 display a range of values (0.88-0.98) for the scaling factor. One may expect a more pronounce deviation from the harmonic frequencies for hydrogen bonded NH stretches, where the contribution from anharmonicity is more significant.

4.3.1 $Br^-\cdot(NH_3)$

The optimized geometries for $Br^-\cdot(NH_3)$ complex are shown in Figure 1. While **Ia** is a minimum point of the potential energy surface, **Ib** and **Ic** are found to be transition states (TS) of first and second order respectively. **Ib** corresponds to the interconversion of

equivalent **Ia**'s through internal rotation. These results are similar to the calculations on $Cl^-\cdot(NH_3)$.[23,26] The calculated energies for the complexes are shown in Table 2. From the minimum geometry (**Ia**), the binding energy of $Br^-\cdot(NH_3)$ is predicted to be 7.8 kcal/mol. It is reduced to 7.0 kcal/mol upon including the correction of zero-point vibrational energy (ZPVE). Both values are in good agreement with the association enthalpy (7.7 ± 0.1 kcal/mol) measured from high-pressure mass spectrometry[19]. The respective energies of **Ib** and **Ic** relative to the C_s minimum are 1.2 and 1.4 kcal/mol. The energy order is reversed when ZPVE is included and the values are respectively reduced to 0.9 and 0.8 kcal/mol. Basis set superposition error (BSSE) were not computed.

The optimized structures of the three geometries are given in Table 3. For the minimum structure (**Ia**), the distance between Br and the shared proton is 2.617 Å. The hydrogen bond is nearly linear, with a Br-H-N angle of 163.0 The N-H bond with the shared proton is lengthened by 0.011 Å comparing with free ammonia. On the other hand, the non-hydrogen-bonded N-H bond lengths remain almost unchanged (lengthened only by 0.002 Å). The hydrogen bonds are significantly longer in **Ib** and **Ic**, with respective to Br-H distances of 3.056 and 3.395 Å. The N-H bond containing the shared proton in both **Ib** and **Ic** geometries (1.017 Å) remains close to the value of free ammonia (1.013 Å). The hydrogen-bond angle (Br-H-N) is 114.7° for **Ib** and 100.2° for **Ic**.

Table 4 shows the predicted vibrational frequencies of **Ia-c**, together with the symmetries and calculated infrared intensity (km/mol). In the region of 3000-3700 cm^{-1}, **Ia** displays two IR active vibrations. The 3438 cm^{-1} (235 km/mol) band corresponds to the hydrogen-bonded N-H stretch (a'), and the 3589 cm^{-1} (64 km/mol) band corresponds to the symmetric combination of the two free N-H stretches (a'). The IR intensity of both

vibrations is significantly enhanced with respect to ν_1 (2 km/mol) and ν_3 (6 km/mol) of free ammonia. The antisymmetric combination of the free NH stretches at 3653 cm^{-1} (a") is predicted to have no IR intensity. One may also note that the first overtone of the bending modes at 1650 cm^{-1} (a') and 1700 cm^{-1} (a") would be in the vicinity of NH stretches. For the bifurcated structure (**IIb**), three IR active vibrations (3510, 3617 and 3644 cm^{-1}) of comparable intensity (17, 11 and 7 km/mol) are obtained in the 3000-3700 cm^{-1} region. Only one doubly degenerate vibration (3632 cm^{-1}) is predicted to be IR active for the dipole-aligned geometry (**Ic**) with an intensity of 7 km/mol. The a_1 vibration at 3524 cm^{-1} is predicted to be IR inactive.

4.3.2 $I^-\cdot(NH_3)$

The computational results of $I^-\cdot(NH_3)$ are similar to those of $Br^-\cdot(NH_3)$. Of the three calculated geometries (Figure 2), the C_s structure with one hydrogen bond (**IIa**) is again found to be a minimum point. The bifurcated structure (**IIb**, C_s) is a first order TS corresponding to the interconversion of equivalent **IIa**'s through internal rotation. The dipole-aligned geometry (**IIc**, C_{3v}) is a second order TS. The electronic and relative energies of these geometries are shown in Table 5. From the minimum geometry (**IIa**), the binding energy of $I^-\cdot(NH_3)$ is calculated to be 6.5 kcal/mol, and is reduced to 5.8 kcal/mol by ZPVE correction. These predicted values are only in approximate agreement with experimental measurement (ΔH_{298} = 7.7 ± 0.1 kcal/mol)[19]. The deviation may be due to the frozen-core approximation employed for the complex and the neglect of BSSE, but one does not expect better agreement at this level of theory and basis set. The relative

energies of **IIb** and **IIc** with respect to **IIa** are 0.8 and 0.7 kcal/mol. ZPVE correction reduces these values to 0.5 and 0.3 kcal/mol, respectively.

The results of the geometry optimization are given in Table 3. For the minimum structure (**IIa**), the hydrogen bond is nearly linear (I-H-N = 157.6°) and the I-H distance is predicted to be 2.960 Å. In comparison with $Br^-(NH_3)$, the complexation with I^- leads to a smaller distortion to the ammonia moiety. The N-H bond with the shared proton is lengthened by 0.008 Å, and the non-hydrogen-bonded N-H bonds is lengthened by 0.002 Å. The hydrogen bonds are significantly longer in **IIb** and **IIc**, with respective I-H distances of 3.339 and 3.680 Å. The N-H bond containing the shared proton (1.017 Å) remains close to the free ammonia (1.014 Å) in both geometries. The hydrogen-bond angel (I-H-N) is 101.8° for **IIb** and 100.9° for **IIc**.

The vibrational frequencies of **IIa-c**, together with the symmetries and predicted infrared intensity (km/mol), are shown in Table 6Isomer **IIa** displays two IR active vibrations similar to the case of $Br^-\cdot(NH_3)$. The 3472 cm^{-1} (111 km/mol) band corresponds to the N-H stretch (a') hydrogen-bonded to I^-, and the 3597 cm^{-1} (73 km/mol) band corresponds to the symmetric combination of the two free N-H stretches (a'). The IR intensity of both vibrations is again significantly enhanced with respect to ν_1 and ν_3 of free ammonia. The antisymmetric free NH stretch at 3648 cm^{-1} (a") is predicted to be IR inactive. The first overtone of the bending vibrations at 1652 cm^{-1} (a') and 1690 cm^{-1} (a") would also be in the vicinity of the NH stretches. For the bifurcated structure (**IIb**), three IR active vibrations (3506, 3620 and 3640 cm^{-1}) of comparable intensity (12, 9 and 8 km/mol) are obtained in the region of interest, with intensities that are much weaker than those of **Ia**. For the dipole-aligned geometry (**IIc**), two vibrational

frequencies are obtained between 3000 to 3700 cm^{-1}. The doubly-degenerated (e) mode at 3632 cm^{-1} (6 km/mol) is weakly IR active, and the a_1 mode at 3519 cm^{-1} (1 km/mol) is almost IR inactive.

4.4 EXPERIMENTAL RESULTS AND DISCUSSION

The respective TOF mass spectra of $Br^-\cdot(NH_3)_n$ and $I^-\cdot(NH_3)_n$ clusters are shown in Figures 3 and 4. The infrared spectra of mass-selected $Br^-\cdot(NH_3)$ and $I^-\cdot(NH_3)_n$ (n = 1-3) ions were recorded in the 3050-3450 cm^{-1} region at a step size of 2.5 cm^{-1}. The only photodissociation channel observed in our experiments was the loss of one ammonia molecule.

4.4.1 $Br^-\cdot(NH_3)$

The vibrational predissociation spectrum of $Br^-\cdot(NH_3)$ is shown in Figure 5. The IR spectrum is dominated by an intense absorption band centered at 3182 cm^{-1}. The band appears as a doublet with peaks located at 3175 and 3185 cm^{-1}. A broad feature of weaker intensity is seen to center at 3280 cm^{-1}. Another sharper feature with similar intensity is also observed at 3347 cm^{-1}.

The observed spectrum is consistent with the structure **Ia** (C_s) in which the ammonia formed one near linear hydrogen bond with Br^-. Using a scaling factor of 0.94[29], the *ab initio* frequencies for the ionic hydrogen-bonded NH stretch and symmetric free NH stretch are predicted to be 3231 cm^{-1} (ν_2) and 3374 cm^{-1} (ν_1) respectively, with a relative intensity of about 1:4. This frequency pattern is in reasonably good agreement (within 2%) with the experimental spectrum. The larger discrepancy in the lower

frequency vibration is likely to due to the larger anharmonicity in the hydrogen-bonded mode. The broad band at around 3280 cm^{-1} can either be associated with the overtone of bending modes ($2\nu_3$ and $2\nu_8$) or the combination of ν_2 with low frequency modes (e.g. ν_6). The bifurcated structure (**Ib**) is predicted to have three IR absorptions of similar intensity (4:3:2) at 3300, 3400 and 3425 cm^{-1}, where the C_{3v} structure (**Ic**) is predicted to have only one degenerated IR active mode at 3414 cm^{-1}. Both of these predictions are not consistent with the experimental data. Similar structure has been assigned for $Cl^-\cdot(NH_3)$[22,23]. The ionic NH stretch in $Cl^-\cdot(NH_3)$ is 68 cm^{-1} red-shifted from that of $Br^-\cdot(NH_3)$.

The ionic NH stretch displays a steep low-energy edge and shading to the blue, suggesting a P branch bandhead and a contraction of the intermolecular bond upon excitation. The 10 cm^{-1} splitting of the doublet feature is quite unusual. Typical ionic hydrogen-bonded vibrational bands are broad, red-shifted bands with little or no structure. The broadness is generally attributed to unresolved combination bands involving low frequency modes. Currently the observed splitting is unassigned. Possible origins include a sequence hot band due to an initial excitation to a low frequency vibration, partially resolved rotational structure, H-atom exchange via hindered internal rotation of the NH_3 or inversion (umbrella motion) of the ammonia moiety. However, as suggested by a theoretical study on the related $H^-\cdot(NH_3)$ system [30], the splittings induced by hindered internal rotation or inversion of the NH_3 are likely to be less than 1 cm^{-1}. Therefore these tunnelings are not the probable causes for the observed splitting.

4.4.2 $I^-\cdot(NH_3)$

The vibrational spectrum of $I^-\cdot(NH_3)$ is shown in Figure 6. Five absorption features are observed in the 3100-3450 cm^{-1} region. An intense doublet-like band appears at 3217 and 3240 cm^{-1}, and a second doublet band is located at 3360 and 3385 cm^{-1}. Both of the doublets are blue-shaded. An intense singlet is observed at 3305 cm^{-1}.

Comparing the IR spectrum with those of the $Cl^-\cdot(NH_3)$ and $Br^-\cdot(NH_3)$, the additional absorption bands in $I^-\cdot(NH_3)$ are rather intriguing. The $Cl^-\cdot(NH_3)$ and $Br^-\cdot(NH_3)$ complexes possess similar features corresponding to a dominating ionic NH stretch and a weak free NH stretch. The $I^-\cdot(NH_3)$ complex, however, displays a doublet in the region of ionic-hydrogen-bonded NH stretch. The stronger component in this doublet is blue-shifted by 42 cm^{-1} from the ionic NH stretch of $Br^-\cdot(NH_3)$. The second doublet is in the region of the free NH stretch. The singlet is observed in the region that may correspond to the bending overtone of NH_3 moiety or the combination of the ionic NH stretch with a low frequency intermolecular mode.

The basic frequency patterns of the three geometries do not agree with the experimental observation. Of these three geometries, only the one-hydrogen-bond structure (**IIa**) is found to be a minimum point. However, the energy differences among the geometries are predicted to be within 1 kcal/mol, and structures **IIb** and **IIc** may not necessarily be high-order stationary points when computed at higher level of theory. Using a scaling factor of 0.94 for *ab initio* frequencies, the following comparisons with the calculated geometries are possible:

1) If the $I^-\cdot(NH_3)$ complex posses the predicted minimum energy structure with one nearly linear hydrogen bond (**IIa**), the predicted IR frequencies for the hydrogen-bonded

NH and symmetric free NH stretches will be 3264 and 3381 cm^{-1} respectively with an intensity ratio 3:2. One may then assign the 3217 cm^{-1} peak to the ionic NH stretch and the 3360 cm^{-1} peak to the free NH stretch. The higher-frequency component of the doublets (+23 and +25 cm^{-1}) may due to a sequence hot band involving initial states excited to one of the low-frequency intermolecular vibrations (e.g. $\nu_{im} \rightarrow \nu_2 + \nu_{im}$, where ν_{im} = intermolecular mode). The complexes probed in our experiment may possess substantial vibrational energy as the cluster temperature is limited by the evaporative cooling of the ammonia monomer. While the intermolecular vibrations may be quite anharmonic, differences between ground and excited state frequencies will be small and may lead to closely spaced sequence bands. Such a hot-band sequence has been assigned in a similar experiment on $I^-\cdot(C_2H_2)$[31]. The singlet feature at 3305 cm^{-1} may be assigned to the combination of ionic NH stretch and a low frequency mode (ν_5 or ν_6.). Alternatively, it may be assigned to an overtone of one of the bending vibrations (ν_3 or ν_8) of the ammonia moiety. The high intensity indicates that the bend overtone would have to be strongly coupled to the ionic stretch, i.e. the local modes would be essentially degenerate. Such a resonance behavior has been observed in $Br^-\cdot(H_2O)$, but is substantially weaker in $Cl^-\cdot(H_2O)$ and $I^-\cdot(H_2O)$.[5]. If the bend overtone and the ionic stretch are strongly coupled, the peaks at 3217 and 3305 cm^{-1} are better described as two components of the combined mode. One may then expect a sequence band to appear together with 3305 cm^{-1}; however, such a feature was not observed in our spectrum. Alternatively the 3240 cm^{-1} could be a Fermi-resonance with the other bend overtone ($2\nu_3$), but that would be inconsistent with the sequence band assignment of the free NH stretch.

2) If the structure with two hydrogen bonds (**IIb**) is a minimum geometry instead, the observed spectrum may result from the coexistence of isomers **IIa** and **IIb**. The calculated IR absorptions for **IIb** are at 3296, 3403 and 3422 cm^{-1} with intensity ratio 3:2:2. One may assign the 3217 and 3385 cm^{-1} peaks to the ionic stretch and symmetric stretch of **IIa**. The peaks at 3240, 3305 and 3360 cm^{-1}, which are of similar intensity, may then correspond to the two ionic NH stretches and the free NH stretch of geometry **IIb** respectively. One discrepancy of this assignment, however, is that the predicted ionic NH stretches of **IIb** are red-shifted from free NH stretch by 126 and 19 cm^{-1}. The observed frequency pattern is of 120 and 55 cm^{-1} instead. Furthermore, *ab initio* calculations predict that the ionic NH stretch of **IIb** will only be one tenth as intense as the ionic NH stretch of **IIa**. The population of isomer **IIb** would then have to be much greater than that of isomer **IIa** to account for the intensities appearing in the spectrum

4.4.3 $I^-\cdot(NH_3)_n$ for n = 2, 3

Infrared vibrational spectra are also observed for $I^-\cdot(NH_3)_2$ and $I^-\cdot(NH_3)_3$ (Figure 7 and 8). The absorption bands are broader than that of n = 1, suggesting the inhomogenous broadening from different isomers possible for larger clusters. For n = 2, a broad band centered at around 3218 cm^{-1} is assigned to the ionic NH stretches. The band at 3365 cm^{-1} is assigned to the free NH stretch. The 3300 cm^{-1} band may be assigned to either bending overtone or combination band of ionic NH stretch with low-frequency modes. No fine structures are resolved for these absorptions. The corresponding bands in n = 3 are located at 3228, 3318 and 3370 cm^{-1}.

Interestingly, the ionic NH stretch is blue-shifted by 10 cm^{-1} from n = 2 to n = 3, but remains unchanged from n = 1 to n = 2. As the cluster increases, one may expect a typical weakening of the hydrogen bond between ligands and the ionic center. The reduced bond strength will then lead to a frequency blue-shift of the ionic hydrogen bond. This behavior is observed only at n =3, but not in n =2. The frequency-shift behavior suggests a possible enhancement of hydrogen-bonding due to the additional ammonia molecule at n = 2. A possible mechanism may involves a cooperative effect in which the binding of ammonia to the polarizable I^- ion induces a dipole that favors and is enhanced by the binding of a second ammonia to the same side of the ion. Such a mechanism has been suggested for $Sr^+(H_2O)_n$[32] and $Cl^-(H_2O)_n$ clusters [2].

4.5 SUMMARY

In this chapter we have reported the infrared predissociation spectroscopy of $Br^-\cdot(NH_3)$ and $I^-\cdot(NH_3)_n$ (n = 1-3) clusters in the region of 3050-3450 cm^{-1}. We have also performed *ab initio* calculations on three possible geometries for $Br^-\cdot(NH_3)$ and $I^-\cdot(NH_3)$ to aid in the assignment of the IR spectra.

For the $Br^-\cdot(NH_3)$ complex, the observed spectrum is consistent to the structure (**Ia**) in which there is one nearly linear hydrogen bond between the Br^- and the NH_3 moiety. A dominating ionic NH stretch appears at 3175 cm^{-1}, and the weaker free NH stretch appears at 3348 cm^{-1}. An unassigned splitting (~10 cm^{-1}) is also observed at the ionic NH stretch. Such an assignment is similar to that for $Cl^-\cdot(NH_3)$.

For the $I^-\cdot(NH_3)$ complex, five distinct IR absorption bands are observed in the spectrum. The spectrum is not consistent with basic frequency patterns of the three

geometries considered in the *ab initio* calculations. The geometry with single hydrogen bond (**IIa**) is possible if one invokes the appearance of sequence band at the ionic and free NH stretches, and a near degeneration of the bend overtone and the ionic stretch. The spectrum may also be consistent with the coexistence of the isomers with one (**IIa**) and two hydrogen bonds (**IIb**) in the $I^-\cdot(NH_3)$ complex.

Finally, substantial inhomogenous broadening are displayed in the vibrational spectra for $I^-\cdot(NH_3)_n$ (n =2-3), suggesting the possibility of multiple isomers of in larger clusters.

4.6 REFERENCES

1. M. S. Johnson, K. T. Kuwata, C.-K. Wong, and M. Okumura, *Chem. Phys. Lett.*, **260,** 551 (1996).

2. J.-H. Choi, K. T. Kuwata, Y.-B. Cao, and M. Okumura, *J. Phys. Chem. A,* **102,** 503 (1998).

3. C. G. Bailey, J. Kim, C. E. H. Dessent, and M. A. Johnson, *Chem. Phys. Lett.*, **269,** 122 (1997).

4. P. Ayotte, C. G. Bailey, G. H. Weddle, and M. A. Johnson, *J. Phys. Chem. A,* **102,** 3067 (1998).

5. P. Ayotte, G. H. Weddle, J. Kim, and M. A. Johnson, *J. Am. Chem. Soc.*, **120,** 12361 (1998).

6. P. Ayotte, S. B. Nielsen, G. H. Weddle, and M. A. Johnson, *J. Phys. Chem. A,* **103,** 10665 (1999).

7. P. Ayotte, G. H. Weddle, J. Kim, J. Kelley, and M. A. Johnson, *J. Phys. Chem. A,* **103,** 443 (1999).

8. P. Ayotte, J. A. Kelley, S. B. Nielsen, and M. A. Johnson, *Chem. Phys. Lett.*, **316,** 455 (2000).

9. S. J. Vaughn, E. V. Akhmatskaya, M. A. Vincent, A. J. Masters, and I. H. Hilier, *J. Chem. Phys.*, **110,** 4338 (1999).

10. H. E. Dorsett, R. O. Watts, and S. S. Xantheas, *J. Phys. Chem. A,* **103,** 3351 (1999).

11. O. M. Cabarcos, C. J. Weinheimer, J. M. Lisy, and S. S. Xantheas, *J. Chem. Phys.*, **110,** 5 (1999).

12. P. Weis, P. R. Kemper, and M. T. Bowers, *J. Am. Chem. Soc.*, **121,** 3531 (1999).

13. S. S. Xantheas and J. Thom H. Dunning, *J. Phys. Chem.*, **98,** 13489 (1994).

14. S. S. Xantheas, *J. Phys. Chem.*, **100,** 9703 (1996).

15. S. S. Xantheas and L. X. Dang, *J. Phys. Chem.*, **100,** 3989 (1996).

16. K. Satoh and S. Iwata, *Chem. Phys. Lett.*, **312,** 522 (1999).

17. R. G. Keesee and J. A. W. Castleman, *J. Phys. Chem. Ref. Data,* **15,** 1011 (1987).

18. J. W. Larson and T. B. McMahon, *J. Am. Chem. Soc.*, **106,** 517 (1984).

19. D. H. Evans, R. G. Keesee, and J. A. W. Castleman, *J. Chem. Phys.*, **86,** 2927 (1987).

20. U. Kaldor, *Z. Phys. D,* **31,** 279 (1994).

21. G. Markovich, O. Cheshnovsky, and U. Kaldor, *J. Chem. Phys.*, **99,** 6201 (1993).

22. P. S. Weiser, D. A. Wild, P. P. Wolynee, and E. J. Bieske, *J. Phys. Chem. A,* **104,** 2562 (2000).

23. K. T. Kuwata, *Ph. D. Thesis*, California Institute of Technology, 1998.

24. J.-H. Choi, *Ph. D. Thesis*, California Institute of Technology, 1995.

25. M. S. Johnson, *Ph. D. Thesis*, California Institute of Technology, 1995.

26. E. J. Bieseke, A. M. Soliva, and J. P. Maier, *J. Chem. Phys.*, **94,** 4749 (1991).

27. M. J. Frisch, G. W. Trucks, H. B. Schlegel, P. M. W. Gill, B. J. Johnson, M. A. Robb, J. R. Cheeseman, T. A. Keith, G. A. Petersson, J. A. Montgomery, K. Raghavachari, M. A. Al-Laham, V. G. Zarkrewski, J. V. Ortiz, J. B. Foresman, J. Cioslowski, B. B. Stefanov, A. Nanayakkara, M. Challacombe, C. Y. Peng, P. Y. Ayala, W. Chen, M. W. Wong, J. L. Andres, E. S. Replogle, R. Gomperts, R. L. Martin, D. J. Fox, J. S. Binkley, D. J. Defrees, J. Baker, J. J. P. Stewart, M. Head-Gordon, C. Gonzalez, and J. A. Pople, , Revision D4 ed. (Gaussian Inc., Pittsburgh, PA, 1995).

28. G. Herzberg, *Molecular Spectra and Molecular Strcuture, Volume II and III* (Krieger Publishing, Malabar, Floride, 1991).

29. A. P. Scott and L. Radom, *J. Phys. Chem.*, **100,** 16502 (1996).

30. G. C. M. v. d. Sanden, E.-A. Reinsch, A. v. d. Avoird, P. E. S. Wormer, and P. Rosums, *J. Chem. Phys.*, **103,** 4012 (1995).

31. P. S. Weiser, D. A. Wild, and E. J. Bieske, *Chem. Phys. Lett.*, **299,** 303 (1999).

32. J. C. W. Baushlicher, M. Sodupe, and H. Partridge, *J. Chem. Phys.*, **96,** 4453 (1992).

Table 1 Calculated Properties for NH_3 (C_{3v}) at MP2(Full) and MP2(FC) levels of theory with 6-311++G** basis sets.

NH_3 [a]	Full Correlation	Frozen Core Correlation	Experimental [b]
r(N-H) (Å)	1.013	1.014	1.012
θ (H-N-H) (deg.)	111.5	111.6	106.7
ω_1 [c] (cm^{-1}, a_1) [d]	3536 (2)	3530 (2)	3336.2
ω_2 [c] (cm^{-1}, a_1) [d]	1066 (209)	1069 (207)	932.5
ω_3 [c] (cm^{-1}, e) [d]	3689 (6)	3682 (6)	3443.6
ω_4 [c] (cm^{-1}, e) [d]	1666 (25)	1665 (25)	1626.1
A, B (cm^{-1})	10.006	9.986	9.944
C (cm^{-1})	6.279	6.277	6.196
μ (Debye)	1.777	1.782	1.48

[a] Properties included are internal geometries, vibrational frequencies, rotational constants and dipole moment.

[b] Reference 28.

[c] Infrared intensities are given in parentheses, unit in km/mol.

[d] Mode symmetry.

Table 2 Calculated energies for Br^-, NH_3, and the three geometries of $Br^-\cdot(NH_3)$ at MP2(Full)/6-311++G** level.

Electronic Energy	E_o (a.u.)	E_e (a. u.)[b]
NH_3	-56.434680	-56.399794
Br^-	-2572.963065	-2629.407977
C_s (minimum)	-2629.410174	-2629.374015
C_s (1° T.S.)	-2629.408329	-2629.372642
C_{3v} (2° T.S.)	-2629.407977	-2629.372743
Relative Energy	**ΔE_o (kcal/mol)**	**ΔE_e (kcal/mol)**
C_s (minimum)	0.0	0.0
C_s (1° T.S.)	1.2	0.9
C_{3v} (2° T.S.)	1.4	0.8
$Br^- + NH_3$	7.8	7.0 (expt'l = 7.7 ± 0.1)[a]

[a] ΔH_{298}, Reference 19.

[b] $E_e = E_o$ + Zero-point vibrational energy

Table 3 Calculated geometries for $Br^-\cdot(NH_3)$ and $I^-\cdot(NH_3)$ at MP2(FU)/6-311++G** and MP2(FC)/6-311++G** levels, respectively.

$X^-\cdot(NH_3)$[a]	X = Br[b]	X = I[c]
C_s, 1 H-Bond	**Ia**	**IIa**
r (X-H_2)	2.617	2.960
r (N_1-H_2)	1.024	1.022
r (N_1-H_3)	1.015	1.016
θ (X-H_2-N_1)	163.0	157.6
θ (H_2-N_1-H_3)	104.6	104.5
θ (H_3-N_1-H_4)	105.3	105.3
C_s, 2 H-Bonds	**Ib**	**IIb**
r (X-H_2)	3.056	3.339
r (X-N_1)	3.602	3.886
r (N_1-H_2)	1.017	1.017
r (N_1-H_4)	1.016	1.016
θ (X-H_2-N_1)	114.7	115.4
θ (H_2-N_1-H_3)	100.9	101.8
θ (H_4-N_1-H_2)	105.4	105.4
C_{3v}, 3 H-Bonds	**Ic**	**IIc**
r (X-H_2)	3.395	3.680
r (X-N_1)	3.712	3.999
r (N_1-H_2)	1.017	1.017
θ (X-H_2-N_1)	100.2	100.9
θ (H_2-N_1-H_3)	102.4	103.0

[a] Bond lengths in Å, bond angles in degree.

[b] Atoms are labeled in Figure 1.

[c] Atoms are labeled in Figure 2.

Table 4 Calculated vibrational frequencies and infrared intensities of $Br^-\cdot(NH_3)$ at MP2(FU)/6-311++G** level.

Frequency [a] (cm^{-1})	**Ia** (C_s, Minimum)	**Ib** (C_s, 1° T.S.)	**Ic** (C_{2v}, 2° T.S.)
ω_1	3589 (64, a')	3644 (7, a')	3524 (0, a_1)
ω_2	3438 (235, a')	3510 (17, a')	1259 (242, a_1)
ω_3	1650 (18, a')	1662 (72, a')	82 (4,a_1)
ω_4	1221 (165, a')	1240 (180, a')	3632 (7, e)
ω_5	287 (65, a')	239 (89, a')	1668 (12, e)
ω_6	114 (6, a')	104 (3, a')	192i (97, e) [b]
ω_7	3653 (0, a")	3617 (11, a")	
ω_8	1700 (10, a")	1649 (16, a")	
ω_9	220 (31, a")	187i (54, a") [b]	

[a] Infrared intensity (km/mol) and mode symmetry are given in parentheses.

[b] Imaginary frequency.

Table 5 Calculated energies for I^-, NH_3, and the three geometries of $I^-\cdot(NH_3)$ at MP2(FC)/6-311++G** level.

Electronic Energy	E_o (a.u.)	E_e (a. u.)[b]
NH_3	-56.415524	-56.380683
I^-	-6917.109796	-6917.109796
C_s (minimum)	-6973.535717	-6973.499778
C_s (1° T.S.)	-6973.534513	-6973.498950
C_{3v} (2° T.S.)	-6973.534543	-6973.499354

Relative Energy	ΔE_o (kcal/mol)	ΔE_e (kcal/mol)
C_s (minimum)	0.0	0.0
C_s (1° T.S.)	0.8	0.5
C_{3v} (2° T.S.)	0.7	0.3
$I^- + NH_3$	6.5	5.8 (expt'l = 7.4 ± 0.3)[a]

[a] ΔH_{298}, Reference 19.

[b] $E_e = E_o$ + Zero-point vibrational energy

Table 6 Calculated vibrational frequencies and infrared intensities of $I^-\cdot(NH_3)$ at MP2(FC)/6-311++G** level.

Frequency [a] (cm^{-1})	**IIa** (C_s, Minimum)	**IIb** (C_s, 1° T.S.)	**IIc** (C_{2v}, 2° T.S.)
ω_1	3597 (73, a')	3640 (8, a')	3519 (1, a_1)
ω_2	3472 (111, a')	3506 (12, a')	1251 (272, a_1)
ω_3	1652 (22, a')	1662 (73, a')	73 (2,a_1)
ω_4	1211 (184, a')	1244 (184, a')	3632 (6, e)
ω_5	233 (64, a')	217 (87, a')	1670 (11, e)
ω_6	95 (3, a')	88 (1, a')	151i (95, e) [b]
ω_7	3648 (0, a")	3620 (9, a")	
ω_8	1690 (8, a")	1651 (17, a")	
ω_9	175 (38, a")	144i (52, a") [b]	

[a] Infrared intensity (km/mol) and mode symmetry are given in parentheses.

[b] Imaginary frequency.

4.6 FIGURE CAPTIONS

Figure 1 The optimized geometries for the $Br^-\cdot(NH_3)$ complex.

Figure 2 The optimized geometries for the $Br^-\cdot(NH_3)$ complex.

Figure 3 TOF mass spectrum for the $Br^-\cdot(NH_3)_n$ clusters.

Figure 4 TOF mass spectrum for the $I^-\cdot(NH_3)_n$ clusters.

Figure 5 Infrared predissociation spectrum of $Br^-\cdot(NH_3)$.

Figure 6 Infrared predissociation spectrum of $I^-\cdot(NH_3)$.

Figure 7 Infrared predissociation spectrum of $I^-\cdot(NH_3)_2$.

Figure 8 Infrared predissociation spectrum of $I^-\cdot(NH_3)_3$.

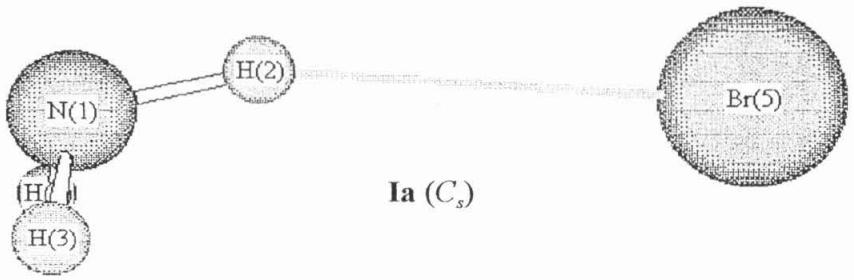

Ia (C_s)

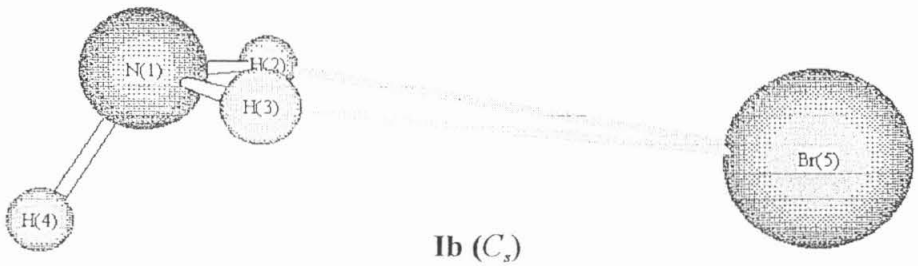

Ib (C_s)

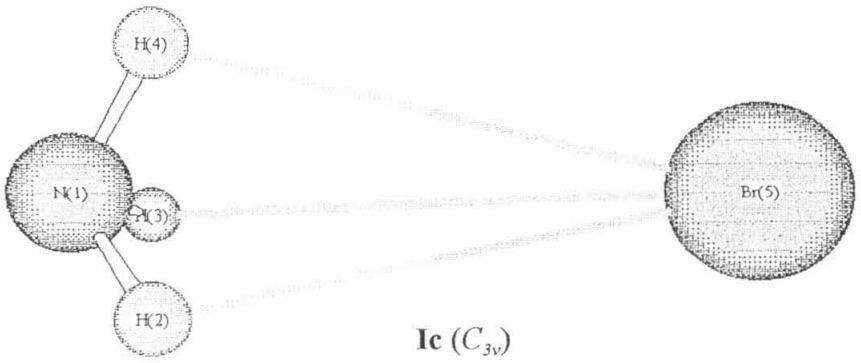

Ic (C_{3v})

Figure 1

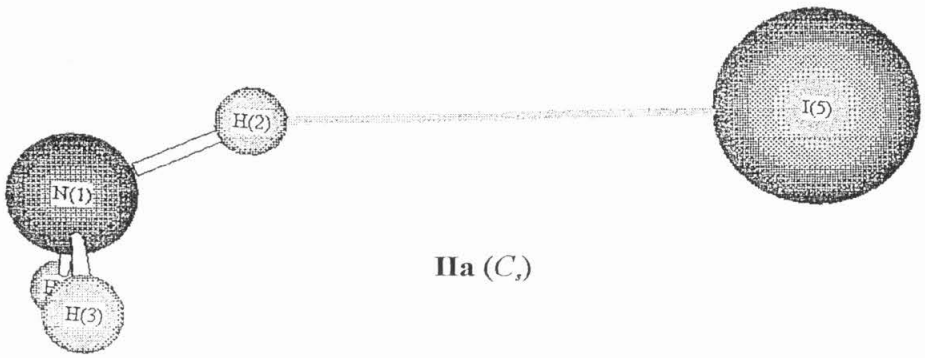

IIa (C_s)

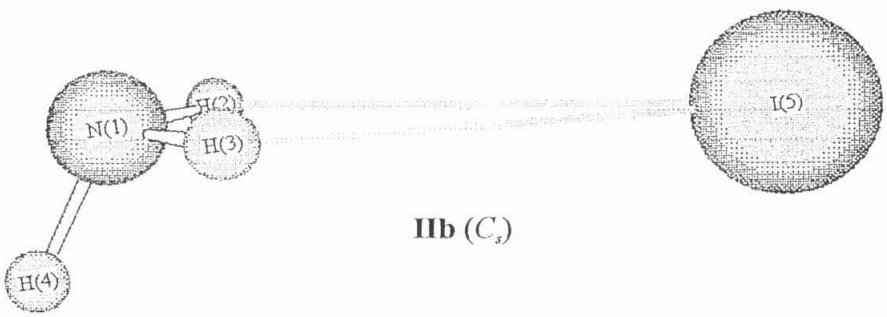

IIb (C_s)

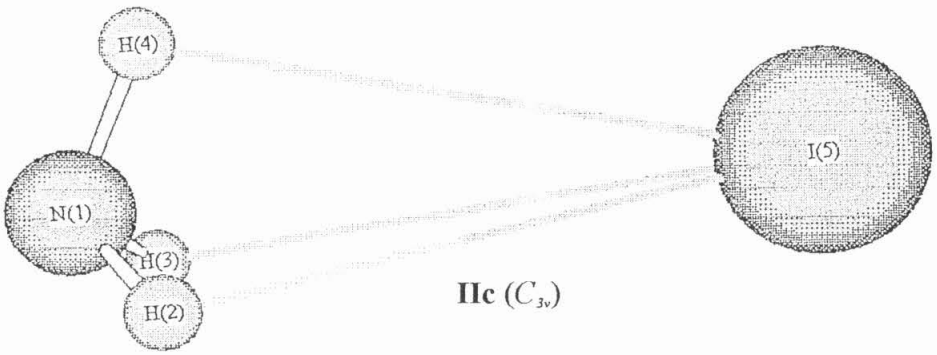

IIc (C_{3v})

Figure 2

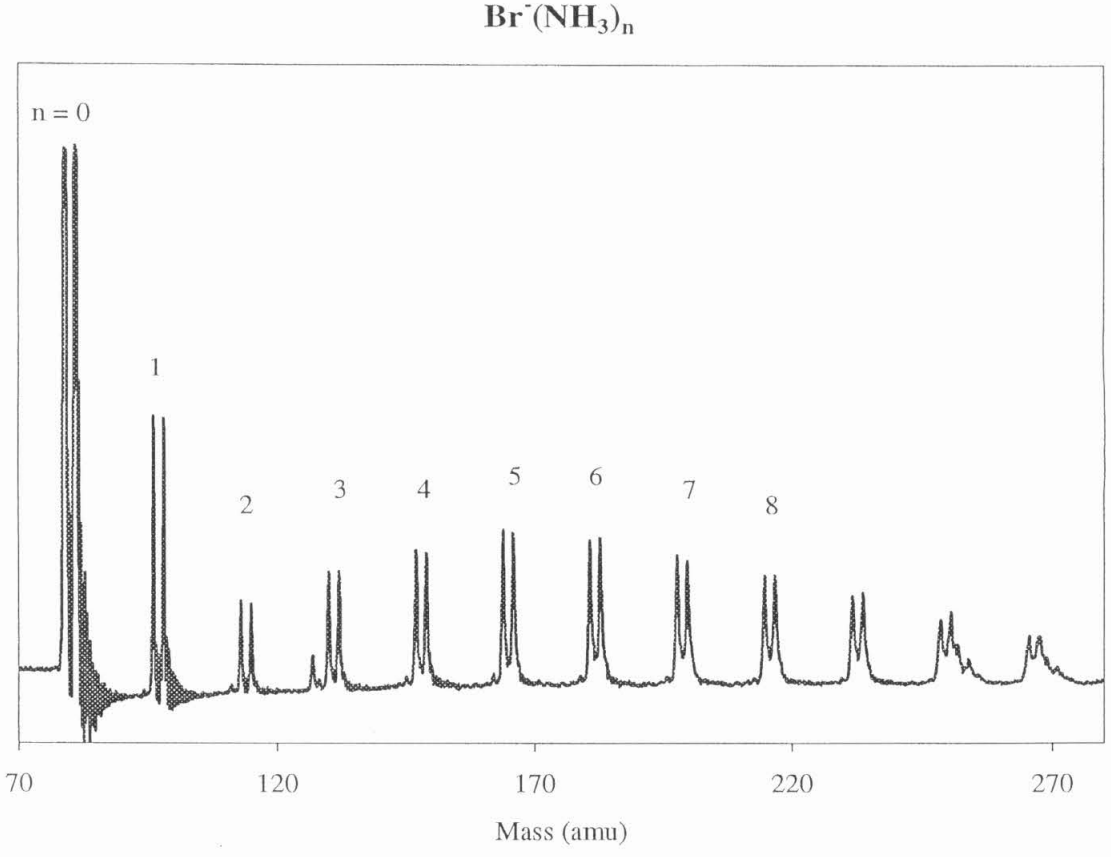

Figure 3

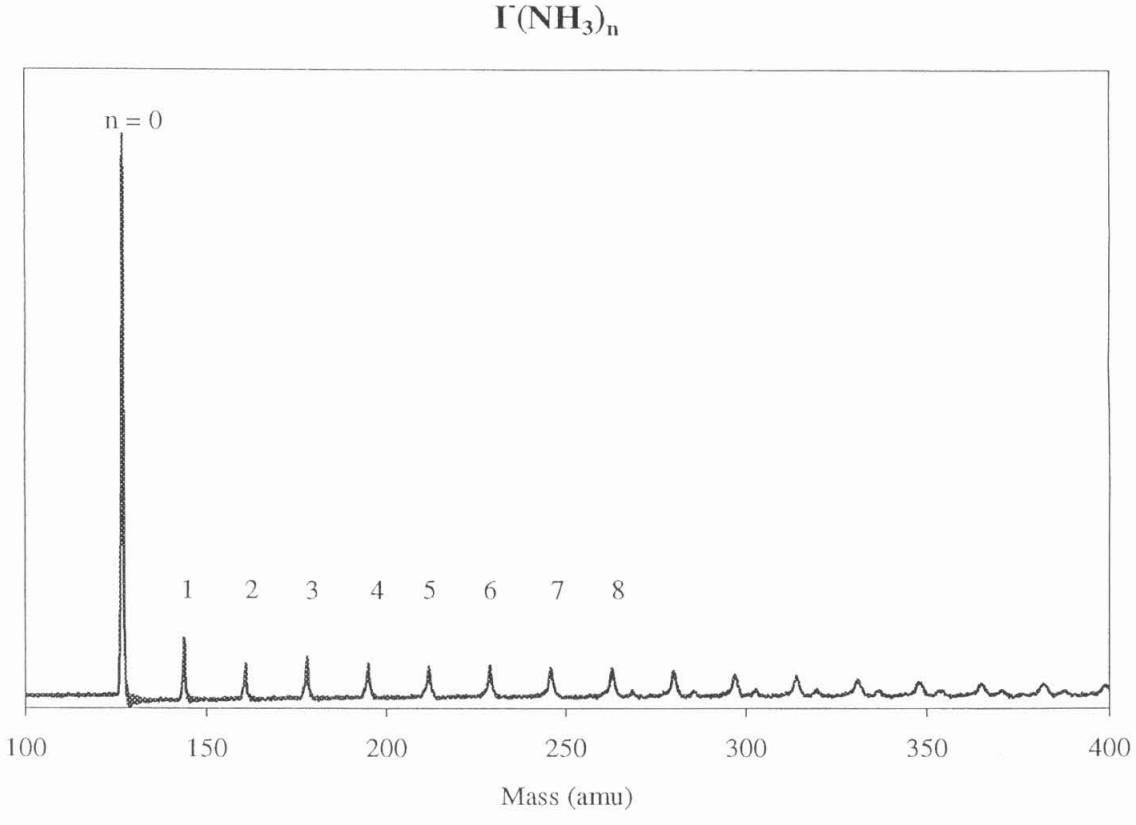

Figure 4

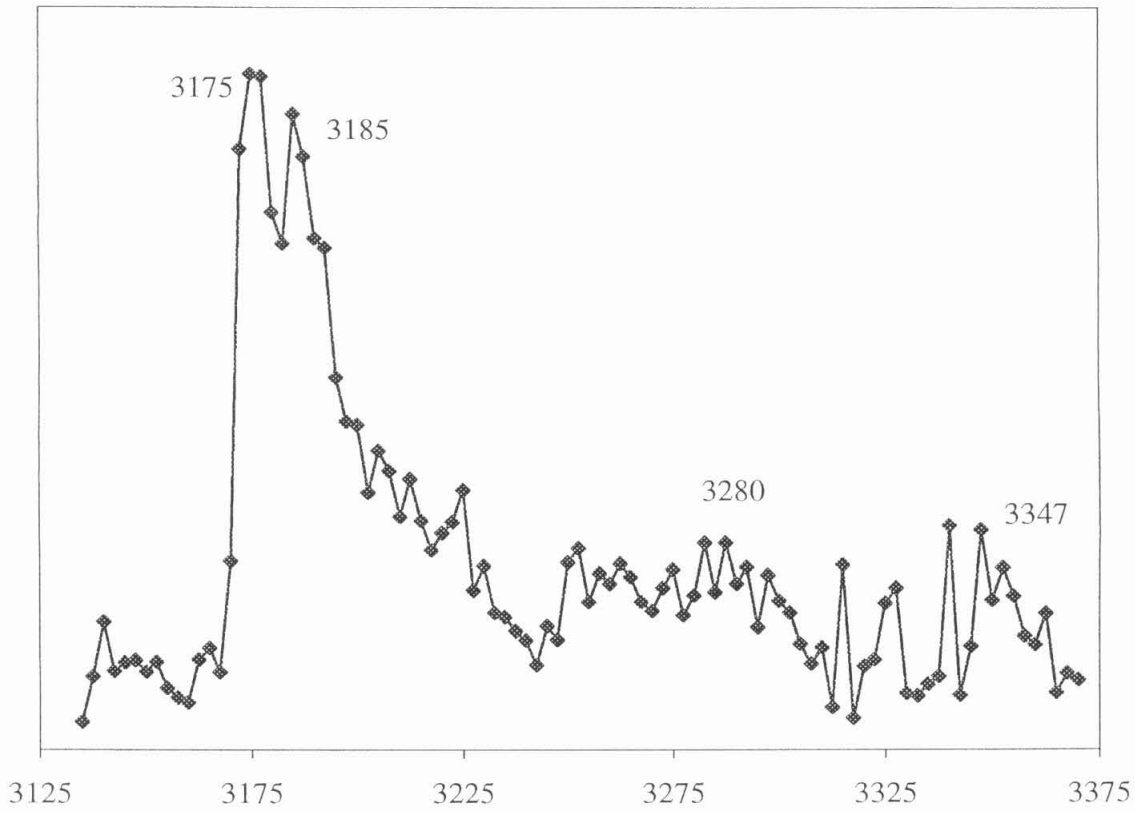

Figure 5

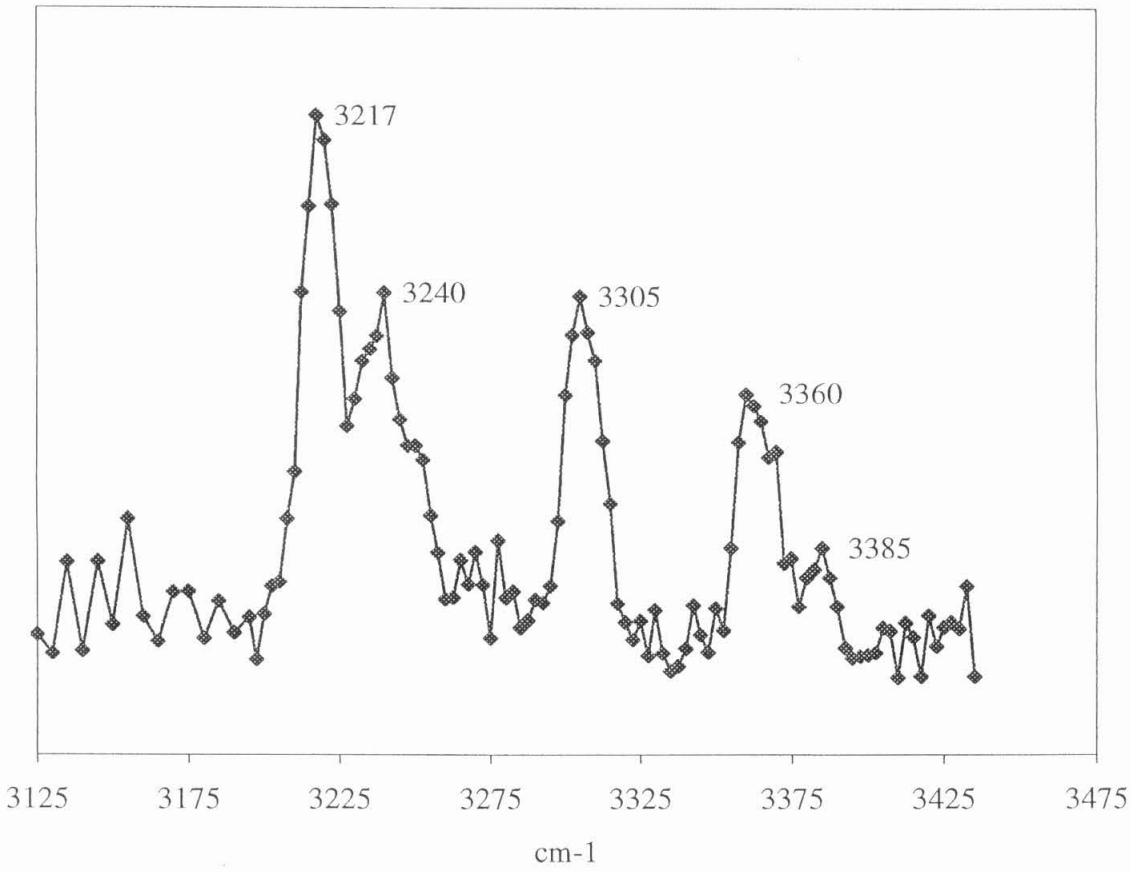
3217
3240
3305
3360
3385
3125
3175
3225
3275
3325
3375
3425
3475
cm-1

Figure 6

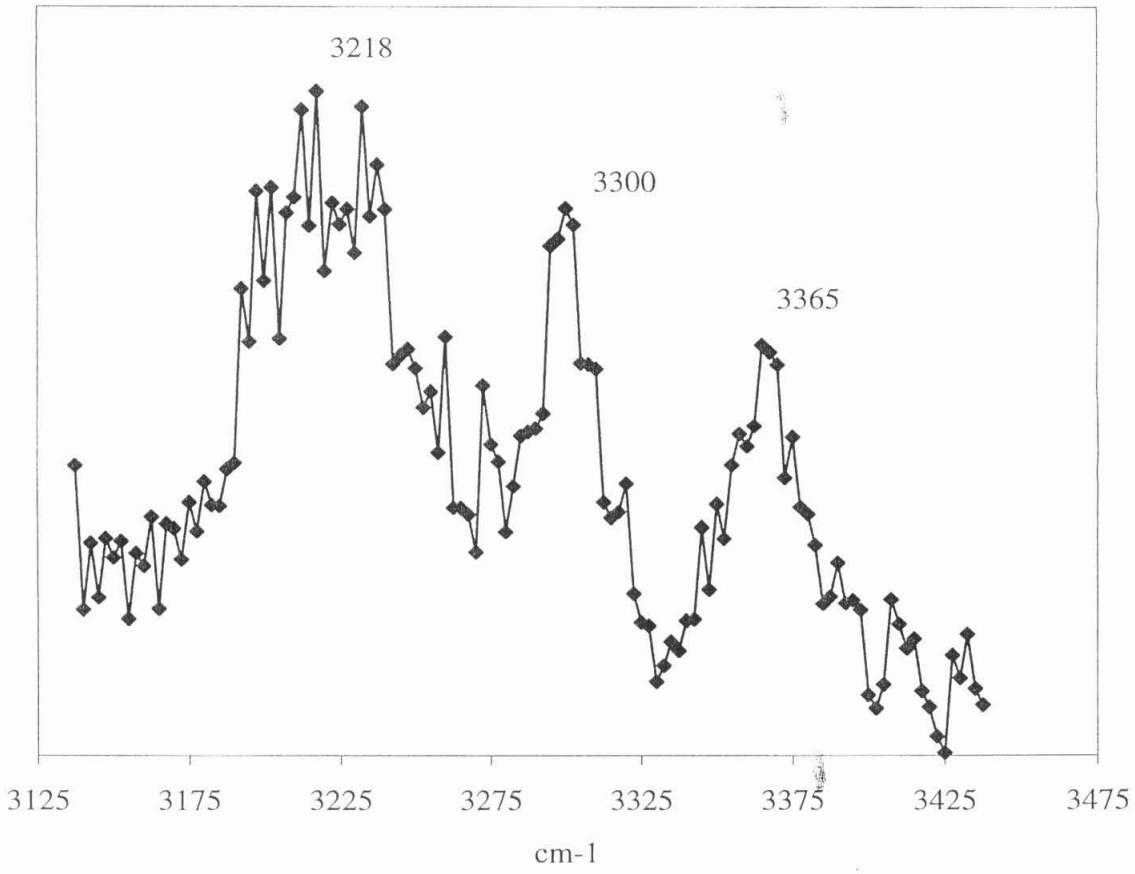

Figure 7

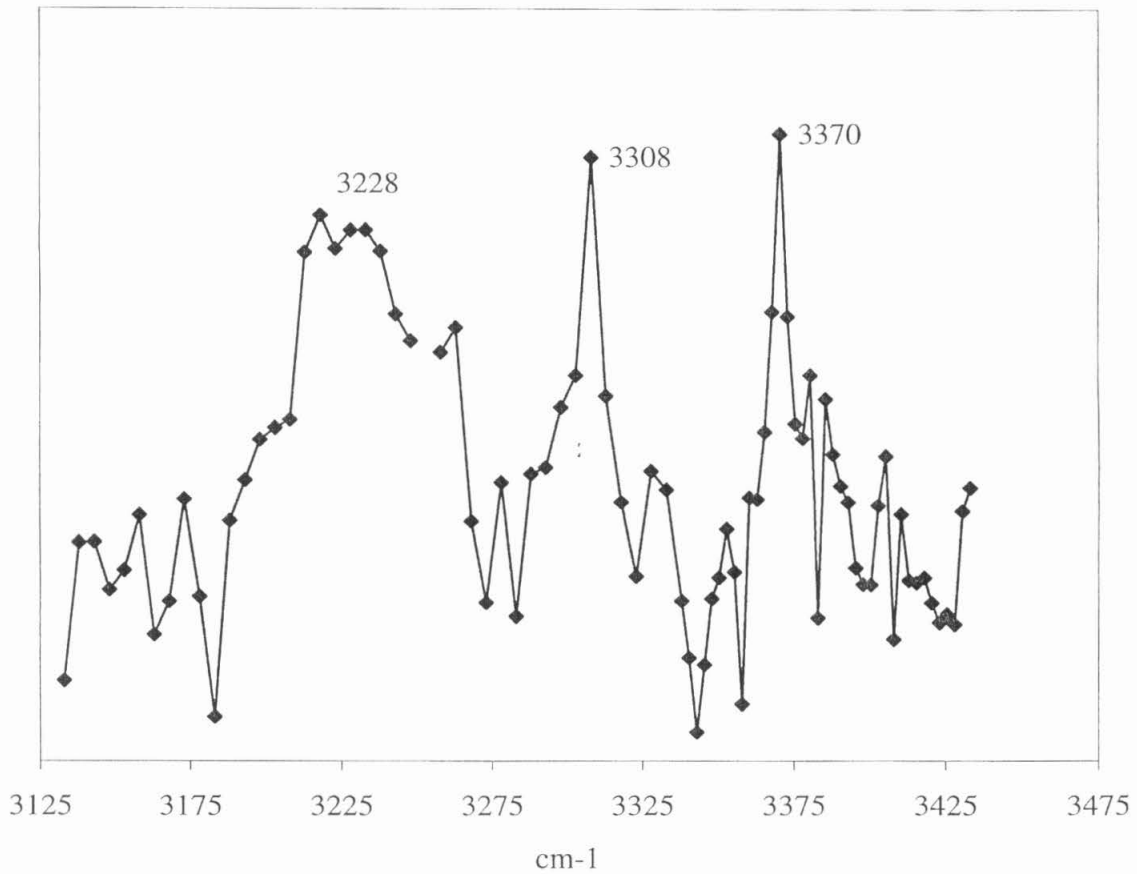

Figure 8

CHAPTER 5

Multiphoton Ionization Studies of the $4d\ ^2\Sigma^+_{1/2} \leftarrow 3p\ ^2\Pi_{1/2}$ Transition in AlAr Complex

5.1 INTRODUCTION

Diatomic metal atom-rare gas (M·RG) complexes have attracted extensive interest in recent years[1,2]. These molecules have provided considerable information about the nonbonding interactions between metal and rare gas atoms both in the electronic ground and excited states. From a fundamental point of view, the simplicity of such systems allows detailed investigations of the van der Waals interaction. Variations of parameters such as metal atom identity, electronic state energy and symmetry, and rare-gas polarizability can be readily achieved. The determination of accurate potential energy curves for M·RG interactions in specific electronic states is important in the understanding of dynamical processes such as scattering and energy transfer. The potential energy curves may also be employed as pair potentials for modeling of larger systems.

The studies of M·RG span across numerous metal atoms such as those in Groups 1 (Li, Na, K), 2 (Be, Mg, Ca), 12 (Zn, Cd, Hg), and 13 (B, Al, Ga, In and Tl)[1]. Among the complexes of Group 13 metals, Al has received much attention[3-11]. In particular there has been considerable interest in the AlAr molecule. Using resonance enhanced multiphoton ionization (REMPI), Gardner and Lester[3] reported the first observation of Al·Ar complex. They measured the $B\ ^2\Sigma_{1/2} \leftarrow X_1\ ^2\Pi_{1/2}$ electronic transition, which correlates with Al atomic $4s \leftarrow 3p$ transition, and determined the lower limits for binding energies (D_0) in $X_1\ ^2\Pi_{1/2}$ and $B\ ^2\Sigma_{1/2}$ states to be 133 and 373 cm^{-1}, respectively. Callender *et al.*[4] extended the work to include heavier rare gases by using laser induced fluorescence (LIF) excitation and dispersed emission. They characterized the vibrational spacings in the ground electronic states of AlAr, AlKr and AlXe. For AlAr complex, they

reported a D_0 value of 136 ± 65 cm^{-1} for the $X\ ^2\Pi_{1/2}$ state, and 369 ± 65 cm^{-1} for the $B\ ^2\Sigma_{1/2}$ state. Furthermore, they determined the spin-orbit splitting between the $X_1\ ^2\Pi_{1/2}$ and $X_2\ ^2\Pi_{3/2}$ states to be 79.8 cm^{-1}. McQuaid *et al.*[5] extended the work to rotationally resolved a number bands in AlAr $B\ ^2\Sigma_{1/2} \leftarrow X_1\ ^2\Pi_{1/2}$ transition. They reported the D_0 values for $X_1\ ^2\Pi_{1/2}$ and $B\ ^2\Sigma_{1/2}$ states as 165 $^{+40}/_{-10}$ cm^{-1} and 399 $^{+35}/_{-8}$ cm^{-1} respectively. The authors also employed the derived vibrational and rotational constants to construct the upper and lower potential energy curves. In 1992, Morse and coworkers[6] used REMPI technique to study several excited states of AlAr and AlKr associated with Al atomic levels from *3d* level up to the ionization limit. By using the D_e value of electronic states arising from the Al(3d) + Ar($^1S_0$) asymptote, they reported a 122.4 ± 4 cm^{-1} value for the D_0 of $X_1\ ^2\Pi_{1/2}$ state. They also determined a spin-orbit spitting of 80.9 ± 4 cm^{-1} between the $X_1\ ^2\Pi_{1/2}$ and $X_2\ ^2\Pi_{3/2}$ states. This lower value of D_0 for $X_1\ ^2\Pi_{1/2}$ state was later supported by the theoretical work of Partridge *et al.*[11] The authors employed a RHF/CCSD(T)/AANO level theory and calculated the D_0 value to be 114.0 cm^{-1}. There was an apparent discrepancy between the $X_1\ ^2\Pi_{1/2}$ D_0 values measured for the X state by McQuaid *et al.* from the $B \leftarrow X$ transition and by from the $C \leftarrow X$ transition. This discrepancy can be resolved by assuming a barrier on the curve potential energy at large internuclear distance for the $B\ ^2\Sigma_{1/2}$ state [6]. From the values of D_0 from McQuaid *et al.*[5] and Morse and coworkers[6], the barrier height can be estimated to be about 40 cm^{-1}.

Recently, Spotts[12] has led an effort in or group to re-examine the electronic spectroscopy of AlAr complex in the vicinity of Al(*3d*/*4p*) manifolds. We focused on the perturbations between Al 3d and 4p electronic states induced by complexation with Ar.

For atomic Al, the $3d \leftarrow 3p$ transitions are strictly one-photon allowed but two-photon forbidden. The reversed situation applies to the $4p \leftarrow 3p$ transitions. In view of this potential selectivity, we performed both one-photon and two-photon measurements for the electronic transitions in AlAr complex. The basic assumption of the experiments was that the one-photon excitation will primarily probe the $3d$ character of the states, while the two-photon excitation will probe the $4p$ characters.

We utilized the one- and two-photon REMPI techniques and reported the previously unobserved two-photon transitions from the ground Al(3p) state to Al($4p$) excited states. We demonstrated the occurrence strong state mixing between the Al 3d/4p manifolds by one- and two-photon REMPI techniques. We determined the Al($3d$)Ar dissociation limit at 137.7 cm^{-1} and proposed a new assignment for the $3d$ $^2\Pi$ and $^2\Sigma$ states in AlAr, and the necessity of changing the assignment suggested by Morse and coworkers[6].

In this chapter, we will report the Al $^2\Pi(4p)$ / $^2\Sigma(3d) \leftarrow {}^2\Pi(3p)$ transitions in the AlAr complex. Specifically we will demonstrate the significant perturbation between the $^2\Sigma_{1/2}(3d)$ and $^2\Pi_{1/2}(4p)$ states above the Al(3d)·Ar dissociation limit. The dissociative behavior of the $^2\Sigma(3d)$ state will also be discussed. The experimental results will be compared with the *ab initio* potential energy curves computed by Jeff A. Sheehy and Jerry A. Boatz at Phillips Laboratory, Edwards Air Force Base.[13]

5.2 EXPERIMENTAL

Details of the experimental arrangement have been discussed elsewhere.[12] Only a brief account will be given here to provide the details specific for this experiment.

Figure 1 shows the schematic diagram for the REMPI apparatus. The AlAr complex was generated by standard laser ablation techniques. Pure argon gas (99.99%, Matheson) at a stagnation pressure of 7-9 atm was expanded into a vacuum chamber (10^{-7} Torr with no gas load) through a piezoelectric pulsed valve (nozzle dia. = 1.5 mm) at a repetition rate of 19 Hz (pulse width = ~250 μs). The third harmonic output (355 nm) of a Nd-YAG laser (Continuum Surelite 1) was focused onto an aluminum target rod (1/4" dia.) positioned directly adjacent at the throat of the expansion to generate the Al atoms. The AlAr complex and larger clusters were then produced by the cooling in the supersonic expansion. About 5 cm downstream the gas jet was skimmed by a 3mm-orfice *skimmer* (Beam Dynamics) and the resulting beam passed into the second differential pumping chamber.

The second chamber consisted of the laser-ionization region, a time-of-flight (TOF) mass spectrometer and a micro-channel-plate detector. The complexes traveled for 20 cm after the skimmer and were intersected with one or more laser beams for resonance enhanced multiphoton ionization (REMPI). The UV and visible laser beams were generated from a dye laser (Continuum TDL-51) pumped by the 532 nm output of a Nd:YAG laser (Continnum NY61-20). The ionization schemes employed in the experiment are shown in Figure 2. In the $1_{UV} + 1'_{vis}$ mode, an UV photon was used to excite the one-photon allowed transitions to the Al(3*d*)·Ar and Al(4*p*)·Ar manifolds, followed by a visible photon for ionization. The UV photons were generated by frequency doubling of the visible output from the dye laser, and therefore $\nu_{UV} = 2 \cdot \nu_{visible}$. In the $2_{Vis} + 1'_{vis}$ mode, a focused visible beam was employed to excite the two-photon allowed transitions. Another photon of the same frequency was then used for ionization.

Following the multiphoton ionization, the ions were extracted perpendicular to the molecular beam and mass-analyzed by a Wiley-McLaren TOF mass spectrometer, and detected by a dual-microchannel plate detector. To acquire a REMPI spectrum, the integrated current of the mass peak of interest (e.g. mass 67 amu for $Al^+ \cdot Ar$) was measured by a gated integrator (Stanford Research System) as the laser frequency was tuned. Since the ionization efficiency would be significantly enhanced if the excitation matched an allowed transition. An electronic spectrum could be obtained by recording the ion intensity as a function of excitation frequency. To reduce the background from ionization of diffusion pump oil, the ablation laser was triggered at half the repetition rate, and background was subtracted out at every other shot of scan. The laser frequency was calibrated by the atomic Al $3d \leftarrow 3p$ and $4p \leftarrow 3p$ transitions, with the smallest grating step size available from the dye laser. The accuracy was within 0.11 cm^{-1}.

5.3 RESULTS AND DISCUSSION

In the Al·Ar complex, three doublet electronic states ($^2\Delta$, $^2\Pi$ and $^2\Sigma$) can be expected to originate from the Al $3d$ levels, and two doublet electronic states ($^2\Pi$ and $^2\Sigma$) from the $4p$ levels[1,6]. We first review the experimental and theoretical results for the transitions from the ground $^2\Pi$ ($3p$) state to the $^2\Sigma$ ($3d$) and $^2\Pi$ ($4p$) states above the Al($3d$)Ar dissociation limit measured at 3255.4 cm^{-1}[12]. Spotts[12] has reported the $4p$ $^2\Sigma$ state, and the $3d$ $^2\Delta$, $^2\Pi$ and $4p$ $^2\Pi$ states. In this section, we focus on evidence for the dissociative 3d $^2\Sigma$ state, and the comparison with theoretical analyses.

5.3.1 Review of Two-Photon Spectra of Al $^2\Pi(4p) \leftarrow {}^2\Pi(3p)$ Transition

Evidence for the two-photon $^2\Pi$ (4p) ← $^2\Pi$ (3p) transition has been reported by Spotts[12], and a summary the analysis is given here. The two-photon REMPI spectra for AlAr in 32550 to 33050 cm^{-1} region (the vicinity of atomic Al $4p \leftarrow 3p$ transitions) are shown in Figure 3. The spectra correspond to both $AlAr^+$ signal, and Al^+ signal arising from dissociative transitions in the Al·Ar complex. The observed band positions are reported in Table 1. Two vibronic progressions are clearly observed in both $AlAr^+$ and Al^+ channels. They are designated as series A and B. As shown in Table 2, the separations of adjacent bands between the two series (A2-B2, A3-B3, etc) are within 11-14 cm^{-1}. This range of separation is in good agreement with the atomic Al($4p$) $^2P_{1/2}$ - $^2P_{3/2}$ spin-orbit splitting (15.83 cm^{-1}), and thus the series A and B are assigned to the $^2\Pi_{1/2}$ ($4p$) and $^2\Pi_{3/2}$($4p$) electronic states respectively. The intense doublets in Al^+ spectrum are due to the atomic Al $^2\Pi_{1/2,3/2}$ ($4p$) ← $^2\Pi_{1/2,3/2}$ ($3p$) transitions.

The observation of dissociative signal in the Al^+ channel suggests a significant coupling of these bound vibronic bands to another dissociative electronic state in the same spectral region. Furthermore, there appears to be a selectively perturbation of the $^2\Pi_{1/2}$ ($4p$) state. Starting from the high frequency region, the $^2\Pi_{1/2}$ ($4p$) vibronic bands become increasing perturbed (increasing peak broadening) as the series moves towards the Al($3d$)Ar dissociation limit. However, the same pattern is not observed in the $^2\Pi_{3/2}$ ($4p$) bands. In the $AlAr^+$ spectrum, peak broadening becomes prominent at peaks A4 and A5. Their intensity in the Al^+ spectrum increases at the same time. Peak A6 is completely absent in the $AlAr^+$ channel, but exhibits as a broad feature (FWHM = ~20 cm^{-1}) in the Al^+ channel instead. This strongly dissociative feature suggests a curve crossing between the potentials of the $^2\Pi_{1/2}$ ($4p$) state and a dissociative state. We propose the coupling

state to be the repulsive $^2\Sigma^+_{1/2}$ ($3d$) state arising from the Al($3d$)Ar electronic manifold. Upon complexation with Ar, the degenerated $3d$ levels in Al atom will be splitted into Δ, Π and Σ states. The Σ state corresponds to the d_z orbital pointing towards the Ar atom. One may therefore expect a repulsive interaction with the closed-shell Ar in such an arrangement of electron density. One should also note that the peak X2 is not believed to be the perturbed A6 vibronic feature in Al^+·Ar channel, as it corresponds to a dip in the broadly dissociative Al^+ signal. Instead, it may be due to a quasi-level in the $^2\Sigma^+_{1/2}$ ($3d$) potential. Similar consideration may also apply to peak X3.

The proposed perturbation of $^2\Pi_{1/2}$ ($4p$) from $^2\Sigma^+_{1/2}$ ($3d$) is consistent with the allowed spin-electronic coupling in diatomic molecules. As discussed by Lefebvre-Brion and Field[14], the selection rules for the homogenous spin-electronic perturbations are:

$$\Delta\Lambda = +/- 1, \Delta\Sigma = -/+ 1, \Delta S = 0 \text{ and } \Delta\Omega = 0,$$

where Λ, Σ, S and Ω are the projections of standard angular momenta onto the inteatomic axis[14]. The $^2\Pi_{1/2}$ ($4p$) state can be described by the configuration $|\Lambda = +/- 1, \Sigma = -/+ 1/2, \Omega = 1/2\rangle$, and the $^2\Sigma^+_{1/2}$ ($3d$) state by configuration $|\Lambda = 0, \Sigma = +/- 1/2, \Omega = 1/2\rangle$. A perturbation by $^2S^+_{1/2}$ state, however, will not be allowed for the $^2\Pi_{3/2}$ state, which possesses $|\Lambda = +/1\ 1, \Sigma = +/- 1/2, \Omega = 3/2\rangle$ configuration.

5.3.2 One-Photon Spectra of Al $^2\Sigma^+$ (3d) ← $^2\Pi$ (3p) Transition at Al^+ Channel

Additional evidence for the presence of the dissociative state is observed from the one-photon Al^+ signal above the Al($3d$)Ar dissociation limit. Figure 4 shows the 1_{UV} + $1'_{vis}$ and 2_{vis} + $1'_{vis}$ REMPI spectral in this spectral region recorded at the Al^+ channel. The corresponding spectra measured at the $AlAl^+$ channel are also included for comparison.

The perturbed bands in the two-photon spectra are clearly exhibited in the Al^+ $1_{UV} + 1'_{vis}$ spectrum. While peaks A4 and A5 are distinctly observed, the X2 broad band appears as the most intense feature, with a prominent X3 peak located at the red tail of the band. A shoulder-like feature is also evident between X2 and X3 at about 32598 cm^{-1}. The X2 peak is near but not coincident with the two-photon A6 band. This overall profile from 32575 to 32635 cm^{-1} is characteristic of a bound $\rightarrow$ continuum transition, presumably between the ground and $^2\Sigma^+_{1/2}$ (3*d*) states. The appearance of the broad A6 and X2 bands in the Al^+ spectra suggests that the curve crossing between the $^2\Sigma^+_{1/2}$ (3*d*) and $^2\Pi_{1/2}$ (4*p*) states occurs within an internuclear distance accessible by direct Franck-Condon-allowed transition from the ground state. In other words, the curve-crossing point is located in the vicinity of the equilibrium ground-state bond distance (3.79 Å).[5]

5.3.3 Review of Ab Initio AlAr Potential Energy Curves

Our proposed assignments are consistent with the *ab initio* calculations performed by Jeff A. Sheehy and Jerry A. Boatz at Philips Laboratory, Edwards Air Force Base.[13] They employed the (17*s*12*p*5*d*4*f*)/[7*s*6*p*4*d*3*f*] atomic natural basis set (supplemented with diffuse (1*s*1*p*1*d*1*f*) functions), and calculated the potential energy curves at the level of multireference configuration interaction from [6331] (3 electrons in 13 orbitals) state-averaged complete active space reference wavefunctions. Spin-orbit interactions of the atomic Al moiety were neglected.

In the ground state calculations (Figure 5), the authors obtaine an equilibrium bond distance of 4.0 Å, which is longer than the experimental value of 3.79 Å[5]. The calculated bond energy (D_0) is 132 cm^{-1}, and is in good agreement with the 122.4 cm^{-1}

value measured by Morse and coworkers[6]. The potential energy curves of Al(3*d*)Ar and Al(4*p*)Ar manifolds are displayed in Figure 6. A strongly bound $^2\Pi(4p)$ state, with a binding energy of 498 cm^{-1}, is clearly shown in the calculations. An avoided crossing of the $^2\Pi(4p)$ and $^2\Pi(3d)$ states is evident at about 3.6 Å, with a nonadiabatic coupling strength of about 150 cm^{-1}. This perturbation is predicted to occur at a crossing point above the Al(3*d*)·Ar dissociation limit. However, our experiment suggests that the curve crossing occurs below the dissociation.[12] The discrepancy can be explained by the error in the *ab initio* value of the atomic Al(3*d*)/Al(4*p*) splitting. Comparing to an experimental value of 522 cm^{-1}, the calculations overestimate the asymptotic separation by about 300 cm^{-1}.

The calculations predict that the $^2\Sigma^+(3d)$ state is largely repulsive, but with a metastable well. At about 3.8 Å, the $^2\Sigma^+(3d)$ state is in a close proximity to the $^2\Pi(4p)$ and $^2\Pi(3d)$ states. It suggests a possible curve crossing with the $^2\Pi$ states in a region where Franck-Condon transitions will be favorable. This prediction is qualitatively consistent with spectra. Another noticeable feature is that an energy barrier appears at about 4.5 Å. The barrier height is approximately 116 cm^{-1} above the quasi-bound minimum of the state at 3.4 Å. The presence of a potential well in the 3-4 Å region may support the presence of quasi-bound vibrational levels Such levels would be consistent with the unassigned X2 peak observed as a dip in the fragmentation channel.

5.3.4 *Continuum← Bound Simulation for the $^2\Sigma^+_{1/2}(3d) \leftarrow X\ ^2\Pi_{1/2}(3p)$ Transition*

The experimental results and the *ab initio* calculations are consistent with a curve crossing between $^2\Sigma^+_{1/2}(3d)$ and $^2\Pi_{1/2}(4p)$ states. It will be informative to obtain direct

evidence for the $^2\Sigma^+_{1/2}(3d)$ state through the comparison of the dissociative A6 feature with the theoretical prediction. To this end, the *ab initio* potential energy curves were used to perform a bound $\rightarrow$ free Franck-Condon absorption intensity calculation. The absorption profile for the $^2\Sigma^+_{1/2}(3d) \leftarrow {}^2\Pi_{1/2}(3p)$ transition was simulated by using the computer program, BCONT, written and distributed by Le Roy[15], with *ab initio* data points as the input potentials. We should caution that for the ground $^2\Pi_{1/2}(3p)$ state, the *ab initio* calculations overestimate the Al-Ar bond length to 4.0Å (exp. = 3.79 Å)[5], and the D_0 value to 132 cm^{-1} (exp. = 132.4 cm^{-1})[6]. Nevertheless, no adjustment was applied to the *ab initio* potentials in our simulation. Furthermore, spin-orbit coupling in the Al atom was not included in the calculations.

The simulated profile for the $^2\Sigma^+_{1/2}(3d) \leftarrow {}^2\Pi_{1/2}(3p)$ transition is shown Figure 7. Input parameters for the BCONT program are given in Table 3. Three absorption features are predicted in the simulations. The dominant feature at 32438 cm^{-1} displays a symmetric profile with a FWHM of about 10 cm^{-1}. Another feature of lower intensity is located at 32414 cm^{-1}, 24 cm^{-1} to the lower-frequency side of the main peak. It has a FWHM of about 4 cm^{-1}. The third band at 32488 cm^{-1} is 50 cm^{-1} higher in frequency than the main absorption. It is significantly weaker than the other two features and has a FWHM of 28 cm^{-1}.

The two main absorptions (A' and B') are below the potential barrier on the $3d$ $^2\Sigma^+_{1/2}$ curve. They are likely to correspond to transitions from the ground state to the metastable-well of the $3d$ $^2\Sigma^+_{1/2}$ state, but not the outer-well region. As the equilibrium bond distance is 4 Å in the ground state and the barrier is located at 4.5 Å, the Franck-Condon overlap with the outer well region (internuclear distance $\rangle$ 4.5 Å) should be

unfavorable. Absorptions A' and B' support the possible transitions to quasi-bound levels in the upper state.

The frequency position of absorption C' suggests a correspondence to the potential barrier in the $3d\ ^2\Sigma^+_{1/2}$ state. As reviewed by Tellinghuisen[16], this type of absorption pattern corresponds to the fact that the continuum wave function in the upper state increases in amplitude owing to the presence of a barrier, and oscillates very slowly at small distances from the barrier maximum.. That, in turns, leads to an enhancement of the overlap integral. Such a transition behavior has been observed and simulated for different Σ states in Hg·RG systems (RG = Ne[17-19] and Ar[19,20]). The weak intensity in the simulation is probably due to the unfavorable Franck-Condon overlap with the ground-state wavefunction. If the barrier is located in Franck-Condon-allow region above the ground-state minimum, a more prominent transition can be expected. In order to verify the origin of the broad-band feature (C'), a simulation is performed with the $3d\ ^2\Sigma^+_{1/2}$ potential curve shifted to a shorter internuclear distance by 0.55 Å. The profile is shown in Figure 8. As the barrier is shifted to the Franck-Condon-allowed region, the intensity of the band C' increases significantly. This result agrees with the assignment of C' to the potential maximum on the $3d\ ^2\Sigma^+_{1/2}$ curve.

5.3.5 Comparison of Simulation and One-Photon Al^+ Spectrum

The simulated profile predicts three absorption bands for the $^2\Sigma^+_{1/2}(3d) \leftarrow X\ ^2\Pi_{1/2}(3p)$ transition: one peak due to the potential barrier, and two peaks due to the quasi-bound levels within the metastable well. One may compare the simulation with the one-photon Al^+ spectrum and obtain more insight about the observed features. However, one

should caution that the reliability in the simulated transition frequency and relative intensity is limited by the accuracy of the *ab initio* potentials. As discussed earlier, the *ab initio* calculations overestimate the asymptotic Al(3d)/Al(4p) separation by ~500 cm^{-1}, and the ground equilibrium distance by ~0.21 Å. And also, if quasi-bound levels are indeed present in the metastable well, a bound → bound simulation will be more appropriate to predict the transition frequency. The bound → continuum simulation should, therefore, only be used as a guideline for spectral assignment.

The intensity of peak B' suggests a correspondence to peak X2 in the one-photon Al^+ spectrum. The comparison is shown Figure 9. In order to match the absorption maximum with the experimental data, the simulation is shifted to higher frequency by 185 cm^{-1}. This blue shifting indicates that the calculated potentials underestimate the energy difference by ~200 cm^{-1}. The agreement is quite favorable, given the intrinsic accuracy possible for these electronic-excited-state calculations. The simulated profile agrees reasonably well with experimental data on the high-energy side, suggesting a fair reproduction of the potential curvature. Peak X3 in the Al^+ spectrum may be assigned to band A' in the simulated profile. However, the experimental frequency shift from the main absorption is 36 cm^{-1}, while the simulation only shows a 24 cm^{-1} displacement. For the band C', it may correspond to the unassigned intensity observed at 32670 to 32680 cm^{-1}. But one should note that the experiment displays two peak-like absorptions rather than a broad band of 50 cm^{-1} FWHM.

In this assignment scheme, all the experimental absorptions are due to the quasi-bound levels within the metastable well on the $3d\ ^2\Sigma^+_{1/2}$ potential. It will be consistent with the observed transitions in the $AlAr^+$ channel in both one-photon and two-photon

excitations. However, there is no correspondence for the shoulder feature observed at around 32609 cm^{-1}. If band A' is alternatively assigned to the 32609 cm^{-1} shoulder, one may have to assign peak X3 to a bound level originating from a different state such as the $4p\ ^2\Pi_{1/2}$. However, the peak's intensity in the AlAr+ channel is considerably lower than other bound levels in the $4p\ ^2\Pi$ spectrum.

Another possibility is that the actual barrier in the upper potential is located in a Franc-Condon-allowed region. The transition to the potential maximum will be more prominent. In the cases of favorable Franck-Condon overlap, the "barrier" band can even become the dominant feature in the absorption.[17-20] If one assumes such a behavior for the $^2\Sigma^+_{1/2}$ state, one may then assign Peak X2 to C', the shoulder at 32610 cm^{-1} to B', and Peak X3 to A'. In this scheme, the absorption intensity on the high-energy side of X2 (Figure 4a) can be attributed to the projection of ground-state wavefunction to the outer side of the barrier. It is also consistent to the dissociative A6 profile in the two-photon Al^+ spectrum.

5.3.6 Potential Barrier in the $^2\Sigma^+_{1/2}(3d)$ State

The presence of a potential maximum in the $^2\Sigma^+_{1/2}(3d)$ state is rather intriguing. As the barrier is located (4.5 Å) far away from the 3d-4p Π-states crossing point (3.8 Å), and the spin-orbit interaction is completely neglected in the *ab initio* calculations, it is unlikely that the barrier is resulted from avoided curve crossing in the calculation. Furthermore, in a simplified physical picture, this Σ state will correspond to the $3d_z$ orbital pointing towards the Ar atom, with the electron density located along the internuclear axis. One may therefore expect the Σ state to be totally repulsive due to Pauli

repulsion between the electron clouds. In order to explain such a potential maximum, Dual *et al.* have proposed a "penetration model" [1,20] for the presence of potential barrier in Σ states originating from Rydberg-like diffuse orbitals in metal-rare gas complexes. The postulated model can as summarized as follows: In a diffuse orbital, such as that in a Rydberg state, the long-range attractive dispersion is operative at a large internuclear distance. When the rare gas approaches the metal atom, it starts to experience repulsion from the outerlobe density of the Rydberg electron. At a shorter distance, the rare gas will then "penetrate" the diffuse electron cloud and experience stronger attractive forces from the unshielded metal core somewhat similar to the M^+·RG (M = metal atom) situation. In this way, a potential barrier at an intermediate internuclear distance will be resulted. This kind of potential maximum has also been observed in other metal atom-rare gas systems, such as Li[21-23], B[24,25], Ca[26], Al(4s Σ state)[4-6], In[27], Ga [28] and Hg[17-20,29].

5.4 SUMMARY

In this chapter we have reported the REMPI spectroscopy of the bound $4p\ ^2\Pi_{1/2}$ and $^2\Pi_{3/2}$ states, and the dissociative $3d\ ^2\Sigma^+_{1/2}$ state in the Al·Ar complex. The electronic transition from the ground state to $4p\ ^2\Pi_{1/2}$ and $^2\Pi_{3/2}$ states are monitored in both $AlAr^+$ and Al^+ channels. The dissociative spectrum at Al^+ channel suggests the coupling of the $^2\Pi_{1/2,3/2}$ states to the repulsive $3d\ ^2\Sigma^+_{1/2}$ state. Moreover, above the Al(3d)·Ar dissociation limit, the $4p\ ^2\Pi_{1/2}$ state is selectively perturbed significantly by $3d\ ^2\Sigma^+_{1/2}$ state through the allowed spin-electronic coupling.

The spin-electronic coupling is further manifested in the dissociative Al^+ spectrum of the $3d\ ^2\Sigma^+_{1/2}$ state obtained by one-photon excitation. Using the potential

energy curves obtained from *ab initio* calculations, a bound → continuum Franck-Condon-intensity simulation is performed, and compared with the one-photon $3d\ ^2\Sigma^+_{1/2}$ profile. The agreement provides convincing evidence for the nature of perturbation above the Al(3d)Ar dissociation limit, and the repulsive character of the $3d\ ^2\Sigma^+_{1/2}$ state. Furthermore, a potential maximum at 4.5 Å is predicted on the $3d\ ^2\Sigma^+_{1/2}$ potential by *ab initio* calculations. Such a potential maximum on a largely repulsive Σ state can be rationalized by the "penetration" model proposed for diffuse electronic orbitals in metal-rare gas complexes by Breckenridge and coworkers[1,20,26].

5.5 REFERENCES

1. W. H. Breckenridge, C. Jouvet, and B. Soep, in *Metal and Semiconductor Clusters: Spectroscopy and Structure*, Vol. 3, edited by M. A. Duncan (JAI Press Inc., Greenwich, Connecticut, 1995), pp. 1-83.

2. C. Crepin-Gilbert and A. Tramer, *Int. Rev. Phys. Chem.*, **18,** 485 (1999).

3. J. M. Gardner and M. I. Lester, *Chem. Phys. Lett.*, **137,** 301 (1987).

4. C. L. Callender, S. A. Mitchell, and P. A. Hackett, *J. Chem. Phys.*, **90,** 5252 (1989).

5. M. J. McQuaid, J. L. Gole, and M. C. Heaven, *J. Chem. Phys.*, **92,** 2733 (1990).

6. S. A. Heidecke, Z. Fu, J. R. Colt, and M. D. Morse, *J. Chem. Phys.*, **97,** 1692 (1992).

7. Z. Fu, S. Massick, J. G. Kaup, O. B. d'Azy, and W. H. Brenckenridge, *J. Chem. Phys.*, **97,** 1683 (1992).

8. K. F. Willey, C. S. Yeh, and M. A. Duncan, *Chem. Phys. Lett.*, **211,** 156 (1993).

9. X. Yang and P. L. Dagdigian, *J. Chem. Phys.*, **108,** 3522 (1998).

10. J. Lei and P. L. Dagdigian, *Chem. Phys. Lett.*, **304,** 317 (1999).

11. H. Partridge, C. W. Bauschlicher, Jr., and L. VIsscher, *Cehm. Phys. Lett.*, **246,** 33 (1995).

12. J. M. Spotts, *Ph.D. Thesis*, California Institute of Technology, 1998.

13. J. A. Boatz and J. A. Sheehy, (1998).

14. H. Lefebvre-Brion and R. W. Field, *Perturbations in the Spectra of Diatomic Molecules* (Academic Press, Orlando, Florida, 1986).

15. R. J. LeRoy, *Computer Phys. Commun.*, **52,** 383 (1989).

16. J. Tellinghuisen, *Adv. Chem. Phys.*, **60,** 299 (1985).

17. M. Okunishi, K. Yamanouchi, K. Onda, and S. Tsuchiya, *J. Chem. Phys.*, **98,** 2675 (1993).

18. K. Onda and K. Yamanouchi, *J. Chem. Phys.*, **102,** 1129 (1995).

19. L. Krim, C. Jouvet, B. Soep, K. Onda, K. Yamanouchi, and J. P. Visticot, *J. Cehm. Phys.*, **103,** 5956 (1995).

20. M.-C. Duval, O. B. D'Azy, W. H. Breckenridge, C. Jouvet, and B. Soep, *J. Chem. Phy.*, **85,** 6324 (1986).

21. W. Behmenburg, A. Makonnen, A. Kaiser, F. Rebentrost, V. Staemmler, M. Jungen, G. Peach, A. Devdariani, S. Tserkovnyi, A. Zagrebin, and E. Czuchaj, *J. Phys. B: At. Mol.Opt. Phys.*, **29** (1996).

22. A. Makonnen, A. Haiser, and W. Behmenburg, *Z. Phys. D,* **36,** 325 (1996).

23. S. J. Park, Y. S. Lee, and G.-H. Jeung, *Chem. Phys. Lett.*, **277,** 208 (1997).

24. E. Hwang, Y.-L. Huang, P. L. Dagdigian, and M. H. Alexander, *J. Chem. Phys.*, **98,** 8484 (1993).

25. E. Hwang, P. L. Dagdigian, and M. H. Alexander, *Can. J. Chem.*, **72,** 821 (1994).

26. A. W. Leung, J. G. Kaup, D. Bellert, J. G. McCaffrey, and W. H. Brenckenridge, *J. Chem. Phys.*, **111,** 2484 (1999).

27. W. M. Fawzy, R. J. LeRoy, B. Simard, H. Niki, and P. A. Hackett, *J. Chem. Phys.*, **98,** 140 (1993).

28. S. J. Park, M. C. Kim, Y. S. Lee, and G.-H. Jeung, *J. Chem. Phys.*, **107,** 2481 (1997).

29. K. Onda, K. Yamanouchi, M. Okunishi, and S. Tsuchiya, *J. Chem. Phys.*, **101,** 7290 (1994).

Table 1 Observed vibronic bands for $^2\Pi_{1/2}$ (4p) ← $^2\Pi_{1/2}$ (3p) and $\Pi_{1/2}$ (4p) ← $^2\Pi_{1/2}$ (3p) transitions in Al^+·Ar and Al^+ channels by two-photon excitation.

Al(4*p*) $^2\Pi_{1/2}$ (Series A)	Al(4*p*) $^2\Pi_{3/2}$ (Series B)	Unassigned Features	Al^+·Ar Channel (cm^{-1})	Al^+ Channel (cm^{-1})
A1			32890	-----
	B2		32862	-----
A2			32848	32848
	B3		32816.5	32817.2
A3			32803.7	32803.3
		X1	32775.5	32777.0
	B4		32765.7	32765.0
A4			32753.5	32752.7
	B5		32708.0	32706.4
A5			32697.0	32695.4
	B6		32652.2	32651.0
		X2	32618.4	-----
A6 [a]			-----	32626 (band max)
		X3 [a]	32587.0	32586.5
	B7		32572.9	35272.0

[a] Broad A6 feature corresponds to the $^2\Sigma^+_{1/2}$ (3*d*) state.

Table 2 Observed differences between Series A and B. The values correspond to the spin-orbit splittings between $\Pi_{1/2}$ (4*p*) and $^2\Pi_{3/2}$ (4*p*) vibronic bands.

Vibronic Levels	Spin-Orbit Splitting from Al^+·Ar channel (cm^{-1})
A2-B2	14.0
A3-B3	12.8
A4-B4	12.2
A5-B5	11.0
Al(4p) $^2P_{3/2}$ - $^2P_{1/2}$	15.83

Table 3 Input parameters for BCONT 1.4 Franck-Condon-intensity calculations for Al·Ar $^2\Sigma^+_{1/2}$ ($3d$) ← $^2\Pi_{1/2}$ ($3p$) transition.

NFIT	IORD	IFREE	NV	NJ	IRDAT	NEWPOT	IWR	IPNCH	OVRCRT
0	2	1	1	0	1	1	-1	1	1.0D-5

NT	NFR	IRWAVL	IFRPW
0	120	0	1

WAVL

32320	32322	32324	32326	32328	32330	32332	32334
32336	32338	32340	32342	32344	32346	32348	32350
32352	32354	32356	32358	32360	32362	32364	32366
32368	32370	32372	32374	32376	32378	32380	32382
32384	32386	32388	32390	32392	32394	32396	32398
32400	32402	32404	32406	32408	32410	32412	32414
32416	32418	32420	32422	32424	32426	32428	32430
32432	32434	32436	32438	32440	32442	32444	32446
32448	32450	32452	32454	32456	32458	32460	32462
32464	32466	32468	32470	32472	32474	32476	32478
32480	32482	32484	32486	32488	32490	32492	32494
32496	32498	32500	32502	32504	32506	32508	32510
32512	32514	32516	32518	32520	32522	32524	32526
32528	32530	32532	32534	32536	32538	32540	32542
32544	32546	32548	32550	32552	32554	32556	32558

EV
15.136

BV
0.0707443

IVFIX	JFIX
0	0

ZMU	RMIN	RH	REX
16.104377	1.6	0.001	3.96

NTPI	VLIMI
26	141.0492889

NUSEI	VSHFTI	RFACTI	VFACTI
12	0	1.D0	1.D0

Table 3 Continued.

RTPI	VTPI	RTPI	VTPI	RTPI	VTPI
2.0	17230.341	2.4	5590.111	2.6	3185.497
2.8	1754.527	3.0	914.718	3.2	439.705
3.4	186.336	3.5	112.442	3.6	62.596
3.7	30.648	3.8	11.870	3.9	2.568
4.0	0.000	4.1	2.096	4.2	7.195
4.5	30.501	4.8	54.857	5.0	68.705
5.2	80.312	5.4	89.803	6.0	108.566
7.0	122.098	8.0	127.159	10.0	130.452
12.0	131.317	100.0	131.718		

PRM(1)	PRM(2)	PRM(3)
1	0	0

NTPF	VLIMFI
26	32235.79869

NUSEF	VSHFTF	RFACTF	VFACTF
12	0	1.D0	1.D0

RTPF	VTPF	RTPF	VTPF	RTPF	VTPF
2.0	43861.792	2.4	35002.395	2.6	33528.941
2.8	32792.327	3.0	32460.406	3.2	32343.827
3.4	32329.384	3.5	32339.143	3.6	32353.579
3.7	32369.875	3.8	32386.172	3.9	32401.456
4.0	32414.839	4.1	32425.746	4.2	32434.163
4.5	32445.107	4.8	32438.665	5.0	32428.219
5.2	32414.246	5.4	32398.067	6.0	32345.091
7.0	32273.917	8.0	32238.703	10.0	32224.018
12.0	32225.067	100.0	32226.749		

PRM(4)	PRM(5)	PRM(6)
3.59	0.2056	0

5.6 FIGURE CAPTIONS

Figure 1 Schematic diagram for the REMPI apparatus.

Figure 2 $1_{UV} + 1'_{vis}$ and $2_{vis} + 1'_{vis}$ excitation schemes for the REMPI experiments.[12]

Figure 3 $2_{vis} + 1'_{vis}$ single-color REMPI spectra obtained above the Al(3*d*)Ar dissociation limit at 32557.8 cm^{-1}. Top panel shows the spectrum recorded at the $AlAr^+$ channel. Bottom panel shows the spectrum from Al^+ channel.[12]

Figure 4 Comparison of REMPI spectra above the Al(3*d*)Ar dissociation limit: Al^+ channel at (a) $1_{UV} + 1'_{vis}$ and (b) $2_{vis} + 1'_{vis}$ excitation; $AlAr^+$ channel at (c) $1_{UV} + 1'_{vis}$ and (d) $2_{vis} + 1'_{vis}$ excitation.[12]

Figure 5 Ground state $^2\Pi(3p)$ and $^2\Sigma^+(3p)$ potential energy curves for AlAr.[13]

Figure 6 Potential energy curves arising from Al(3*d*)Ar and Al(4*p*)Ar electronic manifolds.[13]

Figure 7 BCONT 1.4 continuum ← bound simulation of the $^2\Sigma^+(3d) \leftarrow {}^2\Pi(3p)$ transition based on the potential energy curves by Sheehy.[13]

Figure 8 BCONT 1.4 continuum ← bound simulation of the $^2\Sigma^+(3d) \leftarrow {}^2\Pi(3p)$ transition based on the potential energy curves by Sheehy.[13] The upper $^2\Sigma^+(4p)$ is shifted to shorter internuclear distance by 0.55 Å.

Figure 9 Comparison of the BCONT 1.4 simulated dissociative $^2\Sigma^+(3d)$ profile with the experimental $1_{UV} + 1'_{vis}$ spectrum at Al^+ channel.

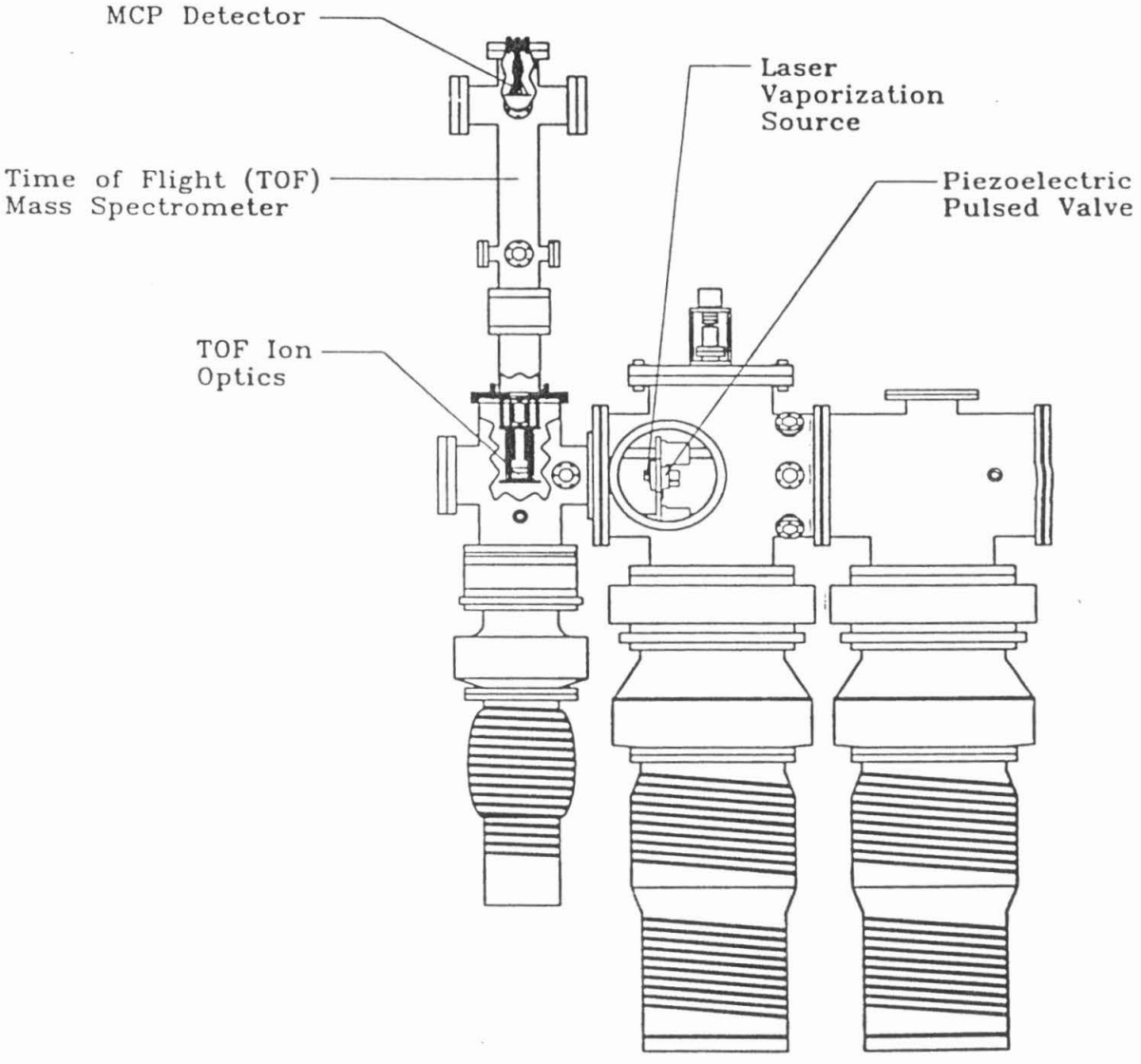
MCP Detector
Laser
Vaporization
Source
Time of Flight (TOF)
Mass Spectrometer
Piezoelectric
Pulsed Valve
TOF Ion
Optics

Figure 1

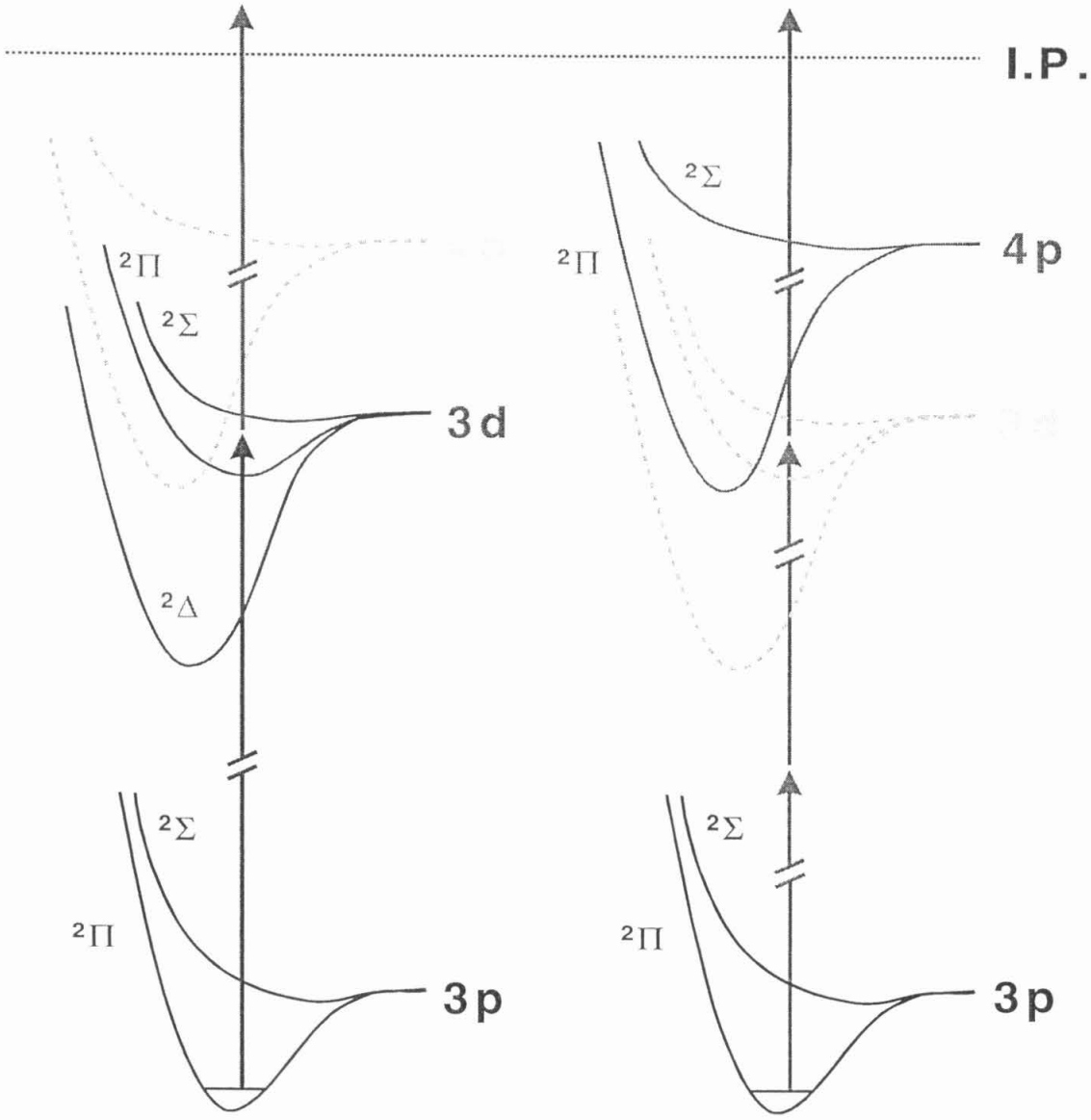
I.P.
$^2\Sigma$
4p
$^2\Pi$
$^2\Pi$
$^2\Sigma$
3d
$^2\Delta$
$^2\Sigma$
$^2\Pi$
3p
$^2\Sigma$
$^2\Pi$
3p

Figure 2

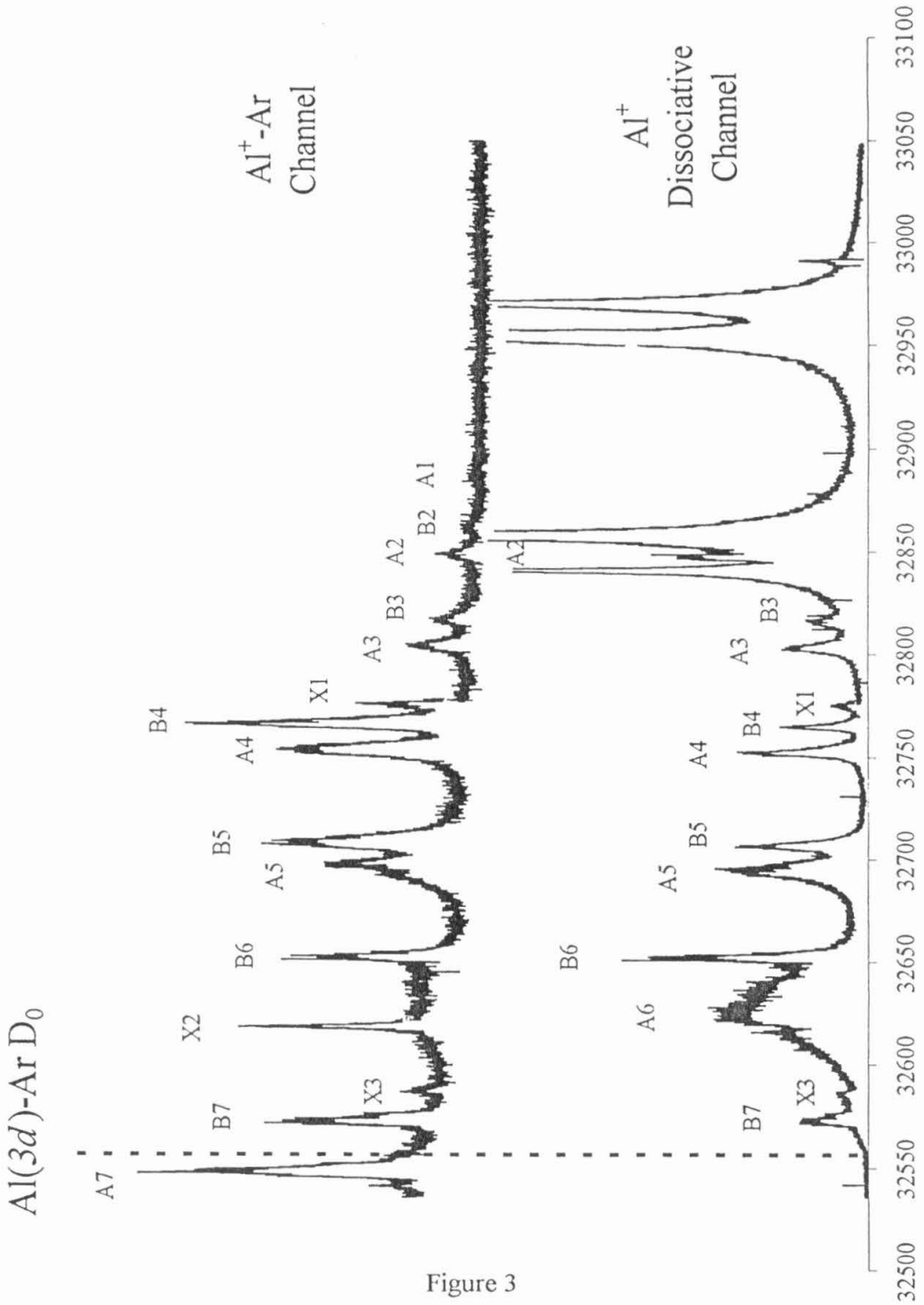
Al(3d)-Ar D0
Al+-Ar Channel
Al+ Dissociative Channel
A7
B7
X3
X2
B6
A6
B5
A5
B4
A4
X1
A3
B3
A2
B2
A1
32500
32550
32600
32650
32700
32750
32800
32850
32900
32950
33000
33050
33100

Figure 3

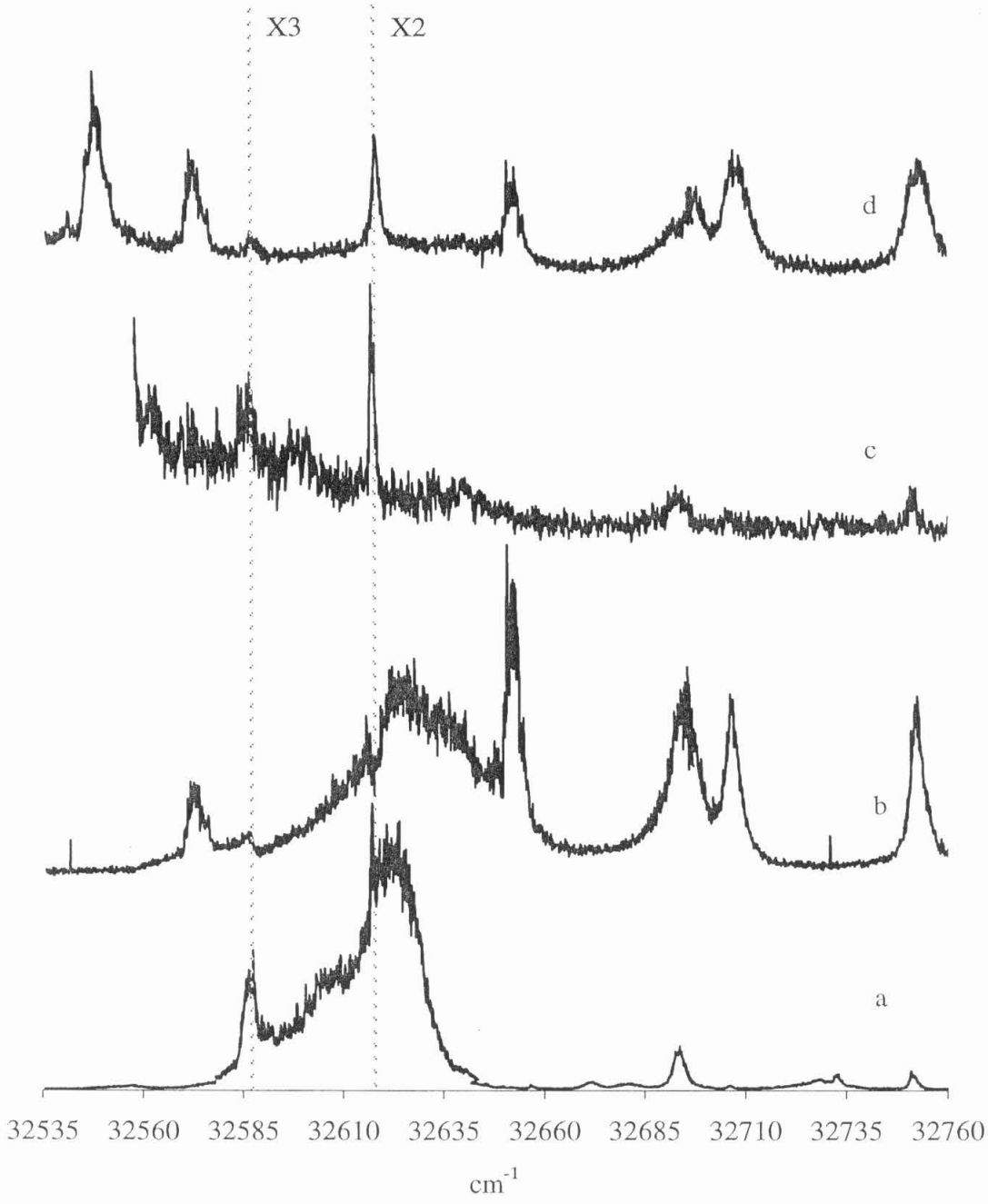
X3
X2
d
c
b
a
32535
32560
32585
32610
32635
32660
32685
32710
32735
32760
cm-1

Figure 4

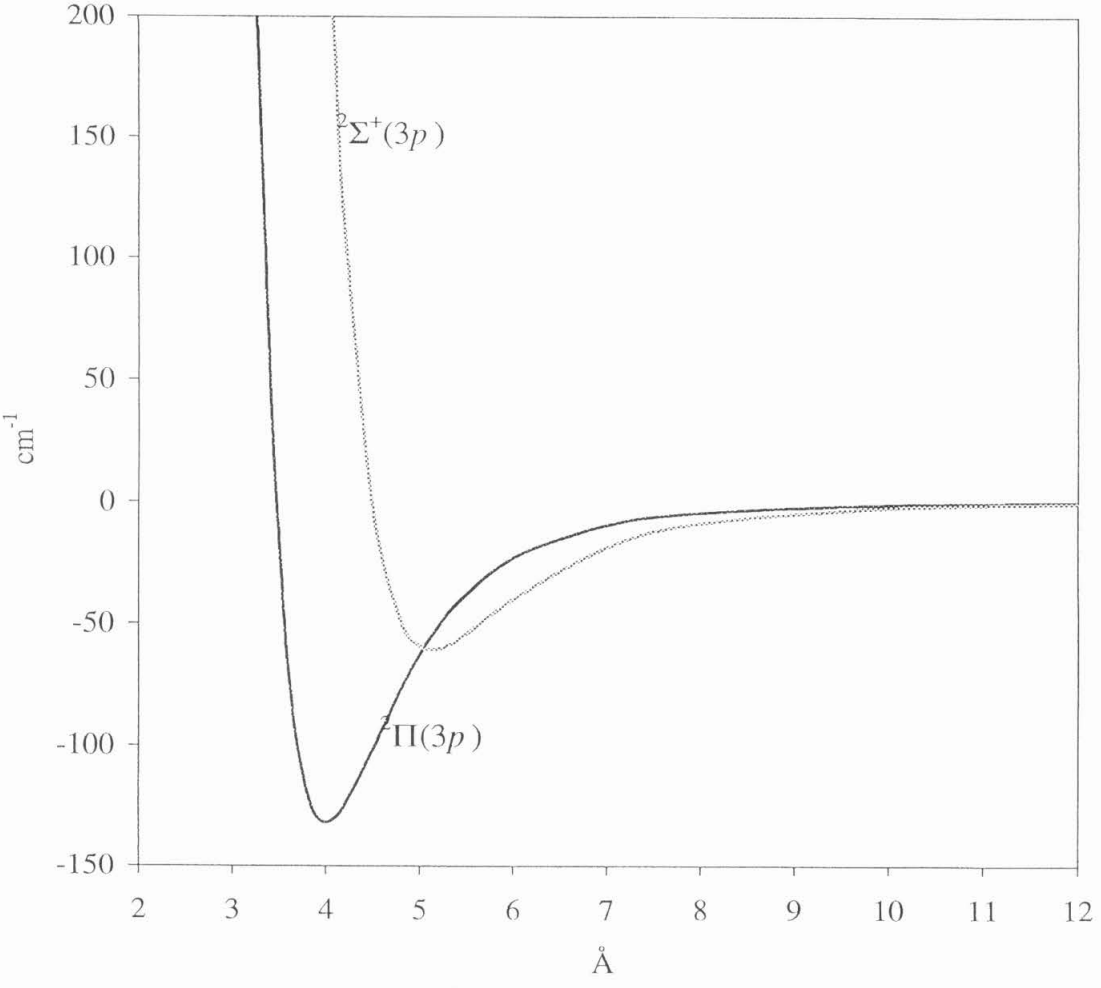

Figure 5

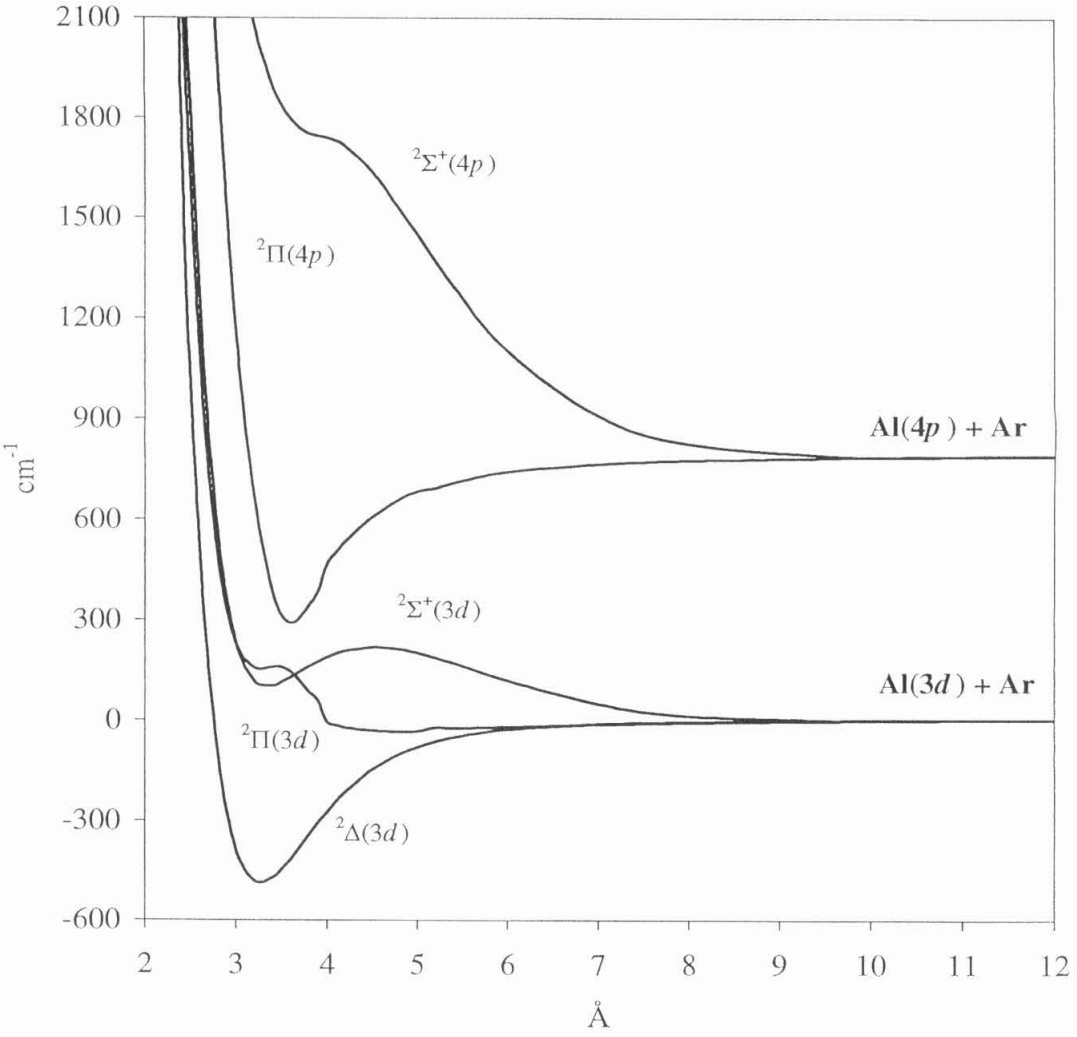
2100
1800
1500
1200
900
600
300
0
-300
-600
cm-1
2
3
4
5
6
7
8
9
10
11
12
Å
2Σ+(4p)
2Π(4p)
Al(4p) + Ar
2Σ+(3d)
Al(3d) + Ar
2Π(3d)
2Δ(3d)

Figure 6

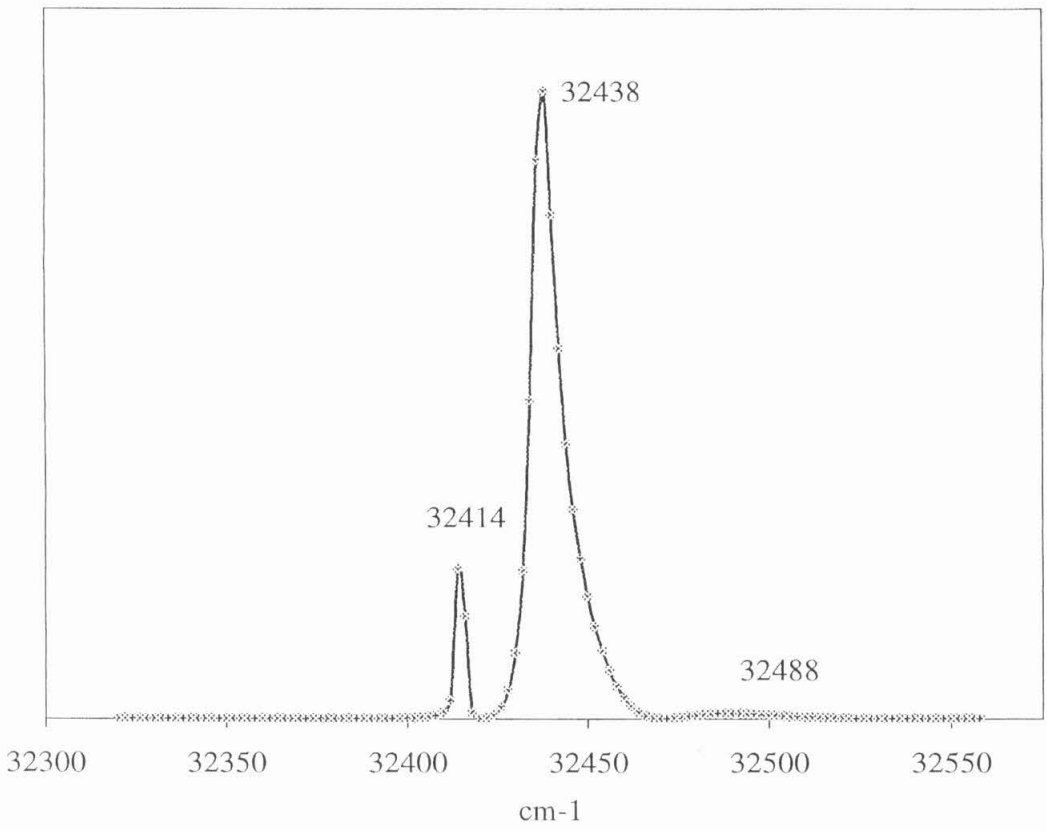

Figure 7

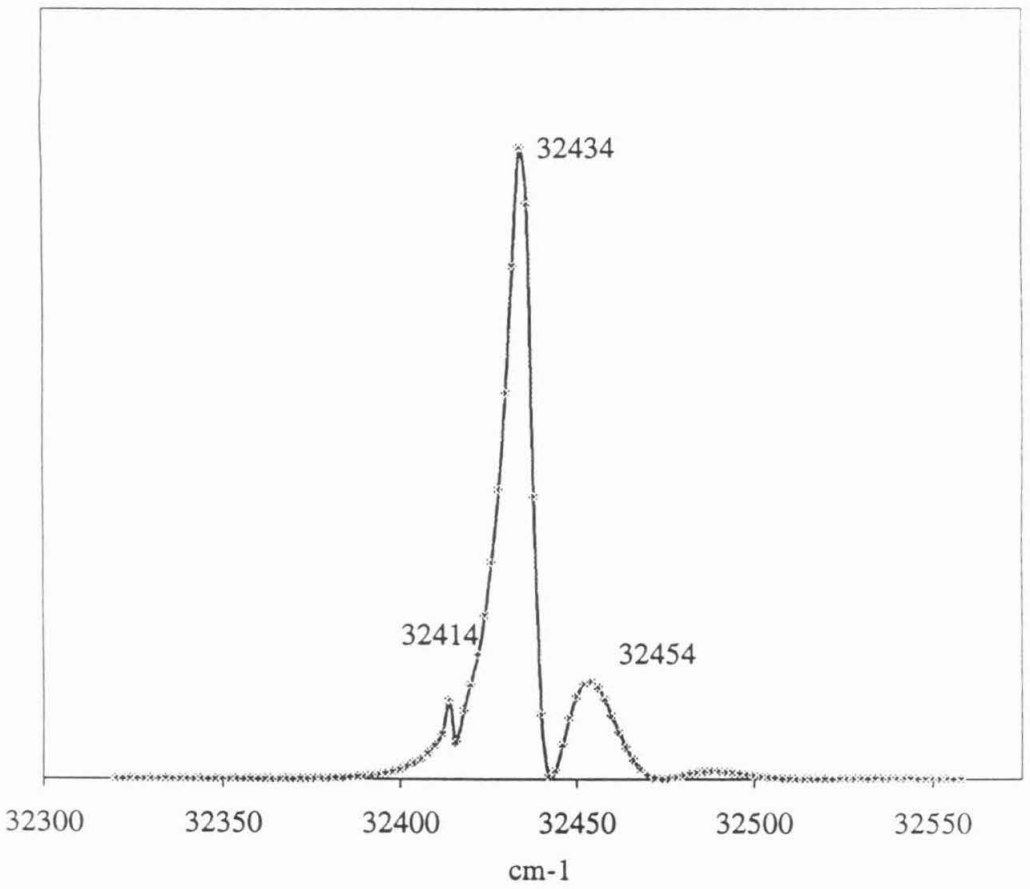

Figure 8

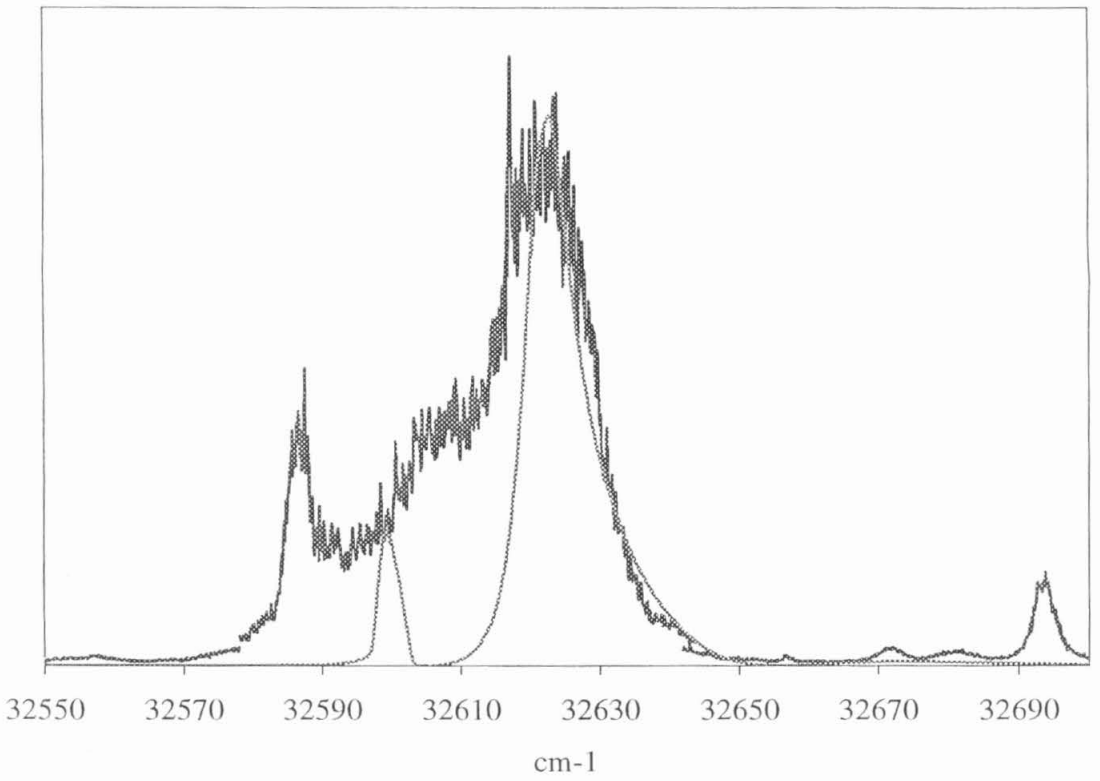

Figure 9